CRCLEME

Cooperative Research Centre for
Landscape Environments
and Mineral Exploration

ANU
THE AUSTRALIAN NATIONAL UNIVERSITY

SPECIAL VOLUME

REGOLITH GEOCHRONOLOGY AND LANDSCAPE EVOLUTION

Brad Pillans
Editor

SPECIAL VOLUME

CRC LEME OPEN FILE REPORT 189

September 2006

REGOLITH GEOCHRONOLOGY AND LANDSCAPE EVOLUTION

Brad Pillans
Editor

CRC LEME OPEN FILE REPORT 189

SPECIAL VOLUME

CRC LEME is an unincorporated joint venture between CSIRO-Exploration & Mining, and Land & Water, The Australian National University, Curtin University of Technology, University of Adelaide, Geoscience Australia, Primary Industries and Resources SA, NSW Department of Primary Industries and Minerals Council of Australia.

Headquarters: CRC LEME c/o CSIRO Exploration and Mining, PO Box 1130, Bentley WA 6102, Australia

Electronic copies of the publication in PDF format can be downloaded from the CRC LEME web site http://crcleme.org.au/Pubs/OFRindex.html. Information on this or other LEME publications can be obtained from http://crcleme.org.au. Hard copies will be retained in the Australian National Library, the Western Australian State Library, and libraries at The Australian National University-Canberra, CSIRO-Kensington-Perth, The University of Adelaide and Geoscience Australia-Canberra.

Reference:
Pillans B, 2006. Regolith Geochronology and Landscape Evolution. *CRC LEME Special Volume Open File Report 189,* 95pp

Keywords:
1. Geochronology - Australia. 2. Regolith - Australia. 3. Landscape Evolution - Australia

ISSN 1329-4768
ISBN 1 921039 51 5

Address and affiliations of Editor

Professor Brad Pillans
CRC LEME
Research School of Earth Sciences
The Australian National University
Canberra, ACT, 0200.

Published by: CRC LEME
c/o CSIRO Exploration and Mining
PO Box 1130, Bentley, Western Australia 6102.

TABLE OF CONTENTS

INTRODUCTION: THE LEME GEOCHRONOLOGY PROJECT

Brad Pillans

CRC LEME, Research School of Earth Sciences, ANU, Canberra, ACT, 0200

The current LEME Geochronology Project [full title: Geochronology and models of landscape evolution], grew out of the Paleomagnetic Dating Project that began in LEME 1 in 1995. Eleven years on, paleomagnetic dating remains at the forefront of the project, but is now supplemented by other dating methods including K/Ar and Ar/Ar, cosmogenic isotopes, luminescence, (U-Th)/He, U/Pb and U-series (Fig. 1). Of these, the latter three methods have yet to reach maturity and further work is required to fully test their applications to regolith materials; the other methods may be considered to be "well established".

The papers in this volume arose from a Regolith Dating Methods Workshop, held in the Research School of Earth Sciences at the Australian National University on Wednesday 20th November 2002. Work being carried out within CRC LEME Geochronology Project was discussed at this workshop and is described in this volume.

Below I outline some of the highlights of the Geochronology Project and its forerunner, the Paleomagnetic Dating Project. Overviews of Australian regolith geochronology are given in Pillans (1998, 2005). An offshoot from the Geochronology Project, the History of Aridity Project is also briefly discussed.

LACHLAN FOLD BELT/WESTERN NEW SOUTH WALES

First results were obtained from Northparkes mine, where Eric Tonui was undertaking his PhD fieldwork (Tonui 1998). Oxidized saprolite yielded a surprisingly old paleomagnetic age of ~320 Ma (Pillans *et al*. 1999), which when combined with apatite fission track data, indicated episodes of kilometre-scale burial and denudation (O'Sullivan *et al*. 2000). Interestingly, recently published K/Ar ages from the Jenolan Caves (Osborne *et al*. 2006) support this regional story.

Further paleomagnetic dating has been undertaken by Martin Smith (2001; 2006) at McKinnons, Elura, New Cobar and Peak Hill mines, yielding generally younger (Cenozoic and Mesozoic) ages. As part of his PhD study, in western NSW, Martin Smith also undertook a study of the suitability of U/Pb dating of anatase in silcrete (See Smith *et al*. this volume).

YILGARN

An early focus in the Geochronology Project was paleomagnetic dating of regolith in the Yilgarn. Sampling was undertaken in open pit mines, which provided excellent, deep exposures. Initially it was hoped to be able to date the widespread, so called "lateritic residuum"; however, this generally proved unsuitable for paleomagnetic dating. On the other hand, oxidized saprolite, up to 100 m below the surface, turned out to be an ideal medium, and revealed a long history of weathering dating back, in some instances, to pre-Cenozoic times. Some early results were published in Anand & Paine (2002, Table 16). These and later results clearly showed that deep oxidation had preferentially occurred during two major episodes – around 60 Ma, and during the last 12 Ma. There is also evidence of an earlier deep oxidation episode at ~300-315 Ma at Laverton (Lancefield mine) and Meekatharra (St Barbara's mine), and another at ~180 Ma at Kalgoorlie (Mt Percy). The result from Lancefield is particularly interesting because the oxidation occurs in a tillite which is overlain by shale of early Permian age (Eyles & de Broekert 2001). The paleomagnetic weathering age indicates that the tillite must be latest Carboniferous or older.

Recent studies (e.g. Pigeon *et al*. 2004; Heim *et al*. 2006) have demonstrated the potential for dating iron nodules in Western Australia using the (U-Th)/He method. Mark Paine (formerly Curtin University) and Martin Smith (ANU) have pioneered this technique in LEME.

Suzanne Simons and Alexander Nemchin have investigated U-series dating of opal veins at Yalgoo (Simons & Nemchin, this volume).

LUCAS HEIGHTS

In July 2002 I was asked to assist in determining the timing of last movement of two faults on the site of the replacement research reactor (RRR) at Lucas Heights in Sydney.

The steeply dipping faults could be traced for more than 100m across the RRR excavation. The eastern strand was a normal fault with a dip separation of 1-1.3 m, while the western strand was a reverse fault with a dip separation of 0.25-0.3 m. The key issue was to assess the seismic hazard posed by the faults.

With no record of historical record of seismicity or surface fault rupture, the only obvious constraint on the history of fault movement was that they offset Triassic age Hawksbury Sandstone. In other words at least one faulting event had occurred in the last 200 million years –hardly a close constraint. However, in the south wall of the excavation a layer of iron oxide was draped across, but not cut by the faults. Samples of the iron oxide layer were taken for paleomagnetic measurements, and showed that the layer had reverse polarity which must have been acquired prior to the last reversal of the Earth's magnetic field (the Matuyama/Bruhnes reversal dated at ~0.78 Ma (Pillans & Bourman 1996)). Thus the last fault movement occurred at least 0.78 million years ago. Indeed, the paleomagnetic pole position indicated an age of > 5 Ma (Pillans 2003), which was considered sufficiently long ago for the risk of future fault movement to be negligible, and for approval to be given to proceed with construction. The RRR will be commissioned in early 2007.

SOUTH AUSTRALIA

Following on from paleomagnetic studies of Pleistocene sections near Adelaide (Pillans & Bourman 1996, 2001), further paleomagnetic sampling was undertaken of deeply oxidized rocks in the Mount Lofty Ranges and at the Moonta copper mine on Yorke Peninsula. Ages from both areas were late Cenozoic (Figure 2), as are K/Ar ages on alunite clays from Moonta (J. Dunlap pers. comm. 2005).

Further north, a ferricrete-capped mesa near Marla has become something of a reference locality for the Geochronology Project – see Figure 2. Paleomagnetic samples from the ferricrete yield a well-defined pole with an age of ~60 Ma, indistinguishable from the regionally extensive Morney Profile in SW Queensland (Idnurm & Senior 1978). Preliminary (U-Th)/He ages (Smith 2006) on the ferricrete are slightly younger (~50 Ma), but are uncorrected for He diffusion losses.

At Beltana, in the Flinders Ranges, there has been much speculation about the origin of the willemite (Zn_2SiO_4) ore – is it supergene or hypogene? In 2001 I collected samples of coronadite associated with the willemite (Figure 3), which yielded a K/Ar age of 435±5 Ma (Groves *et al*. 2003). The age of the coronadite, together with fluid inclusion studies that indicate temperatures of formation in the range 50-150°C, clearly support a hypogene origin (Groves *et al*. 2003). The Beltana results, along with new results from Trinity Well, are further discussed by Jim Dunlap in this volume.

NORTHERN TERRITORY

Prior to LEME, little was known about the age of regolith in the Northern Territory, with one notable exception - a K/Ar dating study of supergene manganese deposits on Groote Eylandt by Dammer *et al*. (1996). However, in 2003, Juan-Pablo Bernal completed a PhD study on the Ranger uranium mine (Bernal 2003), demonstrating that U-series dating was feasible on goethitic pisoliths less than 0.5 million years old (see Bernal *et al*. this volume).

Recently, two LEME projects (NT Regolith, and Tanami projects) provided the opportunity to carry out reconnaissance paleomagnetic dating on samples from a wide range of sites (Pillans & Craig 2005). Current detailed work in the Tanami region indicates that the deep oxidation extends back to ~320 Ma, and that the area has been continuously subaerially exposed for at least 100 Ma, and perhaps longer.

HISTORY OF ARIDITY PROJECT

This project, which ran from 2002 until 2006, was designed to investigate the chronology and evolution of aridity in Australia from about 30 million years ago to the present. Luminescence dating and cosmogenic nuclides indicate that dune systems and stony deserts (gibbers) are significantly older

than previously thought. Papers by Derek Fabel and John Chappell, in this volume, describe the theory and application of cosmogenic nuclide dating in the context of landscape evolution.

REFERENCES

ANAND, R. & PAINE, M. 2002. Regolith geology of the Yilgarn Craton, Western Australia: implications for exploration. *Australian Journal of Earth Sciences* **49**, 3-162.

BERNAL, J.P. 2003. *In situ measurement of U-series diequilibria in iron oxy/hydroxidesand its application to weathering geochronology*. Unpublished PhD thesis, ANU, Canberra.

DAMMER, D., MCDOUGALL, I. & CHIVAS, A.R., 1996. Isotopic dating of supergene manganese oxides from the Groote Eylandt deposit. *Economic Geology* **91**, 386-401.

EYLES, N. & DE BROEKERT, P. 2001. Glacial tunnel valleys in the Eastern Goldfields of Western Australia cut below the Late Paleozoic Pilbara ice sheet. *Palaeogeography, Palaeoclimatology, Palaeoecology* **171**, 29-40.

GROVES, I.M., CARMAN, C.E. & DUNLAP, W.J., 2003. Geology of the Beltana willemite deposit, Flinders Ranges, South Australia. *Economic Geology* **98**, 797-818.

HEIM, J.A., VASCONCELOS, P.M., SHUSTER, D.L., FARLEY, K.A. & BROADBENT, G. 2006. Dating paleochannel iron ore by (U-Th)/He analysis of supergene goethite, Hamersley province, Australia. *Geology* **34**, 173-176.

IDNURM, M. & SENIOR, B.R. 1978. Palaeomagnetic ages of Late Cretaceous and Tertiary weathered profiles in the Eromanga Basin, Queensland. *Palaeogeography, Palaeoclimatology, Palaeoecology* **24**, 263-277.

OSBORNE, R.A.L., ZWINGMANN, H., POGSON, R.E. & COLCHESTER, D.M., 2006. Carboniferous clay deposits from Jenolan Caves, New South Wales: implications for timing of speleogenesis and regional geology. *Australian Journal of Earth Sciences* **53**, 377-405.

O'SULLIVAN, P.B., GIBSON, D.L., KOHN, B.P., PILLANS, B. & PAIN, C.F. 2000. Long-term landscape evolution of the Northparkes region of the Lachlan Fold Belt, Australia: Constraints from fission track and paleomagnetic data. *Journal of Geology* **108**, 1-16.

PIDGEON, R.T., BRANDER, T. & LIPPOLT, H.J, 2004. Late Miocene (U+Th)-^{4}He ages of ferruginous nodules from lateritic duricrust, Darling Range, Western Australia. *Australian Journal of Earth Sciences* **51** 901-909.

PILLANS, B. 1998. *Regolith Dating Methods. A Guide to Numerical Dating Techniques*. Cooperative Research Centre for Landscape Evolution and Mineral Exploration, Perth, 30 pp.

PILLANS, B. 2002. Climate-driven weathering episodes during the last 200 Ma in Southern Australia. *In*: Preiss, V.P. ed. *Geoscience 2002: Expanding Horizons. Abstracts of the16th Australian Geological Convention. Geological Society of Australia, Adelaide Convention Centre, Adelaide, SA, Australia. July 1-5 2002*, pp. 428.

PILLANS, B. 2003. Dating ferruginous regolith to determine fault capability at Lucas Heights, Sydney. *In*: Roach, I.C. ed. *Advances in Regolith: Proceedings of the CRC LEME Regional Regolith Symposia, 2003*, 324-327.

PILLANS, B. 2005. Geochronology of the Australian regolith. *In*: Anand, R.R. & de Broekert, P eds. *Regolith-Landscape Evolution Across Australia.* CRC LEME Monograph, pp. 41-61.

PILLANS, B. & BOURMAN, R., 1996. The Brunhes/Matuyama polarity transition (0.78 Ma) as a chronostratigraphic marker in Australian regolith studies. *AGSO Journal of Australian Geology and Geophysics* **16(3)**, 289-294.

PILLANS, B. & BOURMAN, R., 2001. Mid Pleistocene arid shift in southern Australia, dated by magnetostratigraphy. *Australian Journal of Soil Research* **39**, 89-98.

PILLANS, B. & CRAIG, M. 2005. Reconnaissance paleomagnetic dating of regolith samples from the Northern Territory. *In*: Roach, I.C. ed. *Regolith 2005. Ten Years of CRC LEME*. CRC LEME, pp. 248-251.

PILLANS, B., TONUI, E. & IDNURM, M. 1999. Paleomagnetic dating of weathered regolith at Northparkes mine, NSW. *In*: Taylor, G. & Pain, C. eds. *New Approaches to an Old Continent*. Cooperative Research Centre for Landscape Evolution and Mineral Exploration, Perth, pp. 237-242.

SCHMIDT, P.W. & EMBLETON, B.J.J. 1976. Palaeomagnetic results from sediments of the Perth Basin, Western Australia, and their bearing on the timing of regional lateritisation. *Palaeogeography, Palaeoclimatology, Palaeoecology* **19**, 257-273.

SMITH, M. 2001. *Palaeomagnetic age and geochemical characteristics of the regolith in the Cobar Basin, NSW*. Unpublished BSc (Hons) thesis, University of New South Wales, Sydney.

SMITH, M. 2006. *Towards a geochronology of long term landscape evolution in northwestern NSW*. Unpublished PhD thesis, ANU, Canberra.

TONUI, E. 1998. *Regolith mineralogy and geochemistry at Goonumbla, Parks, NSW*. Unpublished PhD thesis, ANU, Canberra.

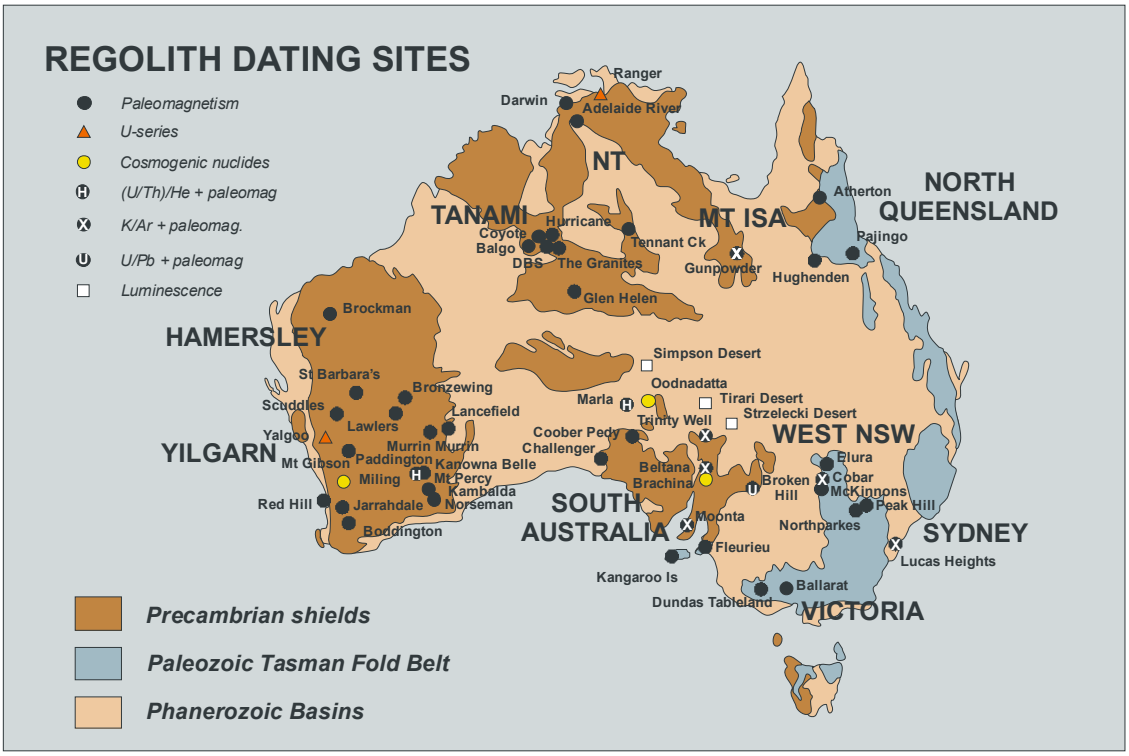

Figure 1. Map showing the distribution of sites from which samples have been dated in the Geochronology Project.

Figure 2. A. View, looking northwest, of a ferricrete-capped mesa, near Marla, in northern South Australia, from which a paleomagnetic weathering age of ~60 Ma has been obtained.

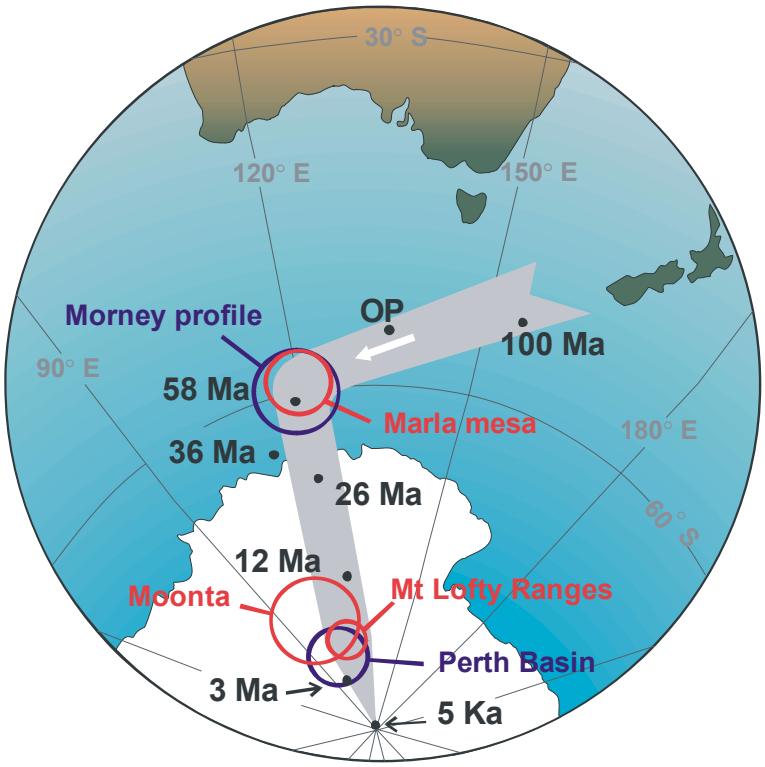

B. Paleomagnetic poles (95% confidence circles) for sites in South Australia, compared with two well established poles from SW Queensland (Morney Profile) and Perth Basin (WA) – data from Idnurm & Senior (1978) and Schmidt & Embleton (1976), respectively.

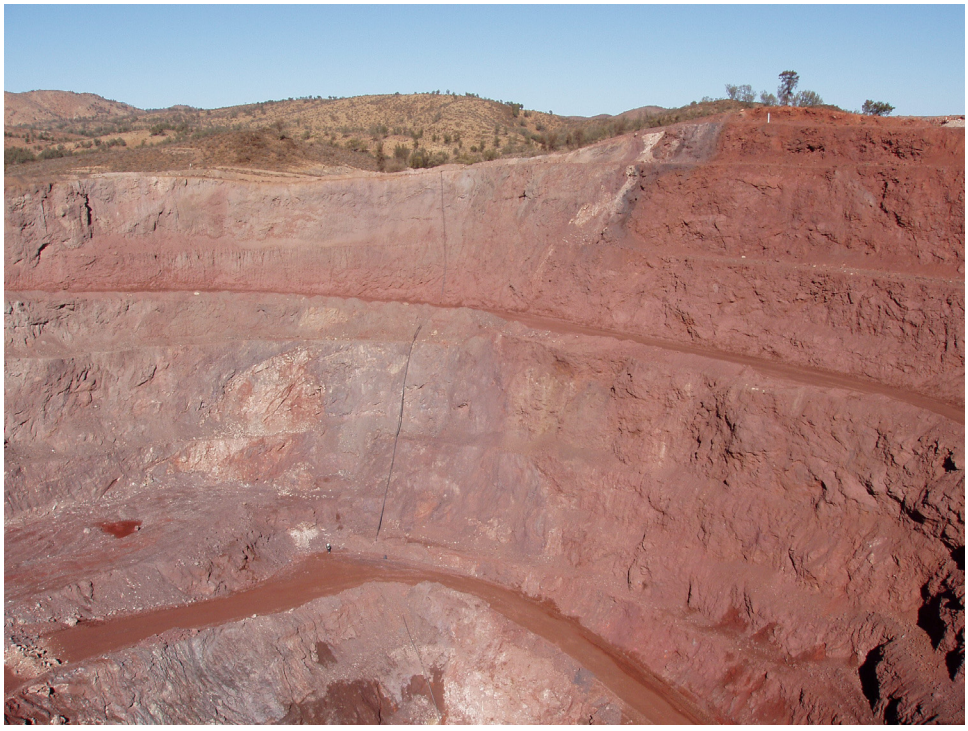

Figure 3. View, looking south, of the Beltana willemite mine, Flinders Ranges, South Australia.

A BRIEF INTRODUCTION TO IN-SITU PRODUCED TERRESTRIAL COSMOGENIC NUCLIDE METHODS

Derek Fabel[1,2]

[1]*CRC LEME, Research School of Earth Sciences, ANU, Canberra, ACT, 0200*
[2]*Dept. of Geographical & Earth Sciences, Glasgow University, Glasgow, G12 8QQ, UK*

INTRODUCTION

The Earth is continually being bombarded by high-energy primary cosmic rays that originate predominantly from super nova explosions within our galaxy. Interactions between these high-energy cosmic rays and the Earth's atmosphere, creates secondary cosmic rays, as well as neutrons and muons. When reaching the Earth's surface, these high-energy particles can penetrate metres into rock and sediment. Nuclear interactions between neutrons and muons produce long-lived radionuclides and stable nuclides in terrestrial materials (Table 1.).

Table 1. Major *in-situ* produced cosmogenic nuclides in terrestrial materials.

Nuclide	Half-life (yr)	Major targets in terrestrial rocks
^{14}C	5,730	O
^{41}Ca	1.04×10^5	Ca, Ti, Fe
^{36}Cl	3.01×10^5	Cl, K, Ca, Fe
^{26}Al	7.05×10^5	Si
^{10}Be	1.5×10^6	O
^{53}Mn	3.7×10^6	Fe
^{129}I	1.56×10^7	Te, Be, Rare Earth Elements
^{3}He	stable	O, Mg, Si, Fe
^{21}Ne	stable	Mg, Al, Si
$^{36, 38}Ar$	stable	Cl, K, Ca, Fe

The production rates of these in-situ produced terrestrial cosmogenic nuclides (TCN) are almost unimaginably small - a few atoms per gram of rock per year, however, using accelerator mass spectrometry (AMS) and noble gas mass spectrometry (NGMS) we can detect and count cosmogenic nuclides down to levels of a few thousand atoms per gram (parts per billion of parts per billion!). The build-up of TCNs through time provides us with a way to measure exposure ages and/or erosion rates for geomorphological surfaces directly from the mineral constituents of the surfaces. Additionally, when previously exposed rock or sediment is deeply re-buried, the relative decay between different cosmogenic nuclides can be used to estimate the burial time.

The aim of this short paper is to briefly explain TCN methods focusing on the nuclides ^{10}Be, ^{26}Al, and ^{21}Ne produced in quartz and currently being utilised at Research School of Earth Sciences, ANU. For a detailed review of the TCN technique see (Gosse & Phillips 2001).

TCN PRODUCTION RATES

The rate of TCN production depends on the cosmic ray flux, which in turn depends largely on the modulation of the primary galactic cosmic ray flux by the Earth's magnetic field, and attenuation of the secondary flux by the Earth's atmosphere (Lal & Peters 1967; Stone 2000; Dunai 2000; Dunai 2001; Gosse & Phillips 2001;). This means TCN production is greater at high latitude because primary cosmic rays are deflected more strongly by the magnetic field at the equator than at the poles, and it is greater at high altitude because the secondary cosmic ray flux attenuates with increasing atmospheric depth (Fig. 1). Thus, TCN production at a location on the earth surface is dependent on its geomagnetic latitude and altitude.

It is also dependent on the geometry of the sample site because decreases in the rates of production occur as a result of shielding of cosmic rays by mountains, sloped surfaces, and local rock formations that block them.

The extent of sample shielding by surrounding topography and sample geometry can be accounted for in models of geometric and shielding corrections, based on measuring sample-surface inclination and vertical angles to the horizon (Dunne *et al*. 1999).

Production rates for ^{10}Be (5.1 ± 0.3 atom/g-quartz/yr), ^{26}Al (31.1 ± 1.9 atom/g-quartz/yr), and ^{21}Ne (19.0 ± 3.7 atom/g-quartz/yr) have been determined from independently dated calibration sites (e.g. Niedermann 2000; Stone 2000; Stone *et al*. 1998) and scaled to sea-level high-latitude (>60°) using relatively well-constrained relationships between TCN production rate, latitude and altitude (Dunai 2000; Dunai 2001; Lal 1991; Stone 2000). However, uncertainties remain on the order of 10% because, (1) the neutron flux distribution at the Earth's surface, as well as the nuclear cross-sections for the production reactions, are not known with sufficient accuracy, and (2) contemporary production rates are not constant due to temporal changes of the Earth's geomagnetic field or altitude as seen by the sample.

For quartz on the surface, the production rate of ^{10}Be and ^{26}Al due to neutrons is much larger than that due to muons. However, muons penetrate much further than nucleons, so that at sufficient depth production by muons becomes dominant (Fig. 2). Production by nucleons as a function of depth can be accurately modelled by a simple exponential law (Brown *et al*. 1992; Lal 1991):

$$P_n(z) = P_n \, e^{-z/L0} \qquad (1)$$

where P is the production rate and subscript n denotes nucleonic production; z is depth below the surface, and nucleon attenuation length is given by $L_0 \approx 160/\rho$ cm (Reedy *et al*. 1994), where ρ is the density of the overburden (in g/cm^3). Muon production as a function of depth is not readily modelled by a simple analytical expression, however, production by muons can be modelled using the sum of three exponential terms (Granger & Muzikar 2001; Granger & Smith 2000), leading to the more complete equation for production as a function of depth:

$$P(z) = P_n \, e^{-z/L0} + P_1 \, e^{-z/L1} + P_2 \, e^{-z/L2} + P_3 \, e^{-z/L3} \qquad (2)$$

where P_1 and P_2 are constants related to production by slow muons (0.096 and 0.021 for Be and 0.723 and 0.156 for Al respectively), P_3 is a constant related to production by fast muons (0.026 and 0.192 for Be and Al respectively), and L_1, L_2, and L_3 are attenuation lengths (738/ρ cm, 2688/ρ cm, 4360/ρ cm).

For many geomorphological scenarios, TCN production by muons does not significantly contribute to the TCN abundance in a sample. However, in situations where surfaces are eroding at rates between 1m/Ma and 10 m/Ma, or where burial of clasts is not sufficiently deep, ignoring muon production can lead to significant errors in modelled erosion rates or burial times (Granger & Muzikar 2001). For the sake of simplicity muons will be ignored in this article.

SURFACE EXPOSURE DATING AND EROSION RATES

Surface exposure dating has been the most widely used TCN method in the earth sciences. In essence, the abundance of a TCN in a rock surface is a measure of its exposure time. The method is best suited to dating events that expose freshly excavated rock for the first time, such as volcanic eruptions, landslides, faults, and glacial retreat.

For scenarios where it is clear that surfaces have experienced a simple, single-stage exposure history (no erosion or burial since first exposure) the TCN concentration at the surface, $N(0)$, accumulates as a function of time according to (Lal, 1991):

$$N(0) = P(0)/\lambda\ (1 - e^{-\lambda T}) \quad (3)$$

for radionuclides, and for stable nuclides:

$$N(0) = P(0)T \quad (4)$$

where $P(0)$ is the TCN production rate at the surface, λ is the radioactive decay constant, and T is the exposure time (Fig. 3). The upper limit of exposure dating depends on the nuclide used, and in the case of radionuclides in a non-eroding surface, is determined by when secular equilibrium is approached, which occurs in 4 – 5 half-lives.

The short attenuation length for TCN production imposes stringent constraints on the amounts of erosion or burial of a surface that can be tolerated without loss of dating accuracy. Because the continual creation of new surfaces by erosion uncovers formerly shielded material, eroded surfaces carry lower TCN concentrations than well-preserved surfaces of the same age (Fig. 4). A more sophisticated (and usually more realistic) model for the build-up of TCN at the surface is needed to take into account surface erosion:

$$N(0) = [P_n(0)/\lambda+\rho\varepsilon/L_0.]\ (1 - e^{-(\lambda+\rho\varepsilon/L0)T}) + N_{inh}\ e^{-\lambda T} \quad (5)$$

where N_{inh} is any inherited TCN concentration from a prior exposure period, and ε is erosion rate. Equation 5 assumes that the depth dependence of TCN production follows a simple exponential law. This is a reasonable assumption for erosion rates much greater than 10 m/Ma and less than 1 m/Ma (Granger & Muzikar 2001). For surfaces eroding at rates between these upper and lower limits a more complete equation, incorporating both nucleon and muon production should be used (Granger & Muzikar 2001).

Using Equations 5 to calculate surface exposure time (T) from a measured TCN concentration (N) requires that the steady-state erosion rate of the surface (ε) is known. In the absence of independent surface exposure age or erosion rate evidence there is no unique solution to the equation, rather, the inferred results consist of paired erosion rates and exposure ages. If we assume the surface erosion rate to be zero, the calculated apparent exposure time represents a minimum for the surface.

Although, independent age control is often not available, steady-state erosion rates can be calculated. Because of the depth-dependence of TCN production (Equations 1 and 2), the accumulated TCN concentration in a mineral grain records the speed with which that grain has been uncovered; slower erosion rates imply longer exposure times (Figure 4). Lal (1991) showed that the TCN concentration (N) in a steadily eroding surface is inversely proportional to the outcrop's erosion rate (ε):

$$N(0) = [P_n(0)/(\lambda+\rho\varepsilon/L_0)] \quad (6)$$

N averages the erosion rate over the time required to erode a layer of thickness $\approx L_0/\rho$ from the surface. Equation 6 assumes that the half-life, λ, is much longer than $L_0/\rho\varepsilon$ and that the erosion rate is constant in time.

PAIRED TCN ANALYSES

It has been shown that the ratio of two TCN concentrations with different decay rates in the same sample varies with exposure time and erosion rate (Lal 1991). It is therefore possible to simultaneously calculate an exposure age and erosion rate for a sample by measuring the concentration of two TCN.

In quartz, ^{26}Al is produced approximately six times faster than ^{10}Be, regardless of the absolute production rate, but ^{26}Al decays more than twice as fast as ^{10}Be (Table 1). If quartz-bearing material

accumulates ^{26}Al and ^{10}Be while exposed at the surface the ^{26}Al/^{10}Be ratio at the time of production will be 6.1 (using the production rates given above).

However, as the exposure time of the surface increases the relative decay between ^{26}Al and ^{10}Be lowers the ^{26}Al/^{10}Be ratio in the surface until secular equilibrium is reached (Figure 5). For an eroding surface secular equilibrium is reached earlier (Fig. 4). The ^{26}Al/^{10}Be ratio in rapidly eroding surface the remains at the production rate ratio of 6.1 because the time it takes for a quartz grain to pass through the TCN production zone is too short for the effects of decay to be apparent. Therefore, calculating the exposure time and steady-state erosion is only possible when the erosion rate is less than 10 m/Ma. It is not possible to determine very slow erosion rates using the ^{26}Al/^{10}Be system because of insufficient analytical precision.

However, by measuring stable ^{21}Ne and radiogenic ^{10}Be in the same quartz sample it is theoretically possible to use the ratio between these two nuclides to determine much slower steady-state erosion rates (Fig. 6). The ^{10}Be/ ^{21}Ne systematics are currently being explored at RSES, ANU.

BURIAL DATING

If a quartz-bearing material accumulates ^{26}Al and ^{10}Be while exposed at the surface and is subsequently buried deep enough that it is completely shielded from cosmic rays (e.g. by deposition in a cave, sedimentary deposit, or deep water body), then the ^{26}Al/^{10}Be ratio will diminish over time, recording the time since burial, according to (Granger and Muzikar 2001):

$$N_{26} = (N_{26})_i \, e^{-\lambda 26 T burial} \quad (7)$$

and

$$N_{10} = (N_{10})_i \, e^{-\lambda 10 T burial} \quad (8)$$

where T_{burial} is the time since burial and $(N_{26})_i$ and $(N_{10})_i$ represent initial ^{26}Al and ^{10}Be concentrations. Because ^{26}Al decays faster than ^{10}Be, the ratio N_{26}/ N_{10} decreases exponentially over time (Figure 7):

$$N_{26}/ N_{10} = (N_{26}/N_{10})_i \, e^{-(\lambda 26 - \lambda 10) \, T burial} \quad (9)$$

Equations 7-9 can be solved iteratively and, as illustrated in Figure 8 can be used to calculate the burial time and pre-burial steady-state erosion rate (Granger *et al*. 2001; Granger *et al*. 1997).

Geological requirements for the method to be applicable are simply that (1) quartz must be exposed at the surface for long enough to accumulate measurable cosmogenic radionuclide concentrations (typically >10 ka), (2) the quartz must be buried quickly with respect to radioactive decay, (3) the quartz must be buried deeply with respect to cosmic ray penetration (typically >10 m), and (4) the sediment must have a simple history of exposure prior to burial, i.e. no inherited TCN concentration.

The age range of burial dating, using ^{10}Be and ^{26}Al, is of the order of 100 kyr to 5 Myr. The lower value is essentially a matter of experimental error, while the upper limit is a function of the AMS detection limit of the order of 10^{-15} for the ratios ^{26}Al/^{27}Al and ^{10}Be/^{9}Be.

HOW MUCH SAMPLE IS NEEDED?

Field sampling sites do not always provide samples characterised by suitable lithology and ideal geometry. The minimum amount of sample varies depending on the TCN used, exposure duration, site-specific production rate, proportion of mineral phases sought, and nature of the analysis (AMS or NGMS). The aim is to collect enough mass so that sufficient nuclides can be extracted or released to make a measurement at the desired level of confidence.

If the aim is to distinguish between a lava that was emplaced 1 Myr ago and 50 kyr ago, or if it is only necessary to determine the relative ages of two or more samples, then lower precision may be tolerated and a smaller sample mass may suffice. However, if the aim is to distinguish between moraines of 15 kyr and 12 kyr, larger samples are needed to attain the required level of precision.

Prior to sampling it is useful to calculate approximately how much sample is needed (Table 2).

Table 2. What is the minimum amount of sample needed?

An example for ^{10}Be from an estimated 6 kyr-old east Australian shore platform	
Estimated surface exposure age	6,000 yrs
Site production rate (adjust for shielding, uplift, erosion)	4.5 atoms ^{10}Be per g qtz/ yr
Estimated concentration of ^{10}Be in quartz	27000 atoms ^{10}Be per g qtz
Desired minimum AMS ^{10}Be/^{9}Be	5 x 10^{-14} atoms ^{10}Be/atoms ^{9}Be
Desired mass BeO used (for 30 minute analysis)	0.5 mg
Number of ^{10}Be atoms in 0.5 mg BeO (assuming pure BeO):	1.2 x 10^{19} atoms ^{9}Be
(0.0005 g BeO · 9/25 g Be/g BeO) / 9.0 g/mol · 6 x 10^{23} atom/mol =	
Number ^{10}Be atoms needed for desired ratio:	600,000 atoms ^{10}Be from the qtz
5 x 10^{-14} ^{10}Be/^{9}Be · 1.2 x 10^{19} atoms ^{9}Be /mg BeO =	
Mass of pure quartz to dissolve:	22.2 g pure qtz
600,000 atoms ^{10}Be / 27000 atoms ^{10}Be per g qtz =	
40% of the quartz is lost to remove meteoric ^{10}Be:	37 g qtz
22.2 / 60% =	
Rock contained 35% quartz:	105.7 g rock
37 / 35% =	
Only 40% of crushed rock has the proper grain size:	264 g rock from site
105.7 / 40% =	

The noble gas TCN have the significant advantage of requiring only a few grams of the target grains, although a few hundred grams of rock are often needed to obtain those grains.

SAMPLE PREPARATION

The aims of sample preparation are to purify the field specimen of materials not suitable for analysis, to concentrate the nuclide of interest sufficiently that it can be accurately analysed, and to transform the sample material into a form suitable for analysis. The sample preparation consists of two parts: (1) a pre-treatment phase in which target minerals are separated, concentrated, and purified; and (2) an isotope extraction phase in which the isotopes are isolated from the minerals and separated from non-in situ cosmogenic isotopes. The amount of time required for sample preparation varies widely, depending on the nuclide, its concentration, and rock lithology.

For ^{10}Be and ^{26}Al the preparation time is usually more than four weeks because of the the time necessary to concentrate the target mineral from the sample, and the time to extract the radioisotopes from the minerals and prepare them in a form suitable for AMS analysis. Preparing quartz for ^{21}Ne tends to be less time consuming, because after isolating and purifying the quartz the samples do not

require chemical preparation before analysis. Table 3 provides a broad outline of the steps required to prepare AMS target material for ^{10}Be and ^{26}Al analysis.

Table 3. Summary of sample preparation for ^{10}Be and ^{26}Al analysis

Physical and chemical pre-treatment:	Wash or brush to remove organics, dust etc
	Crush, grind, and sieve to 250 – 500 micron size
	Wash with water to remove fines
	Bulk magnetic separation
	Remove carbonates (and metals) with aqua regia
	Heavy liquid separation
	Differential leaching in HF and nitric acid, or pyrophosphoric acid
	Test for quartz purity using AAS or ICP-OES
Isotope extraction:	Add native element carrier (^{9}Be or ^{27}Al if necessary) to pre-determined mass of quartz
	Digest quartz in HF
	Elemental analysis of Al and Be by ICP-OES
	Anion chromatography to remove Fe, Ti and other cations
	Cation chromatography to separate Al from Be
	Precipitate $Al(OH)_3$ and $Be(OH)_2$
	Oxidise hydroxides and analyse by AMS

CONCLUSIONS

Terrestrial cosmogenic nuclides (TCN) are an extremely powerful tool for understanding both the history of the surface of the earth and rates of geological and geomorphic processes. Cosmogenic nuclide methods have rapidly supplanted older techniques for dating geomorphic surfaces. In contrast to methods with environmental and sample-specific dependencies, the TCN method has a solid quantitative foundation in nuclear and cosmic-ray physics.

TCN methods have been used to date landforms that constitute records of palaeoclimate fluctuations such as glacial moraines, river terraces, lacustrine and marine shorelines, flood deposits, and many more. In tectonics, TCN are widely used to date surfaces offset by either normal or strike-slip faults. In addition, bedrock fault surfaces can be dated directly. In geomorphology, the use of TCN allows direct quantification of landscape evolution at scales ranging from single outcrops to entire river basins. The development of the TCN technique has played a significant role in elevating the study of landscape evolution from its past status as a highly qualitative field that had fallen into disfavour, to a current position of intense interest in the geosciences. Here various aspects of the TCN method are briefly outlined, focusing on the theory and sample requirements, in order to facilitate a better understanding of the technique within the broader Earth sciences community whose primary concerns are geology and geomorphology.

REFERENCES

BROWN E.T., BROOK E.J., RAISBECK G.M., YIOU, F. & KURZ M.D. 1992. Effective attenuation length of cosmic rays producing 10-Be and 26-Al in quartz: Implications for exposure age dating. *Geophysical Research Letters* **19(4)**: 369-372.

DUNAI T.J. 2000. Scaling factors for the production rates of in-situ produced cosmogenic nuclides: a critical reevaluation. *Earth and Planetary Science Letters* **176(1)**: 159-171.

DUNAI T.J. 2001. Influence of secular variation of the geomagnetic field on production rates of in situ produced cosmogenic nuclides. *Earth and Planetary Science Letters* **193(1-2)**: 197-212.

DUNNE J., ELMORE D. & MUZIKAR, P. 1999. Scaling factors for the rates of production of cosmogenic nuclides for geometric shielding and attenuation at depth on sloped surfaces. *Geomorphology* **27(1-2)**: 3-11.

GOSSE J.C. & PHILLIPS F.M. 2001. Terrestrial in situ cosmogenic nuclides: theory and application. *Quaternary Science Reviews* **20(14)**: 1475-1560.

GRANGER D.E., FABEL D. & PALMER A.N. 2001. Plio-Pleistocene incision of the Green River, Kentucky, from radioactive decay of cosmogenic ^{26}Al and ^{10}Be in Mammoth Cave sediments. *Geological Society of America Bulletin* **113(7)**: 825-836.

GRANGER D.E., KIRCHNER J.W. & FINKEL, R. 1997. Quaternary downcutting rate of the New River, Virginia, measured from differential decay of cosmogenic ^{26}Al and ^{10}Be in cave-deposited alluvium. *Geology* **25(2)**: 107-110.

GRANGER D.E. & MUZIKAR P.F. 2001. Dating sediment burial with in situ-produced cosmogenic nuclides: Theory, techniques, and limitations. *Earth and Planetary Science Letters* **188(1-2)**: 269-281.

GRANGER D.E. & SMITH A.L. 2000. Dating buried sediments using radioactive decay and muogenic production of ^{26}Al and ^{10}Be. *Nuclear Instruments and Methods in Physics Research B* **172(1-4)**: 822-826.

LAL D. 1991. Cosmic-ray labeling of erosion surfaces: in situ nuclide production rates and erosion models. *Earth and Planetary Science Letters* **104**: 424-439.

LAL D. & PETERS B. 1967. Cosmic-ray produced radioactivity on the earth. *Handbook of Physics* **46(2)**: 551-612.

NIEDERMANN S. 2000. The ^{21}Ne production rate in quartz revisited. *Earth and Planetary Science Letters* **183(3-4)**: 361-364.

REEDY, R.C. et al., 1994. Simulations of terrestrial in-situ cosmogenic nuclide production. *Nuclear Instruments & Methods in Physics Research B* **92**: 297-300.

STONE J.O. 2000. Air pressure and cosmogenic isotope production. *Journal of Geophysical Research* **105(B10)**: 23753-23759.

STONE J.O., BALLANTYNE C.K. & FIFIELD L.K. 1998. Exposure dating and validation of periglacial weathering limits, northwest Scotland. *Geology* **26(7)**: 587-590.

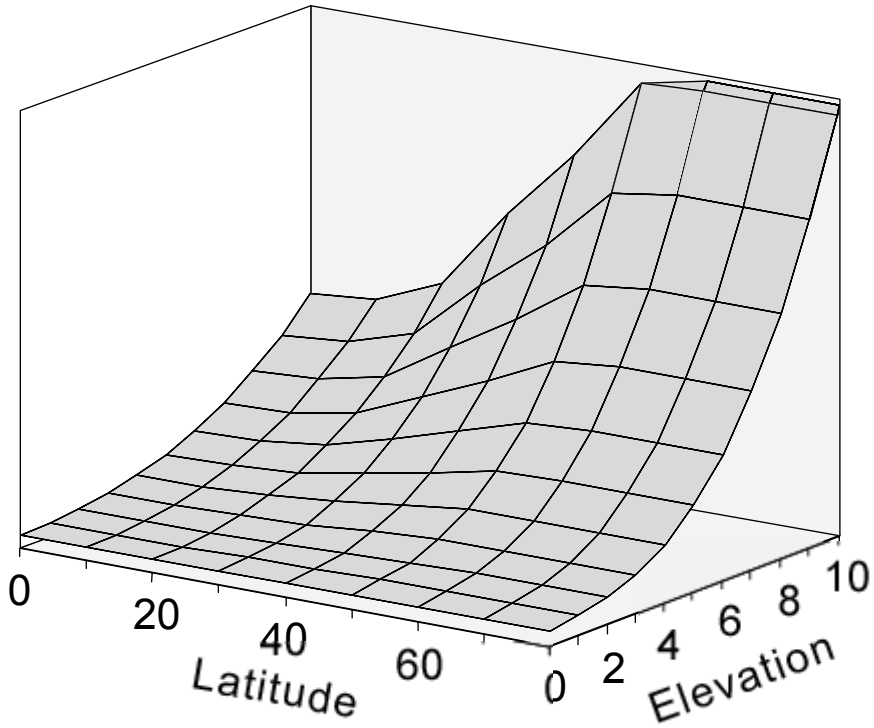

Figure 1. Variation of cosmic ray flux at the earth's surface as a function of altitude and latitude.

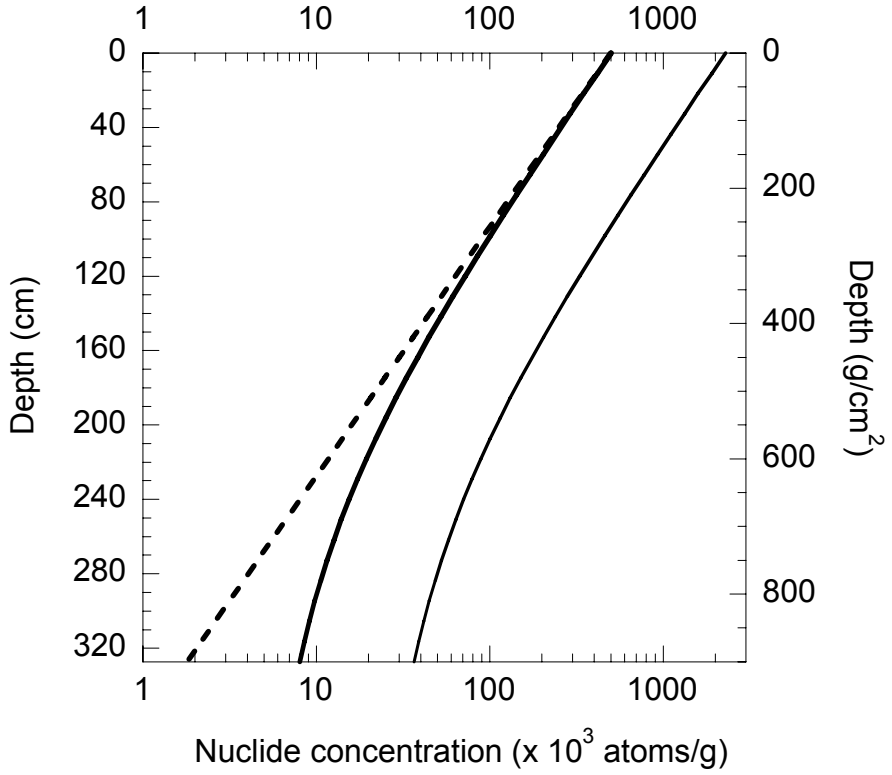

Figure 2. ^{10}Be concentration vs. depth after 100 ka exposure calculated using Equation 1 for nucleon production (dashed line) and Equation 2 for combined nucleon and muon production (solid curve) with a surface production rate of 5.1 atoms g^{-1} a^{-1}, a rock density of 2.75 g cm^{-3} and no erosion. Note the divergence of the curves and the resulting difference in depth estimates if muon production is neglected. The fine dotted curve shows the ^{10}Be concentration vs. depth after 500 ka exposure calculated using equation 2.

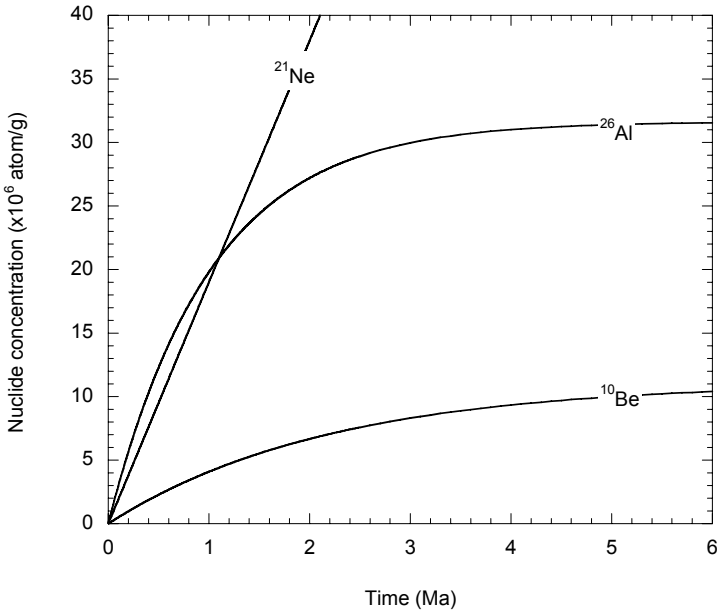

Figure 3. Increase in concentration of the radionuclides ^{10}Be, ^{26}Al, and the stable nuclide ^{21}Ne with time in quartz exposed at the surface of a flat, unshielded, non-eroding outcrop, calculated using Equation 3 and 4 using sea level, high latitude production rates mentioned in the text. For the radionuclides, secular equilibrium (production by cosmic rays = radioactive decay) is approached after 4-5 half-lives, setting the limit of the maximum exposure age that can be determined.

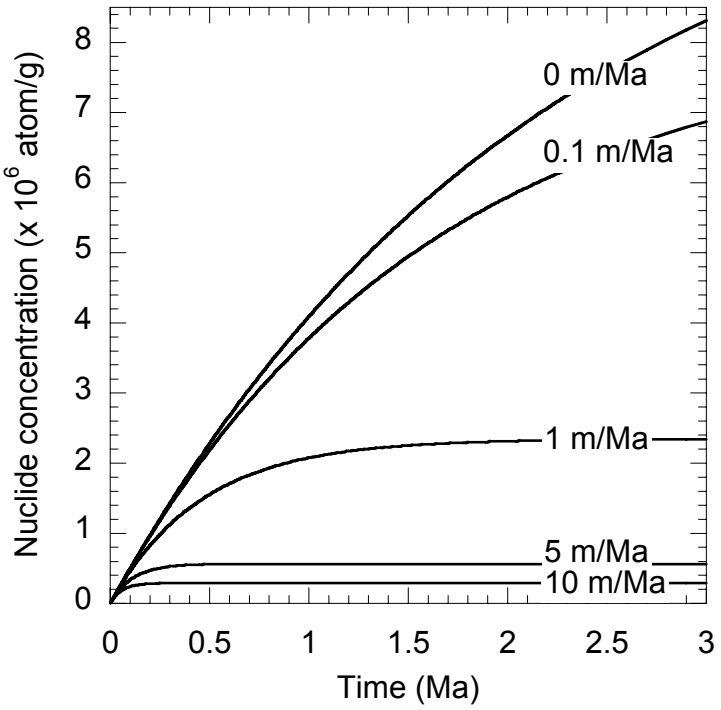

Figure 4. Increase in surface concentration of ^{10}Be with time for different steady-state erosion rates calculated using Equation 5 and sea level, high latitude production rates mentioned in the text.

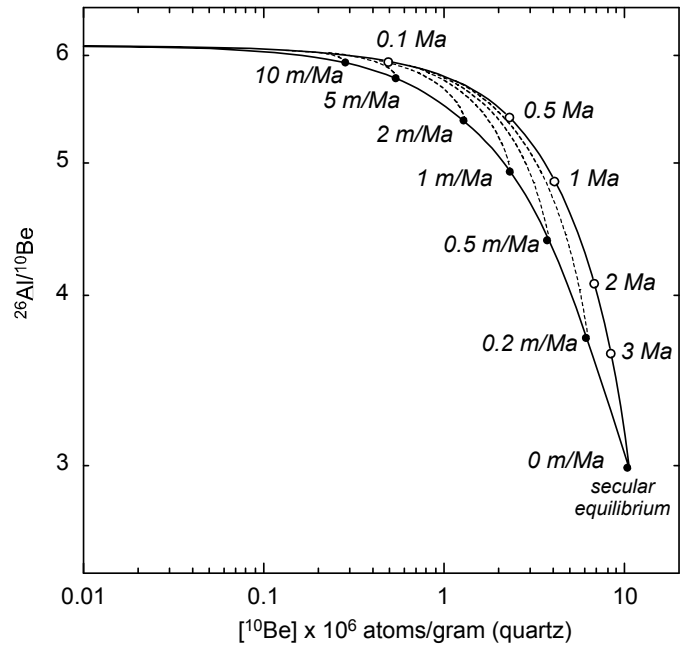

Figure 5. Plot of ^{10}Be concentration vs. ^{26}Al/^{10}Be (also referred to a 'banana-plot'). Continuously exposed samples fall on the curve connecting the open circles labelled with exposure time. Steadily eroding samples lie on the lower curve connecting the labelled steady-state erosion end points (solid dots). The dashed curves show the trajectory of samples within the ^{10}Be concentration vs. ^{26}Al/^{10}Be space for the given steady-state erosion rates. The area bounded by the continuous exposure and steady-state erosion curves is known as the "steady-state erosion island" (Lal 1991). Given a simple exposure history and assuming constant production rate ratios, all samples collected at the earth's surface must lie within the steady-state erosion island. Samples that lie below the steady-state erosion island have experienced a complex history, which may include burial or non-steady state erosion in the sample's recent history.

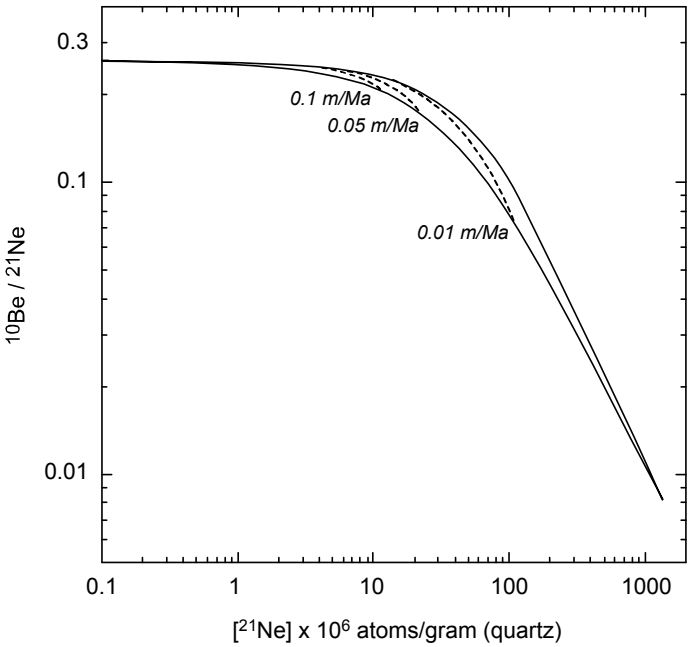

Figure 6. Plot of ^{21}Ne concentration vs. ^{10}Be/^{21}Ne. As in Figure 5, the upper curve represents the continuous exposure trajectory, while the lower curve indicates the steady-state erosion end points. The dashed lines show the sample trajectories for the labelled erosion rates. Note the improved resolution at lower erosion rates compared to using ^{26}Al and ^{10}Be (Figure 5).

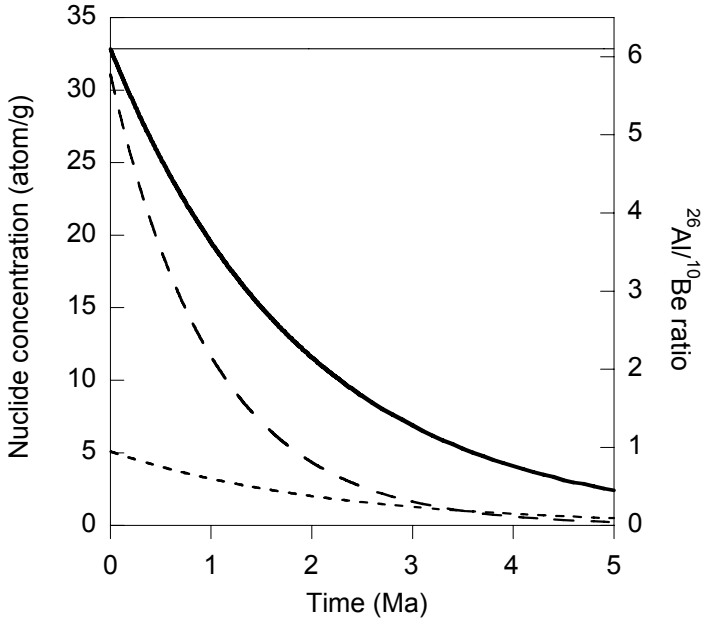

Figure 7. Decay of ^{26}Al (long dashed curve) and ^{10}Be (short dashed curve), and the ^{26}Al/^{10}Be ratio (solid curve) as a function of time.

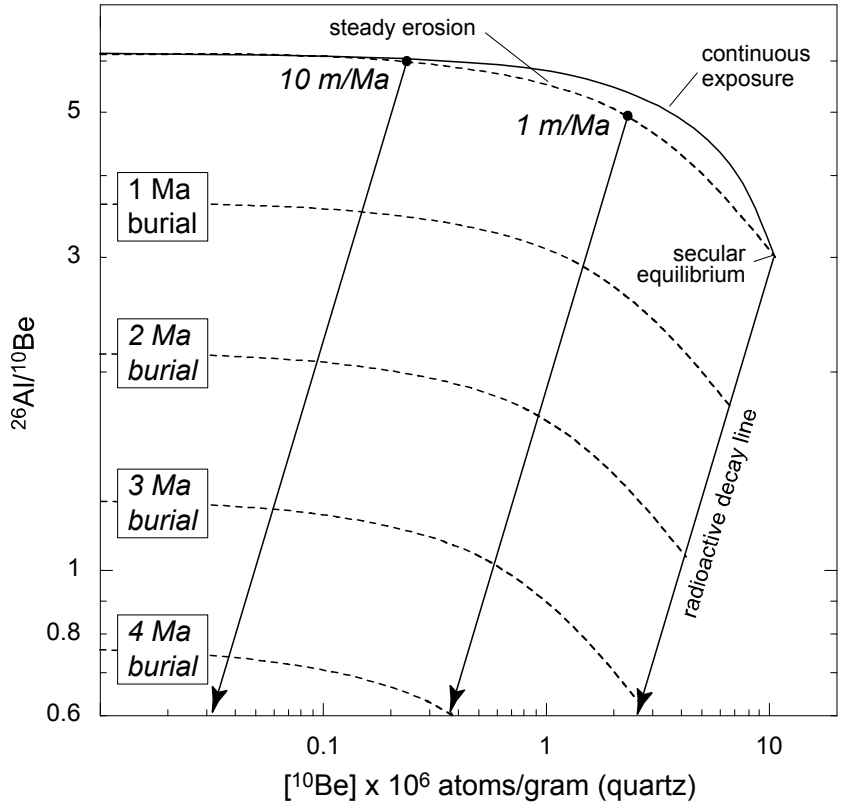

Figure 8. Burial dating plot showing the ^{10}Be concentration and ^{26}Al/^{10}Be ratio in sediment or rock. Quartz with no burial history should plot between the steady erosion and continuous exposure curves (see Figure 5). For quartz that is buried and completely shielded from cosmic rays, the ^{26}Al/^{10}Be decreases along a line parallel to the solid 'radioactive decay line'. The measured ^{26}Al/^{10}Be ratio in a sample determines the burial time, and can also be used to calculate the pre-burial erosion rate. Million-year isochrones are shown for quartz burial following steady erosion.

AUSTRALIAN LANDSCAPE PROCESSES MEASURED WITH COSMOGENIC NUCLIDES

John Chappell

CRC LEME, Research School of Earth Sciences, ANU, Canberra, ACT, 0200

INTRODUCTION

Owing to the movement of particles and solutes, together with the formation of secondary minerals, regolith stratigraphy tends to be complex. In contrast with sedimentary basins, where the record of history follows the rule that upwards-is-younger, the time dimension in regolith varies in direction and scale. Although regolith may show visible horizonation, age-structures often lack "upness". At the field-profile scale, the ages of specific secondary minerals may become younger as depth increases, while at the hand-specimen scale, concentric age-structures are common. In describing regolith geology of the Yilgarn craton, Anand & Paine (2002) emphasise that to understand this complex material, knowledge of processes and rates is necessary at all scales, from microscopic to regional.

Advances in various dating methods provide the means for measuring the rates at which regolith is produced from rock weathering, as well as rates of mixing and transport, and the residence time of regolith-derived sediment in colluvial mantles, floodplains and rivers. In Australia, these processes tend to be very slow and rates are difficult to assess by direct observations. Moreover, owing to the effects of climatic changes in the past, processes acting today often are not typical of those that acted throughout the history of regolith formation.

Nuclides produced in surface rocks and sediments by cosmic ray reactions ("terrestrial cosmogenic nuclides", or TCNs) are powerful tools for determining regolith history. Some TCNs are radioactive, others are stable, and the production of all TCNs diminishes with depth below the ground surface. Lal (1991) analysed the potential of TCNs for resolving a variety of earth-surface processes, and TCNs have since become a powerful tool for evaluating many aspects of landscape and regolith history, including surface exposure ages, erosion rates and, in the case of buried materials, their burial history. However, owing to their very low abundances in surface materials, the measurement of TCNs requires highly specialised methods. Fabel (this volume) reviews the natural production, sample preparation and measurement of TCNs, while the present paper reviews a number of recent applications in Australian landscape studies. To assist the review, the basic principles underlying the application of TCNs to such studies are briefly summarised below, but for a fuller acount the reader should turn to Fabel (this volume), while extensive bibliographies together with further details of principles and methods can be found in Cerling & Craig (1994), Tuniz *et al*. (1998), Fifield (1999) and Bierman *et al.* (2002).

The most widely-used TCNs for determining exposure and erosion histories of rock surfaces and regolith are radioactive ^{10}Be (½-life 1.52 Ma) and ^{26}Al (0.72 Ma), which are produced by cosmic rays from oxygen and silicon atoms, respectively, in rocks or deposits within a few metres of the ground surface. Quartz is the preferred mineral, as it is widespread, and is relatively easily separated and cleaned. ^{36}Cl (½-life 0.35 Ma), produced from Cl, K, Ca and Fe, is used for non-quartzose rocks such as basalt and limestone, although its determination is more demanding than ^{10}Be. The stable nuclide ^{21}Ne is also produced cosmogenically from Si, Al and Mg in rock minerals, and can advantageously be used for evaluating regolith histories beyond the range of radioactive TCNs. However, ^{21}Ne is also generated by non-cosmogenic processes, and determination of the TCN component is relatively complex (Fujioka *et al*. 2005).

PRINCIPLES

TCNs are produced by nuclear interactions of nucleons and muons generated by cosmic rays with nuclei in terrestrial materials. Nucleon reactions (e.g. spallation by neutrons) dominate within a few metres of the surface; muon reactions are quantitatively less important but penetrate to over 10 m depth (Lal, 1991; Bierman *et al*. 2002; Fabel, this volume). Production rates depend on the local flux

of cosmic rays, which varies with latitude and altitude; hence, TCN data are usually normalised to sea level and high latitude, using normalisation methods established by Lal (1991) and later recalibrated (Stone 2000; Bierman *et al*. 2002).

The amount of a given TCN in a given volume of near-surface material depends on its history of exposure and erosion: in general, the TCN content increases with the duration of exposure, but if a rock surface is reburied, radioactive TCNs produced during prior exposure begin to decay. Following exposure by rapid removal of a substantial cover (equivalent to >10 m of rock), TCNs will accumulate within minerals at the rock surface. Lal (1991) showed that the concentration N of a radioactive TCN in a surface of *exposure age t*, eroding at a uniform rate ε, and with no prior exposure history, is

$$N = P_o\,[1 - \exp(-(\lambda + \mu\varepsilon)t)]/(\lambda + \mu\varepsilon) \qquad (1)$$

where P_o is the production rate of a given TCN at the ground surface (atoms $g^{-1}yr^{-1}$) and λ is the radioactive decay constant. The term $\mu = \rho/\Lambda$ where Λ is the absorption mean free path for nuclear interacting particle ($g.cm^{-2}$) and ρ is rock or regolith density ($g.cm^{-3}$) (the notation follows Lal, 1991; Fabel in this volume uses similar notation except that he writes $1/L_o$ where we use μ). If erosion is zero, (1) reduces to the following expression for exposure age:

$$N(t) = P_o\,\lambda^{-1}(1 - \exp(-\lambda t)) \qquad (2)$$

Under continuous uniform erosion, (when $t >> 1/(\lambda + \mu\varepsilon)$) the TCN concentration depends only on the erosion rate ε. At depth H below the surface (where H is less than a few metres, so that TCN production is dominated by cosmic-ray nucleons), the TCN content is given by

$$N(z) = P_o \exp(-\mu H)/(\lambda + \mu\varepsilon) \qquad (3)$$

The situation is more complex for a previously-exposed surface is later buried, or for sediment derived from an eroding source. The TCN concentration at burial depth z is

$$N(h) = N_o \exp(-\lambda t^*) + P_o \lambda^{-1} \exp(-\mu z).(1 - \exp(-\lambda t^*)) \qquad (4)$$

where $t*$ is the time elapsed after burial and N_o is the nuclide concentration immediately before burial (given by equation 2 for a previously-exposed surface, or equation 3 for sediment from a uniformly eroding source). As N_o and $t*$ are both unknowns, neither can be determined from a measurement of a single TCN but, if the burial depth (z) is known and can be assumed to have remained constant, both N_o and $t*$ can be determined from measurement of a pair of TCNs with different half-lives, using iterative computational methods (see Granger & Muzikar, 2001; Fabel, this volume).

EXPOSURE DATING AND LONG-TERM EROSION RATES: AUSTRALIAN EXAMPLES

TCN exposure dating has been used in a variety of Australian landscape settings, from Late Pleistocene glacial landforms in southeast Australia to ancient silcrete pavements in the Lake Eyre basin. Using ^{10}Be and ^{36}Cl for exposure-age dating of moraine deposits, Barrows *et al* (2001; 2002) found that the last major advance of former glaciers at a comprehensive range of sites in the Snowy Mountains and Tasmanian high country occurred between at 17,000 and 20,000 years ago, very close to the timing of the Last Glacial Maximum in the northern hemisphere. Kiernan *et al*. (2004) reported similar results from southwest Tasmania.

In contrast to these glacial features, which are amongst Australia's youngest landforms, evidence of several types including the dating of secondary regolith minerals has shown that rock surfaces and surficial deposits elsewhere in Australia, particularly in the arid interior, are very much older (Pillans 2005, and this volume).

TCN data from semi-arid landforms are discussed in the next paragraph; however, at this juncture it is useful to cite an example where TCN measurements have shown that surficial deposits in the stony desert west of Lake Eyre are of pre-Quaternary exposure age: using paired ^{10}Be and ^{21}Ne, Fujioka *et al*. (2005) reported exposure ages of 2 – 4 Ma for stony clasts ("gibbers") in the western Lake Eyre Basin.

To obtain exposure ages such as these, it is assumed that erosion has been negligible (Equation 1 shows that the TCN content depends on both ε and t, unless $t >> 1/(\lambda + \mu\varepsilon)$). In the case of glacial landforms, preserved glacial grooves in the hard rock surfaces support this assumption. In general, however, most bedrock landforms are the product of long-term erosion.

Where field evidence indicates that a bedrock landform has existed without any soil or surficial mantle for a very long time, it is more realistic to use TCN data to gauge the long-term erosion rate of the bedrock surface, using Equation 3, rather than to derive an exposure age. Thus, TCN measurements have been used to evaluate long-term erosion rates at a variety of Australian sites.

Table 1 summarises TCN data from Australian erosion and soil production studies. At the low end of the spectrum, erosion rates determined from granitic residual hills (inselbergs) in the Eyre Peninsular sites range from below 0.3 m Ma^{-1} to 5.7 m Ma^{-1} (Bierman & Caffee, 2002). Table 1 shows that rates reported from low-relief granitic surfaces near Katherine, Northern Territory (Bierman & Caffee, 2002), and from low ridges comprised of banded iron formation rocks in the eastern goldfields of Western Australia (Chappell, 2003), are similarly slow. Steep rocky slopes in jointed quartzite in the Flinders Ranges yielded higher rates (~2 to 12 m Ma^{-1}; Table 1). From sites in the more humid eastern highlands, apparent erosion rates from about 9 to over 20 m Ma^{-1} are reported from granite tors in the headwalls of the Bega Valley and from sandstone crags ("pagodas") in the Blue Mountains of NSW (Heimsath *et al*. 2000; Wilkinson *et al*. 2005). In all these studies, the range of erosion rate estimates at any given site is significant, relative to the mean (coefficients of variation range from 0.4 to 0.9). Although this may reflect true variation of erosion rate across a landform with a complex history (Bierman & Caffee, 2002), such variability is also likely to reflect local departures from uniform erosion, occasioned by irregular, sub-metre-scale exfoliation or surface break-up.

Table 1: Typical TCN erosion rates from Australia

Site	^{10}Be x 10^6 a g^{-1}	Exposure age x 10^3 years*	Erosion rate m Ma^{-1}**
Inselbergs, Eyre Peninsula (BC02)			
Lowest ^{10}Be		0.53 105	5.68
Highest ^{10}Be		5.09 1313	0.34
Mean (67 samples)		651	1.31
Coeff. of variation		0.53	0.91
Bedrock surfaces, Northern Territory (BC02)			
Lowest ^{10}Be	0.79	158	3.72
Highest ^{10}Be	2.90	650	0.81
Mean (19 samples)		320	2.24
Coeff. of variation		0.52	0.45

Residual hills, Eastern Goldfields of W.A. (C03)			
Lowest ^{10}Be	0.88	180	3.17
Highest ^{10}Be	2.65	595	0.86
Mean (8 samples)		317	2.08
Coeff. of variation		0.50	0.39
Silcrete gibbers, western Lake Eyre basin (F 05)*			
Lowest ^{10}Be gibber	6.63	1985	0.18
Highest ^{10}Be gibber	9.59	4395	0.04
Craggy quartzite slopes, Brachina Gorge, Flinders Ranges (UP.)			
Lowest ^{10}Be	0.24	47	12.4
Highest ^{10}Be	1.17	242	2.3
Mean (9 samples)		94	7.9
Sediment from quartzite slopes, Brachina Gorge, Flinders Ranges (UP.)			
Lowest 10Be sediment	0.36	71	8.2
Highest 10Be sediment	0.72	145	3.9
Mean (4 samples)		102	6.1
*Granite tors, Bega valley (H*00)*			
Lowest ^{10}Be surface	0.15	26	23.0
Highest ^{10}Be surface	0.40	67	8.7
*Sandstone spurs and pagodas, southeast Tablelands (W*05)*			
Lowest ^{10}Be surface	0.11	22	26.8
Highest ^{10}Be surface	0.31	61	9.5
*Soil-mantled slopes, NSW (Bega Valley H*00; Blue Mts W*00)*			
Bega Valley ^{10}Be min (H=0.0)	0.06	10	68.0
Bega Valley ^{10}Be max (H=0.9)	0.51	87	9.3
Blue Mts ^{10}Be min (H=40)	0.10	21	28.0
Blue Mts ^{10}Be max (H=60)	0.17	39	15.0

Notes and references for Table 1. *Exposure age assuming no erosion (minimum exposure age). **Erosion rate assuming uniform long-term erosion (maximum erosion rate). BC02 – Bierman & Caffee (2002); C03 – Chappell (2003); F*05 – Fujioka *et al*. (2005); UP – Chappell, unpublished data; H*00 – Heimsath et al. (2000); W*00 – Wilkinson *et al*. (2005).

Overall, the data indicate that erosion rate tends to increase with rainfall and is higher in steep terrain than on low-relief surfaces. However, the results confirm that, in contrast to tectonically active areas such as New Zealand where erosion rates determined directly from catchment sediment yields range beyond 10,000 m Ma^{-1} (Griffiths 1981; Hovius *et al*. 1997), erosion in Australia is very slow, even in the relatively humid eastern highlands.

SOIL PRODUCTION RATES

The production of soil through rock weathering is one of the most fundamental landscape processes and is of primary significance for soil conservation, but generally is so slow as not to be measureable by direct observation. TCNs offer a basis for determining long-term rates of soil production.

Using Equation 3, the rate of surface lowering (erosion) of a soil-mantled surface soil can be determined from TCN concentrations measured in the rock or undisturbed saprolite at soil base. The result rests on the assumption that the depth of soil cover at the site has remained constant while the underlying surface has been lowered by several metres, which in turn assumes that soil production from the weathering rock and soil loss by creep and other transport processes are equal and remain constant, a condition referred to as steady-state.

Supported by field observations of soil depth on forested, convex spurs in the upper Bega Valley, NSW, which matched theoretical predictions of steady-state soil depth as a function of slope curvature, Heimsath *et al* (2000) assumed that steady-state conditions exist in their study area, and used TCN measurements from saprolite at soil base to determine rates of surface lowering. At the sites in moderately steep, forested granitic slopes in the upper Bega Valley, NSW, Heimsath *et al*. (2000) found that

$$\varepsilon(H) = 53 \exp(-0.02H) \qquad (5)$$

where $\varepsilon(H)$ is the rate of lowering under soil of thickness H, at a given site. Heimsath *et al*. (2000) equated soil production with surface lowering, and proposed that Equation 5 describes the rate of soil production as a function of soil thickness. Chappell (2003) showed that data from sites of lower relief ("downland") in the Bega Valley follow the same trend, although the rate for any given soil thickness is somewhat lower, and Heimsath *et al*. (1999) reported very similar results from soil-mantled greywacke hillsides in California, using the same TCN methods. It should be noted that these studies equate the rate of soil production with the rate of surface lowering; strictly, this is an upper limit, as net soil production rate will generally be less than the surface lowering rate, which is the sum of soil production and mineral dissolution (Stonestrom *et al*. 1998).

The rates of soil production and the negative dependence on soil depth, as reported by Heimsath *et al*. (1999; 2000) and represented by Equation 5, have become an invaluable benchmark for comparative studies. From similar TCN-based methods at soil-mantled sandstone sites in the Blue Mountains, NSW, Wilkinson *et al*. (2005) reported soil production rates from 15 to 28 m.Ma^{-1}, squarely within the range for granitic sites in the Bega Valley (c.f. Table 1). However, from the standpoint of understanding processes of soil production, it is important to note that whereas Heimsath *et al*. (2000) inferred that maximum soil production occurs where the soil is thinnest (as Equation 5 implies), Wilkinson *et al*. (2005) concluded that the maximum rate occurs under a shallow but finite soil cover (~0.1 m) and that the negative-exponential relationship shown by Equation 5 applies only when soil cover is thicker than this. Despite these differences of interpretation, it is clear that TCNs offer a powerful method for assessing the rate of soil production.

CATCHMENT ESTIMATES OF EROSION USING TCNs

Human-induced erosion and soil-loss are familiar problems but their real characteristics often are not accurately known, because local data may be insufficient to evaluate the rates involved, and prior baseline data all too often are lacking. TCNs offer a means for assessing long-term erosion on a catchment scale.

(i) Small catchments

TCN production and concentration decrease rapidly with depth below the ground surface (indicated by the exponential term in H, Equation 2). Hence, where a soil-mantled surface is subject to metre-scale

erosion events such as shallow landslips, scour and tree-throw, the TCN concentration will vary from point to point even though the average long-term erosion rate may be constant.

The problem can be even more acute on rocky slopes, where erosion occurs through thick-slab exfoliation and/or break-up of coarsely jointed rock: the TCN content varies from point to point, depending on the timing of prior rock break-up events. This situation is illustrated by data from steep, coarsely-jointed quartzite slopes in the Flinders Ranges, summarised in Table 1, which show that a mean erosion rate can only be evaluated by making measurements from many sites. In these circumstances, it becomes attractive to determine the mean rate determined from TCNs in sediment derived from the landform. However, the accuracy of the result depends on the travel history of the sediment as it travels from its source to its collecting point. Ideally, the travel time should be short relative to the time needed for a few tens of centimetres of erosion – a condition most likely to be met in weathering-limited, bare rocky catchments.

That sediment-based measurements lead to reasonable estimates of erosion rate, at least at the local scale, is supported by studies of small soil-mantled catchments, where the mean erosion rates calculated from TCNs measured in quartz sand from local streams were similar to weighted averages of *in situ* rates measured from soil pits dotted around the catchments (Heimsath *et al*. 1999; 2000). For coarse, rocky landscapes, the question has been tested in an ongoing study in Brachina Gorge in the Flinders Ranges of South Australia. Steep slopes comprised of steep, coarsely jointed quartzite were sampled, where slope retreat is dominated by failure of joint-controlled blocks, 0.4–1.1 m in size. The samples yielded apparent erosion rates from 2.3 to 12.4 $m.Ma^{-1}$, with a mean of 7.9 $m.Ma^{-1}$. Sediment samples collected from a talus slope and from stream channels draining the quartzite show significantly less variation, ranging from 3.9 to 8.2 $m.Ma^{-1}$, with a mean of 6.1 $m.Ma^{-1}$. Although somewhat lower than the mean for the slope samples, the difference is not statistically significant. Overall, these studies indicate that catchment-average rates can be derived from sediment, even though irregular erosion causes substantial point-to-point variation of TCN concentration in the source areas.

(ii) Large catchments

The feasibility of evaluating long-term erosion rates on a large scale was tested in a recent pilot study from the Yangtse River - one of the world's largest river catchments. Rising in high mountains of northeast Tibet and western Sichuan, the Yangtse River passes through the lowlands of eastern China and delivers a large quantity of sediment to the East China Sea. Human land-clearing and agriculture increased enormously in the Yangtse basin during the last few thousand years and, in recent historical times, sediment inputs to the Yangtse almost certainly have increased as a result of forest clearing and intensified human use of hill country. In order to husband resources, it seems important to understand the magnitude of human impact, but this will remain uncertain until there are long-term baseline data with which estimates of present-day erosion rates, based on river-gauge data and field plots, can be compared.

Using measurements of ^{10}Be (the TCN of choice) from quartz grains in sediments collected throughout the Yangtse River system, and from hillslopes and small catchments in selected headwater regions, Chappell *et al*. (2006) evaluated long-term regional erosion rates for parts of the high northeast Tibet plateau, the high western mountain sources, and selected catchments in eastern China. Although this was a pilot study based on only 23 sites, long-term estimates of regional erosion for the high mountain catchments proved to be similar to rates based on sediment gauging (ranging to over 700 m Ma^{-1}), while measurements from upper Yangtse River tributaries on the high plateau gave rates of 20–30 m Ma^{-1}, which are substantially less than reported in Chinese studies of present-day erosion.

Collectively, the results indicate that TCN measurements of samples from landscape surfaces, both soil-mantled and rocky, together with TCN measurements of sediments from streams of different orders, will yield reliable estimates of erosion rates, at scales from the local hillside up to the larger catchment.

REFERENCES

ANAND R. & PAINE M. 2002. Regolith geology of the Yilgarn Craton, Western Australia: implications for exploration. *Australian Journal of Earth Sciences* **49**: 3-162.

BARROWS T.T., STONE J.O., FIFIELD L.K. & CRESSWELL R.G. 2001. Late Pleistocene glaciation of the Kosciuszko Massif, Snowy Mountains, Australia. *Quaternary Research* **55**: 179-189.

BARROWS T.T., STONE J.O., FIFIELD L.K. & CRESSWELL R.G. 2002. The timing of the Last Glacial Maximum in Australia. *Quaternary Science Reviews* **21**: 159-173.

BIERMAN P.R. 1994. Using in-situ cosmogenic isotopes to estimate rates of landscape evolution: a review from the geomorphic perspective. *Journal Geophysical Research* **99**: 13885-13896.

BIERMAN P.R. & CAFFEE M. 2002. Cosmogenic exposure and erosion history of Australian bedrock landforms. *Geological Society of America Bulletin* **114**: 787-803.

BIERMAN P.R., CAFFEE M., DAVIS P.T., MARSELLA K., PAVICH M., COLGAN P. & MICKLESON D. 2002. Rates and timing of earth surface processes from in situ-produced cosmogenic Be-10. In E.S.Grew (ed.), *Beryllium: Mineraology, Petrology and Chemistry. Reviews in Mineralogy & Geochemistry 50*: 147-206. Mineralogical Society of America, Washington DC.

CERLING T.E. & CRAIG H. 1994. Geomorphology and in-situ cosmogenic isotopes, *Annual Reviews Earth Planetary Science* **22**: 273-317.

CHAPPELL J. 2003. New determinations of the long-term production and migration of soil, our largest mineral deposit. In I.C.Roach (Ed.) *Advances in Regolith: Proceedings of the CRC LEME Regional Regolith Symposia*. CRC LEME, Perth: pp.66-69.

CHAPPELL J., ZHENG H. & FIFIELD K. 2006. Yangtse River sediments and erosion rates from source to sink traced with cosmogenic ^{10}Be: Sediments from major sources. *Palaeogeography, Palaeoclimatology, Palaeoecology* (in press).

FABEL D. (this volume) A brief introduction to in-situ produced terrestrial cosmogenic nuclide methods

FIFIELD L.K. 1999. Accelerator mass spectrometry and its applications. *Reports on Progress in Physics* **62**: 1223-1274.

FUJIOKA T., CHAPPELL J., HONDA M., YATSEVITCH I., FIFIELD K. & FABEL D. 2005. Global cooling initiated stony deserts in central Australia 2–4 m.y. ago, dated by cosmogenic ^{21}Ne-^{10}Be. *Geology* **33**: 993-996.

GRANGER D.E. & MUZIKAR P.F. 2001. Dating sediment burial with in situ-produced cosmogenic nuclides: theory, techniques and limitations. *Earth Planetary Science Letters* **188**: 269-281.

GRIFFITHS G.A. 1981. Some suspended sediment yields from South Island catchments, New Zealand. *Water Resources Bulletin* **17**: 662-671.

HOVIUS N., STARK C.P. & ALLEN P.A. 1997. Sediment flux from a mountain belt derived from landslide mapping. *Geology* **25**: 231-234.

HEIMSATH A.M., DIETRICH W.E., NISHIIZUMI K. & FINKEL R.C. 1999. Cosmogenic nuclides, topography, and the spatial variation of soil depth. *Geomorphology* **27**: 151-172.

HEIMSATH A.M., CHAPPELL J., DIETRICH W.E., NISHIIZUMI K. & FINKEL R.C. 2000. Soil production on a retreating escarpment in southeastern Australia. *Geology* **28**: 787-790.

HEIMSATH A.M., CHAPPELL J., DIETRICH W.E., NISHIIZUMI K. & FINKEL R.C. 2001. Late Quaternary erosion in southeastern Australia: a field example using cosmogenic nuclides. *Quaternary International* **83-85**: 169-185.

HEIMSATH A.M., CHAPPELL J., SPOONER N.A. & QUESTIAUX D.G. 2002. Creeping soil. *Geology* **30**: 111-114.

KIERNAN K., FIFIELD L.K. & CHAPPELL J. 2004. Cosmogenic nuclide ages for Last Glacial Maximum moraine at Schnells Ridge, southwest Tasmania. *Quaternary Research* **61**: 335-338.

LAL D. 1991. Cosmic ray labeling of erosion surfaces: In situ nuclide production rates and erosion models. *Earth & Planetary Science Letters* **104**: 427-439.

PILLANS B. 2005. Geochronology of the Australian regolith. *In*: R.R. Anand and P. de Broekert (Eds.), *Regolith-Landscape Evolution Across Australia.* CRC LEME, Perth: pp. 41-61.

STONE J.O. 2000. Air pressure and cosmogenic isotope production. *Journal of Geophysical Research,* **105(B10)**: 23753-23759.

STONESTROM D.A., WHITE A.F. & AKSTIN K.C. 1998. Determining rates of chemical weathering in soils - solute transport versus profile evolution. *Journal of Hydrology* **209**: 331-345.

TUNIZ C., BIRD J.R., FINK D. & HERZOG G.F. 1998. *Accelerator Mass Spectrometry*. London: CRC Press, 371 pp.

WILKINSON M.T., CHAPPELL J., HUMPHRIES G.S., FIFIELD K., SMITH B. & HESSE P. 2005. Soil production in heath and forest, Blue Mountains, Australia: influence of lithology and palaeoclimate. *Earth Surface Processes and Landforms* **30**: 923-934.

U-SERIES ANALYSIS OF WEATHERING MINERALS BY LA-MC-ICP-MS: A NEW TOOL FOR REGOLITH GEOCHRONOLOGY

Juan Pablo Bernal[1,2,3], Richard A. Eggleton[2] and Malcolm T. McCulloch[1]

1) *Research School of Earth Sciences, The Australian National University, Canberra, ACT 0200, Australia*

2) *CRC LEME, Department of Earth & Marine Sciences, The Australian National University, Canberra, ACT 0200, Australia*

3) *Present address: Instituto de Geologica, UNAM, Ciudad Universitaria, Coyoacan 04510, Ciudad de Mexico, Mexico*

INTRODUCTION

The establishment of a geochronological framework for weathering processes is essential for the understanding of the evolution of the regolith and its dynamics. This is particularly relevant in the context of the Australian continent, since the vast majority of it is covered by one or more forms of regolith, such as saprolite, duricrusts and/or aeolian deposits. However, despite the geological relevance, there are few robust answers regarding the timing and rates of weathering.

In recent years, the development of highly sensitive and precise mass spectrometers, combined with the use of microsampling techniques has allowed for elemental and isotopic analyses within a textural context (Müller 2003), making the search for geochronological records of weathering processes a feasible task. A combined approach of this type has already made a significant impact to the knowledge of the timing of weathering processes, particularly through application of $^{40}Ar/^{39}Ar$ geochronology to supergene K-bearing Mn-oxides and sulfates (Vasconcelos *et al*. 1994; Dammer 1995; Dammer *et al*. 1996; Ruffet *et al*. 1996; Henocque *et al*. 1998; Dammer *et al*. 1999; Vasconcelos 1999; Feng & Vasconcelos 2001; Li & Vasconcelos 2002), and more recently through U-series dating of pedogenic opal and carbonates (Ludwig & Paces, 2002; Sharp *et al*. 2003).

Despite recent advances in weathering geochronology using radiogenic isotopic systems (such as K-Ar, $^{40}Ar/^{39}Ar$), and mounting evidence for recent and continuous weathering (Taylor & Shirtliff 2003), there are few results constraining weathering processes during the Late Quaternary (<500 ka) in Australia (Dammer *et al*. 1999; Feng & Vasconcelos 2001). This represents a significant gap in our current knowledge and understanding of recent weathering processes; particularly for this period, where the record of climatic variation is more extensive and better preserved than any other (beyond the modern instrumental record), and for which the potential to assess the role of global climate on weathering processes is greater than earlier periods.

In the light of these considerations, this study presents a different approach from previous studies. Here authigenic minerals that incorporate U at their time of formation, in particular goethite (α-FeOOH) and hematite (α-Fe_2O_3), are assessed as geochronological recorders of weathering processes. This required the development of a new methodology for the *in situ* measurement of ^{238}U-decay series by laser ablation-multicollector-inductively coupled plasma-mass-spectrometry (LA-MC-ICP-MS), which is then applied to measure U-series disequilibria in iron oxy/hydroxides formed during weathering of a U-rich chlorite-muscovite-schist from the Ranger U-deposit in the Northern Territory of Australia.

SETTING AND SAMPLE PREPARATION

Fresh, partially weathered and intensely weathered rocks were collected from weathering profiles exposed by mining activities at Ranger Uranium Mine (R.U.M.), Northern Territory, Australia.

Additionally, approximately 150 ferruginous pisoliths from the top of the weathering profiles were collected (Figure 1).

Fresh rock and weathered samples were thin-sectioned (50 μm-thick), and the microcrystalline iron oxy/hydroxides accumulations found between veins and cracks (Figure 2 a,b) analysed by LA-MC-ICP-MS. The surface was cleaned with methanol prior to analysis, in order to remove any dust deposited on it. Only punctual analyses (laser-drilling) were performed on these samples

From the approximately 150 pisoliths and nodules collected, preference was given to those with spherical shape, without obvious signs of alteration, such as cracks or concretions with other pisoliths.

Two types of analysis were carried out: transects across the pisolith circumference (including rind and core), and along the circumference of cutans. Prior to analysis by LA-MC-ICP-MS, microanalytical sampling sites (accumulations of microcrystalline goethite and hematite) were identified and located in thin-sectioned specimens by visual inspection using a petrographic microscope.

ANALYTICAL

A method to analyse ^{238}U-^{234}U-^{230}Th using laser ablation-multi collector-inductively coupled plasma-mass spectrometry (LA-MC-ICP-MS) has been developed using an Ar-F excimer laser (193 nm) coupled with a Finnigan Neptune MC-ICP-MS (details of this system can be found elsewhere (Eggins *et al*. 1998; Sinclair *et al*. 1998)). Briefly, this method allows for *in situ* measurement of uranium and thorium isotopes with a spatial resolution of better than 90 μm. Careful identification of instrumental parameters and matrix effects affecting U-Th measurement by LA-MC-ICP-MS were determined by constantly monitoring and analysing matrix-matched solid standards with known isotopic composition and spatial distribution (Bernal 2003). The method allows the measurement of ^{234}U/^{238}U and ^{230}Th/^{238}U activity[1] ratios with a repeatability of ± 1.6‰ and ± 3‰, respectively, and a precision of ± 4‰, and ± 6‰, respectively, for a specimen containing ~ 300 ppm of U, equivalent to an uncertainty of ± 1.8 ka for a 100 ka old sample, or ± 6.5 ka for a 300 ka old sample producing a stable 0.5 V $^{238}U^{+}$ ion beam (Bernal *et al.* 2005).

Samples and standards were analysed using a 93 μm laser-beam diameter with a sampling rate of 8 Hz. Data were collected in batches of 5-8 scans or rasters, or 10-15 drill-holes. Each batch was bracketed by analysis of the reference materials to monitor for changes in U/Th fractionation, detector drift and SEM/FAR yield measurement. ^{234}U/^{238}U, ^{238}U/^{238}U, ^{230}Th/^{238}U, and ^{238}U/^{232}Th isotope ratios were measured, corrected for mass bias and converted to activities by multiplying by the corresponding decay constants. Note that, hereafter, all ratios presented are activity ratios (AR) unless otherwise stated.

AGE CALCULATIONS AND ERRORS

Ages were derived from the measured ^{234}U/^{238}U and ^{230}Th/^{238}U by solving:

$$\frac{^{230}\mathrm{Th}}{^{238}\mathrm{U}} = 1 - e^{-\lambda_{230}t} + \frac{\lambda_{230}}{\lambda_{230} - \lambda_{234}} \times \left[\left(\frac{^{234}\mathrm{U}}{^{238}\mathrm{U}} \right) - 1 \right] \times \left(1 - e^{-(\lambda_{230} - \lambda_{234})t} \right)$$

where λ refers to the corresponding decay constant for each isotope, and t is the age of the specimen. Ages were estimated using ISOPLOT v.2.49t. (Ludwig 2001). A ^{232}Th/^{238}U > 0.02 (or ^{238}U/^{232}Th <50) was used as an indication of significant contributions from allogenic material to measured AR, in which case the U and Th isotopic composition of the authigenic phase was calculated using Osmond-type isochrons (Osmond et al., 1970) but applying the maximum likelihood approach (Ludwig & Titterington 1994) using ISOPLOT 2.41t (Ludwig 2001).

[1] Activity = No of Atoms x decay constant

RESULTS

$^{234}U/^{238}U$ in microcrystalline iron oxy/hydroxides

Typical $^{234}U/^{238}U$ measured in the microcrystalline goethite and hematite are presented in Figure 3 as a series of "box plots". The most important feature is the relatively small fractionation between ^{234}U and ^{238}U observed for most samples, as attested by an average $^{234}U/^{238}U$ ratio only slightly higher than 1 (average for all profiles 1.0203 ± 0.011 n=158).

The activity ratios in Figure 3 are different to those previously reported (Lowson *et al*. 1986; von Gunten *et al*. 1999) from the top ten metres of the lateritic sections at the Ranger's orebodies #1 and #3. For the latter, $^{234}U/^{238}U$ ratios between 0.7 and 1.16 for the <106 μm fraction have been reported (von Gunten *et al*. 1999), whereas for orebody #1, $^{234}U/^{238}U$ between 0.67 to 1.14 and 0.96-1.21 for amorphous and crystalline iron, respectively, have been reported (Lowson *et al*. 1986). While the ARs presented here fall within the previously reported limits, the variability and apparent trends previously reported are not observed.

The ARs shown in Figure 3 are consistent with U co-precipitation with, or adsorption onto iron oxy/hydroxides from groundwater with dissolved uraninite. Experiments on partial dissolution of uraninite under controlled laboratory conditions have shown only a slight but measurable ^{234}U enrichment in the resulting solution, with $^{234}U/^{238}U$ between 1 and 1.05 (Eyal & Fleischer 1985). Similar activity ratios have been measured in groundwater free from colloidal matter in the Koongarra and Nabarlek U-deposits (Short *et al*. 1988), and other U- and Th- rich orebodies (Bonotto 1998).

Two groundwater samples were collected from the vicinity of the orebody, and the U and Th isotopic composition measured by isotope-dilution MC-ICP-MS following the procedures described elsewhere (de Caritat *et al*. 2005; Mortimer *et al*. 2002). The results of these analyses are presented in Table 1 and indicate that groundwater carrying dissolved uraninite, and percolating through the bedrock (and possibly forming the iron oxy/hydroxides), has an isotopic signature that is similar to that of the authigenic minerals.

Table 1 U and Th concentrations and isotopic composition for groundwater samples collected in the vicinity of Ranger #3 orebody. Coordinates are on Australian GeoDatum 1966. Distance from profile in metres and approximate direction between brackets.

Sample	Bore-hole Location	Depth (m)	Distance from profile NW (m)	U_{TOTAL} ($\mu g \cdot g^{-1}$)	^{232}Th ($ng \cdot g^{-1}$)	$^{234}U/^{238}U$	$^{230}Th/^{238}U$
OB54	274079E 8597466N	90.5	550 (NE)	6.43 ± 0.008	0.06± 0.003	1.051± 0.006	0.012± 0.001
OB56	273450E 8598080N	92	710 (SW)	3.52 ± 0.003	0.05 ± 0.01	0.992± 0.003	0.0093 ±0.001

The $^{230}Th/^{238}U$ and apparent ^{230}Th-age of the microcrystalline iron oxy/hydroxides

Figure 4 shows the $^{230}Th/^{238}U$ for the different samples and profiles plotted against their corresponding depth in the profile. The $^{230}Th/^{238}U$ from samples collected from the top of the profiles have larger uncertainties than those below them, and in some cases populations of iron oxy/hydroxides with significantly different $^{230}Th/^{238}U$ can be identified. Clearly, the iron oxy/hydroxides from the top of the profiles have been subjected to weathering and reprecipitation processes that are not recorded in samples that are deeper in the profiles.

The activity ratios for samples from profile G are similar to each other within 2-σ uncertainty. However, when plotted against their corresponding depth in the profile (Figure 4) a trend towards lower $^{230}Th/^{238}U$ ratios from bottom to top is noticeable. Conversely, the $^{230}Th/^{238}U$ for samples from

profiles BS and NW show different trends to that of profile G: for profile NW $^{230}Th/^{238}U$ decrease with depth, while no trend is evident for the AR for profile BS (apart from the large scatter at the top of the profile).

The microcrystalline iron oxy/hydroxides at the top of the profiles appear to have been subjected to a number of relatively complex processes. In contrast, the $^{230}Th/^{238}U$ from the lower parts of profiles NW and BS suggest that these specimens probably reflect a single, non-altered, generation of authigenic iron oxy/hydroxides minerals, from which it may be more likely to obtain geochronological information.

Consideration of the AR in a $^{234}U/^{238}U$-$^{230}Th/^{238}U$ evolution diagram (Figure 5) shows that the samples fall along an evolution line for $[^{234}U/^{238}U]_0 = 1.05 \pm 0.05$, however, there is no obvious relationship between $^{234}U/^{238}U$ isotopic evolution and stratigraphic position of samples within the profiles. Only one sample, 1AB5 (see Appendix), has an average $^{234}U/^{238}U$ slightly lower (0.992 ± 0.010) than the other samples, possibly due to slight alteration. All samples cluster within a $^{230}Th/^{238}U$ activity ratio between 0.7 and 0.95, and only one, NW14 (see Appendix), has a 2-σ uncertainty that exceeds U-series dating limits (*i.e.* infinite age).

Estimation of apparent ages (see Appendix) shows that most samples cluster within an age-span of 205 ± 30 ka (unweighted average, 203 ± 13 ka, weighted average 2 outliers excluded). In the case of profiles NW and G, the apparent ages for each sample are correlated with their corresponding stratigraphic position within the profile.

For profile NW a ^{230}Th-age of 127.8 +11/-10 ka is estimated for the bottom of the profile and 241 +31/-23 ka for the top (the uppermost sample has not been considered). The ARs measured in the authigenic iron oxy/hydroxides in this profile lie, within 2-σ uncertainty, on an evolution line with a $[^{234}U/^{238}U]_0 = 1.03 \pm 0.02$ (Figure 5). For profile BS, the relationship between the ^{230}Th-age and the stratigraphic position of the sample is weaker than profile NW, with only a marginal increase in the ^{230}Th-age from bottom to the top of the profile. The ARs for this profile also fall over an evolution line with $[^{234}U/^{238}U]_0 = 1.03$; however, unlike profile NW, the ARs fail to follow the expected evolution pattern. This difference may be due to open-system behaviour of the iron oxy/hydroxides in the upper sections of the profile, casting doubt on the validity of the assumed closed-system conditions, thus the ^{230}Th-ages. For profile G, in contrast, the trend between ^{230}Th-ages and depth is inverted. Although the ARs fall within the $[^{234}U/^{238}U]_0 = 1.05 \pm 0.05$ evolution line estimated for all the samples, this is mainly due to the large uncertainties in the estimated ARs. The observed trend in ages and $^{230}Th/^{238}U$ (Figure 4) suggest that the iron oxy/hydroxides in this profile have been subjected to post-depositional incorporation of U and, as such, might not have been closed-systems.

None of the analysed samples produced an age younger than 120 ka. This should not necessarily be considered as definitive evidence indicating a pause in the evolution of the weathering profile, as not all microcrystalline components were measured. In particular those smaller than the optimum spatial resolution (90 μm) of the laser ablation sampling used.

Contrary to other systems usually dated using U-series disequilibria, such as corals, speleothems or opals, there is no petrographic evidence supporting closed-system behaviour for the microcrystalline iron oxy/hydroxides. Although the U-series compositions for samples from profiles NW and BS have apparently evolved within the weathering profile, it is not clear if the authigenic goethite and hematite have been subjected to several cycles of congruent dissolution and precipitation. It is very likely that such processes are more important in the upper sections of the profiles, where iron oxy/hydroxides are filling cracks and voids, and are not as intimately associated with the primary minerals as in the samples from the lower sections of the profiles

The ^{238}U-^{234}U-^{230}Th composition of pisoliths across cores and rinds

Figure 6 shows a typical LA-MC-ICP-MS transect along a pisolith rind and core. In the figure, a scan obtained by LA-ICP-QMS (quadrupole mass spectrometry) is also shown, and attests to the high U and Th concentrations found in these materials. Despite the U concentration in the rind being at least 2× that of the core, there is little evidence to suggest significant post-depositional U migration or diffusion into the core. Such processes would be expected to produce a gradual decrease in U

concentration towards the centre of the specimen (for samples affected by recent U uptake), producing concave-upwards U concentration profiles and a complementary increase of $^{230}Th/^{238}U$ and $^{232}Th/^{238}U$ towards the centre. However, the Th/U ratios observed within the core transects are relatively constant and not consistent with any post-depositional U-uptake (Millard & Hedges 1996; Pike *et al*. 2002).

The distribution of U isotopes within the core is also relatively homogeneous, with only some evident variations due to the ablation of allogenic minerals. A $^{234}U/^{238}U$ weighted average of $^{234}U/^{238}U = 1.022 \pm 0.022$ was obtained for all the cores, similar to the AR of the microcrystalline iron oxy/hydroxides from the profiles below them ($^{234}U/^{238}U = 1.05 \pm 0.05$).

These results, combined with the lack of evidence to support post-depositional migration of U within the core, strongly suggest that the cores have been largely closed-systems for, at least, the period of rind formation.

The ^{238}U-^{234}U-^{230}Th composition along the cutans.

Concentric scans along the cutans made it possible to obtain more precise ARs, and with better spatial control than those measured during the transect analysis (see Figure 2). Figure 7 presents the evolution ^{238}U-^{234}U-^{230}Th evolution diagram with the results from all the analysed pisoliths, including the cores and rinds.

The AR for the cutans and the cores do not follow a single $^{234}U/^{238}U$ evolution line. Furthermore $^{234}U/^{238}U$ and $^{230}Th/^{238}U$ appear to be linearly correlated suggesting that such linear array might be the consequence of mixing of two components with different isotopic composition. Alternatively, the isotopic composition of the rinds might be a reflection of a gradual decrease in $[^{234}U/^{238}]_0$ during the last 300 ka. Both alternatives have been thoroughly discussed elsewhere (Bernal 2003), and have been demonstrated to be geochemically inconsistent. Rather, the isotopic composition of the cutans is consistent with a scheme of pisolith accretion and further leaching of U, with preferential loss of ^{234}U. The geochronological consequences of this are discussed elsewhere (Bernal 2003).

DISCUSSION

The distribution of U and its nuclides within the pisolith cores leaves little doubt that these have acted as essentially closed-systems after deposition of the rinds, as no sign of U migration is evident. The cores have a $^{234}U/^{238}U$ weighted average of 1.022 ± 0.022, however a closer examination of the isotopic composition of U in the cores (open ovals in Figure 8) shows that they do not follow a single $^{234}U/^{238}U$ evolution line, and $^{234}U/^{238}U$ ranges between 0.96 and 1.12.

The range of $^{234}U/^{238}U$ suggest that some core material might have been subjected to early leaching and, arguably, dissolution and re-precipitation of hematite before being sealed from the surrounding saprolite during rind accretion. This is consistent with the very active geochemical environment at the top of the profiles, also attested by the AR measured for the microcrystalline iron oxy/hydroxides in the upper sections of the weathering profiles, where pisoliths and nodules are formed.

The ^{230}Th-ages for the cores (see appendix) range from 166 +5/-4 ka to 314 +57/-35 ka. However, the $^{234}U/^{238}U < 1$ for the sample with the oldest age (P13) strongly suggest that the precursor of this core has been affected by significant U leaching prior to accretion of the rind and, consequently, yields a ^{230}Th-age older than any of the other cores. If this was the case, and P13 is excluded, the age-range for the cores is from 155 +5/-4 ka to 241 +12/11 ka, which is similar to that obtained for the microcrystalline iron oxy/hydroxides from profiles NW (127.8 – 272 ka) and BS (190 – 241 ka). In contrast to the microcrystalline iron oxy/hydroxides, the ^{230}Th-ages of the cores appear to be more robust due to the petrographic and geochemical evidence supporting closed-system behaviour. Considering that, prior to accretion, the core-precursors were embedded in the saprolite, the agreement in ^{230}Th-ages between the two types of iron oxy/hydroxides (pisolith cores and microcrystalline) strongly suggest that the ^{230}Th-ages estimated for the saprolite samples (profiles NW and BS) can also be largely regarded as closed-system ages.

The results presented here appear to be at odds with several other reports on the age of weathering processes in Northern Australia. K-Ar and $^{40}Ar/^{39}Ar$ ages of supergene K-Mn-oxides from Groote

Eylandt (approximately 350 km east of Ranger) indicate major weathering events during the late Eocene, 43.7 Ma, Oligocene, 30 Ma, and Miocene, 6-18 Ma (Dammer *et al*. 1996). This evidence is also supported by similar K-Ar and $^{40}Ar/^{39}Ar$ of supergene Mn-oxides from north-western Australia, (Dammer *et al*. 1999), South Australia (Bird *et al*. 1990), central Queensland (Li & Vasconcelos 2002), and elsewhere (Vasconcelos *et al*. 1994; Ruffet *et al*. 1996; Henocque *et al*. 1998).

Clearly these events lie far beyond the range of U-series dating. However, they indicate that the general conditions conducive to weathering have existed for several millions of years. Feng & Vasconcelos (2001), have reported, however, the formation of supergene Mn-oxides during the Quaternary (300-330 ka) along with specimens formed during the late Miocene (6.8 ± 0.8 Ma) in southeast Queensland (Feng & Vasconcelos 2001).

Dammer (1995) has also reported "zero-ages" in locations where Mn-oxides have been formed during the last 50 Ma, but restricted them to coastal areas with high precipitation (Dammer 1995), in agreement with the interpretation of Vasconcelos *et al.* (1994). This indicates that weathering is indeed still active in places where older generations of supergene minerals have been preserved.

The slow rates of formation of supergene Mn-oxides, $0.3 – 6.3 \times 10^{-3}$ mm/ka, (Feng & Vasconcelos, 2001; Henocque *et al*. 1998) suggest that these will form specimens of significant size (~ 1 mm) only after several millions of years of continuous deposition. Consequently, the absence of younger datable Mn-oxides cannot be attributed to the cessation of weathering processes, but rather to the difficulty of accreting "datable" specimens after short periods of time in locations where very slow Mn-deposition rates dominate.

Furthermore, under these conditions, young (Quaternary) Mn-oxides of "datable" size are limited to locations with very high Mn-deposition rates; *i.e.* costal areas with high precipitation with high Mn mobility (Dammer 1995).

The absence of iron oxy/hydroxides specimens older than 300 ka suggests either: 1) oxidising weathering conditions started at ~300 ka or, 2) samples older than 300 ka have not been preserved. Given the results obtained by Dammer (1995), it seems highly unlikely that oxidising weathering, or ferrugnisation, commenced 300 ka ago in Ranger. Rather, the results obtained here suggest that no material older than 300 ka has been preserved. This is supported by thermo-luminescence (TL) dating of alluvial sediments in the Magela Creek catchment, which indicates that a period of significant sediment accumulation was initiated about 300 ka, and suggests that prior to that age erosional episodes in the area were more efficient (Nanson *et al*. 1993). Altogether, it is not possible in the current study to establish the age for the initiation of weathering in Ranger since there has been no preservation of the older generations of iron oxy/hydroxides, a vital factor to accurately establishing the full age range of weathering processes (Taylor & Shirtliff, 2003).

CONCLUSIONS

The results presented here show that the U and Th isotopic composition in authigenic iron oxy/hydroxides are a promising tool as geochronometers for weathering processes. However, the U-Th isotopic evolution of the regolith is complex and requires careful understanding.

The AR measured here suggest that the microcrystalline iron oxy/hydroxides appear to act largely as closed-system. Nevertheless, the geochronological implications of this conclusion need to be regarded with caution. The formation of iron oxy/hydroxides is a continuous process, rather that the result of discrete major weathering events. Furthermore, the ^{230}Th-age of some specimens (*e.g.* the pisolith cores) is not consistent with their stratigraphic position within the weathering profiles. This is a reflection of the continuous and complex evolution of the weathering profiles and, indeed, of weathering processes. Consequently, any further study following the results and interpretations presented here should consider the overall nature of weathering. It is important not to draw geochronological conclusions based on a limited geochronological data-set, without assessing *a priori* the effect and consequences of U and Th mobility in the regolith and authigenic minerals, unless strong and unequivocal geological evidence suggesting a simple weathering scenario is available.

The high affinity of the iron oxy/hydroxides for the uranyl ion, combined with its high mobility in oxidising conditions and lack of mobility of Th provides an efficient fractionation mechanism to "reset" the U-Th geochronometer. However, the small crystal size and pervasive characteristics of the iron oxy/hydroxides require *in situ* analyses. The LA-MC-ICPMS method described here enables the analysis of the iron oxy/hydroxides selectively with minimum contributions from allogenic phases, and within a textural context. Furthermore, sample preparation is also minimised allowing a significant increase in sample throughput.

LA-MC-ICP-MS analysis of pisoliths and iron oxy/hydroxides has the potential to become the "cornerstone" technique to establish a robust geochronological framework for weathering processes. Unfortunately U-leaching has corrupted the U isotopic composition of the pisolith rinds and some cores, making them unusable for geochronological purposes. Nevertheless, the $^{230}Th/^{238}U$ of the cutans strongly suggests that these have been formed continuously during the last 100 ka, supporting a regime of continuous, and not episodic weathering processes in Northern Australia.

ACKNOWLEDGMENTS

The authors would like to thank Energy Resources of Australia Ltd. and Earth-Water-Life Sciences Pty Ltd for support during sample collection at Ranger. Greg Shirtliff is also thanked for continuous support during field work and the course of this research. Support to J.P. Bernal from the ANU, CRC LEME and CONACyT (Mexico) is appreciated.

REFERENCES

BERNAL J.P. 2003. *In situ* measurement of U-series disequilibria in iron oxy/hydroxides and its application to weathering geochronology. Unpublished Ph.D. Thesis, The Australian National University, Canberra.

BERNAL J.P., EGGINS S.M. & MCCULLOCH M.T. 2005. Accurate in situ ^{238}U-^{234}U-^{232}Th-^{230}Th analysis of silicate glasses and iron oxide by laser-ablation MC-ICP-MS. *Journal of Analytical Atomic Spectrometry* **20(11)**: 1240-1249.

BIRD M.I., CHIVAS A.R. & MCDOUGALL, I. 1990. An isotopic study of surficial alunite in Australia; 2, Potassium-argon geochronology. *Chemical Geology; Isotope Geoscience Section* **80(2)**: 133-145.

BONOTTO D.M. 1998. Implications of groundwater weathered profile interactions to the mobilization of radionuclides. *Journal of South American Earth Sciences* **11(4)**: 389-405.

DAMMER D. 1995. Geochronology of chemical weathering processes in the Northern and Western Australian regolith. Unpublished Ph.D. Thesis, The Australian National University, Canberra.

DAMMER D., CHIVAS A.R. & MCDOUGALL I. 1996. Isotopic dating of supergene manganese oxides from the Groote Eylandt deposit, Northern Territory, Australia. *Economic Geology* **91(2)**: 386-401.

DAMMER D., MCDOUGALL I. & CHIVAS, A.R. 1999. Timing of weathering-induced alteration of manganese deposits in Western Australia: Evidence from K/Ar and $^{40}Ar/^{39}Ar$ dating. *Economic Geology* **94(1)**: 87-108.

DE CARITAT P., KIRSTE D., CARR G. & MCCULLOCH M. 2005. Groundwater in the Broken Hill region, Australia: recognising interaction with bedrock and mineralisation using S, Sr and Pb isotopes. *Applied Geochemistry* **20(4)**: 767-787.

EGGINS S.M., KINSLEY L.P.J. & SHELLEY J.M.G. 1998. Deposition and element fractionation processes during atmospheric pressure laser sampling for analysis by ICP-MS. *Applied Surface Science* **129**: 278-286.

EYAL Y. & FLEISCHER R.L. 1985. Preferential leaching and the age of radiation damage from alpha decay in minerals. *Geochimica et Cosmochimica Acta* **49**: 1155-1164.

FENG Y.X. & VASCONCELOS P. 2001. Quaternary continental weathering geochronology by laser-heating $^{40}Ar/^{39}Ar$ analysis of supergene cryptomelane. *Geology* **29(7)**: 635-638.

HENOCQUE O., RUFFET G., COLIN F. & FERAUD G. 1998. $^{40}Ar/^{39}Ar$ dating of west african lateritic cryptomelanes. *Geochimica et Cosmochimica Acta* **62(16)**: 2739-2756.

LI J.W. & VASCONCELOS P. 2002. Cenozoic continental weathering and its implications for the palaeoclimate: evidence from $^{40}Ar/^{39}Ar$ geochronology of supergene K-Mn oxides in Mt Tabor, central Queensland, Australia. *Earth & Planetary Science Letters* **200(1-2)**: 223-239.

LOWSON R.T., SHORT S.A., DAVEY B.G. & GRAY D.J. 1986. $^{234}U/^{238}U$ and $^{230}Th/^{234}U$ activity ratios in mineral phases of a lateritic weathered zone. *Geochimica et Cosmochimica Acta* **50**: 1697-1702.

LUDWIG K.R. 2001. Users manual for Isoplot/Ex. rev. 2.49, *Berkeley Geochronology Center. Special publication No. 1a*, Berkeley, CA.

LUDWIG K.R. & PACES J.B. 2002. Uranium-series dating of pedogenic silica and carbonate, Crater Flat, Nevada. *Geochimica et Cosmochimica Acta* **66(3)**: 487-506.

LUDWIG K.R. & TITTERINGTON D.M. 1994. Calculation of $^{230}Th/U$ isochrons, ages and errors. *Geochimica et Cosmochimica Acta* **58(22)**: 5031-5042.

MILLARD A.R. & HEDGES R.E.M. 1996. A diffusion-adsorption model of uranium uptake by archaeological bone. *Geochimica et Cosmochimica Acta* **60(12)**: 2139-2152.

MORTIMER G.E., MCCULLOCH M.T., KINSLEY L.P.J. & ESAT T.M. 2002. High precision ^{234}U-^{230}Th dating using MC-ICP-MS. *Geochimica et cosmochimica Acta* **66**: A527 (Abstr).

MÜLLER W. 2003. Strengthening the link between geochronology, textures and petrology. *Earth & Planetary Science Letters* **206(3-4)**: 237-251.

NANSON G.C., EAST T.J. & ROBERTS R.G. 1993. Quaternary stratigraphy, geochronology and evolution of the Magela Creek catchment in the monsoon tropics of northern Australia. *Sedimentary Geology* **83**: 277-302.

OSMOND J.K., MAY J.P. & TANNER W.F. 1970. Age of the Cape Kennedy barrier-and lagoon complex. *Journal of Geophysical Research* **75(2)**: 469-479.

PIKE A.W.G., HEDGES R.E.M. & VAN CALSTEREN P. 2002. U-series dating of bone using the diffusion-adsorption model. *Geochimica et Cosmochimica Acta* **66(24)**: 4273-4286.

RUFFET G., INNOCENT C., MICHARD A., BEAUVAIS A., NAHON D. & HAMELIN B. 1996. A geochronological $^{40}Ar/^{39}Ar$ and $^{87}Rb/^{87}Sr$ study of K-Mn oxides from the weathering sequence of azul, Brazil. *Geochimica et Cosmochimica Acta* **60(12)**: 2219-2232.

SHARP W.D., LUDWIG K.R., CHADWICK O.A., AMUNDSON R. & GLASER L.L. 2003. Dating fluvial terraces by $^{230}Th/U$ on pedogenic carbonate, Wind River Basin, Wyoming. *Quaternary Research* **59(2)**: 139-150.

SHORT S.A., LOWSON R.T. & ELLIS, J. 1988. $^{234}U/^{238}U$ and $^{230}Th/^{234}U$ activity ratios in the colloidal phases of aquifers in lateritic weathered zones. *Geochimica et Cosmochimica Acta* **52(11)**: 2555-2563.

SINCLAIR D.J., KINSLEY L.P.J. & MCCULLOCH M.T. 1998. High resolution analysis of trace elements in corals by laser ablation ICPMS. *Geochimica et Cosmochimica Acta* **62(11)**: 1889-1901.

TAYLOR G. & SHIRTLIFF G. 2003. Weathering: cyclical or continuous? An Australian perspective. *Australian Journal of Earth Sciences* **50(1)**: 9-17.

VASCONCELOS P.M. 1999. K-Ar and $^{40}Ar/^{39}Ar$ geochronology of weathering processes. *Annual Reviews of Earth and Planetary Sciences* **27(1)**: 183-229.

VASCONCELOS P.M., RENNE P.R., BRIMHALL G.H. & BECKER T.A. 1994. Direct dating of weathering phenomena by $^{40}Ar/^{39}Ar$ and K-Ar analysis of supergene K-Mn oxides. *Geochimica et Cosmochimica Acta* **58(6)**: 1635-1665.

VON GUNTEN H.R., ROESSLER E., LOWSON R.T., REID R.D. AND SHORT S.A. 1999. Distribution of uranium- and thorium series radionuclides in mineral phases of a weathered lateritic transect of a uranium ore body. *Chemical Geology* **160(3)**: 225-240.

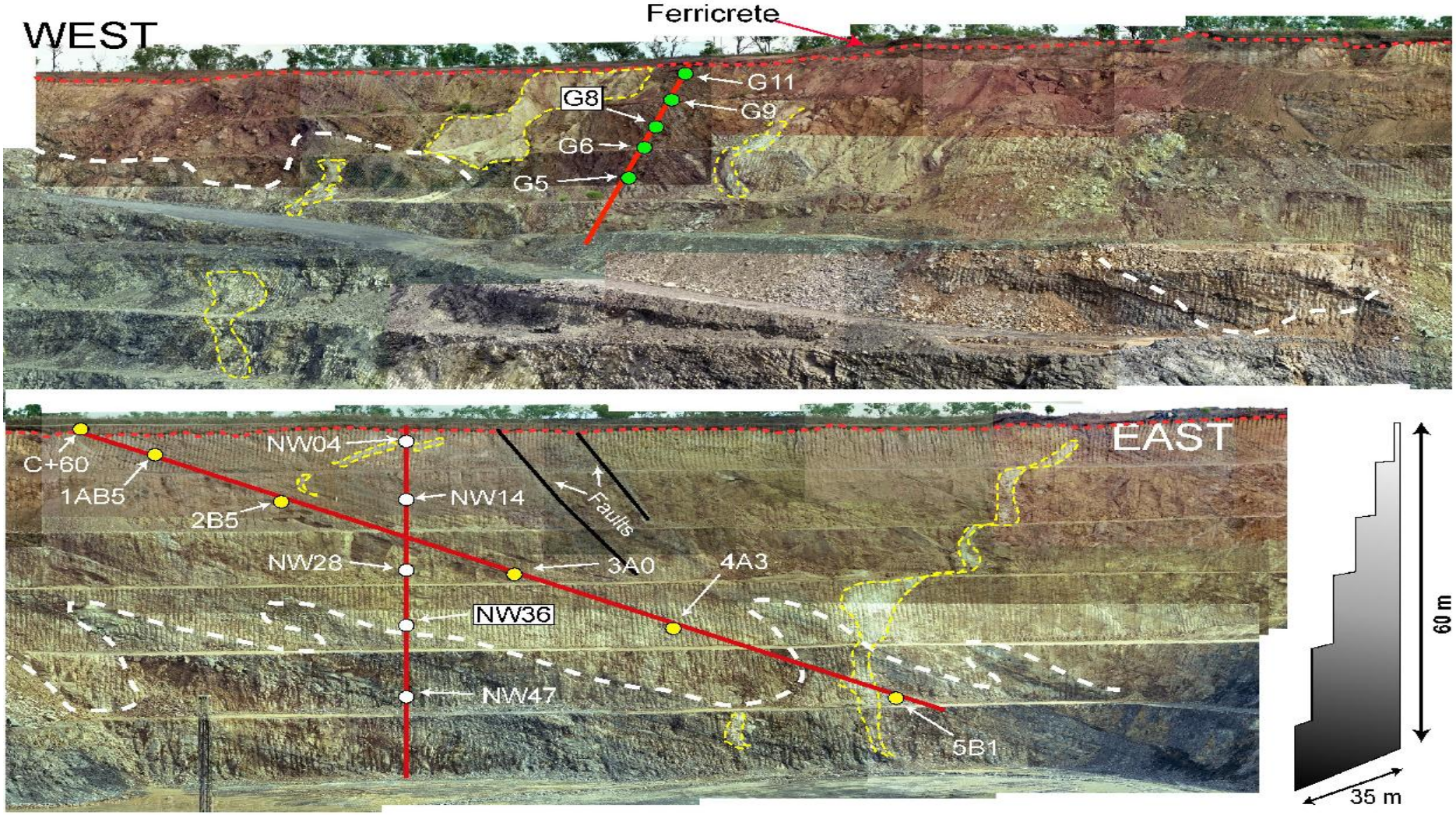

Figure 1. Ranger Uranium Mine, Pit # 3 North Wall, Location of Samples selected of U-series analysis by LA-MC-ICP-MS.

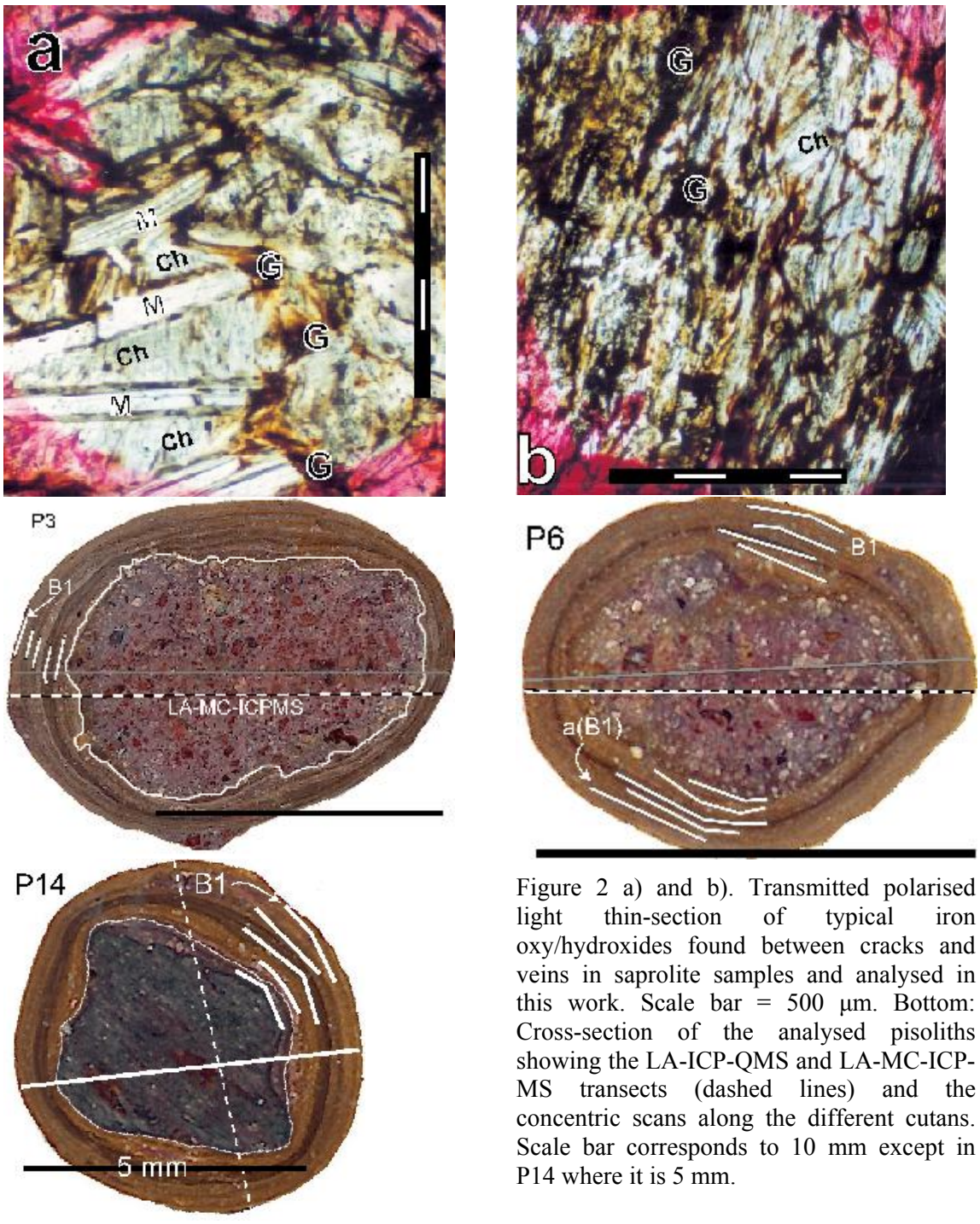

Figure 2 a) and b). Transmitted polarised light thin-section of typical iron oxy/hydroxides found between cracks and veins in saprolite samples and analysed in this work. Scale bar = 500 µm. Bottom: Cross-section of the analysed pisoliths showing the LA-ICP-QMS and LA-MC-ICP-MS transects (dashed lines) and the concentric scans along the different cutans. Scale bar corresponds to 10 mm except in P14 where it is 5 mm.

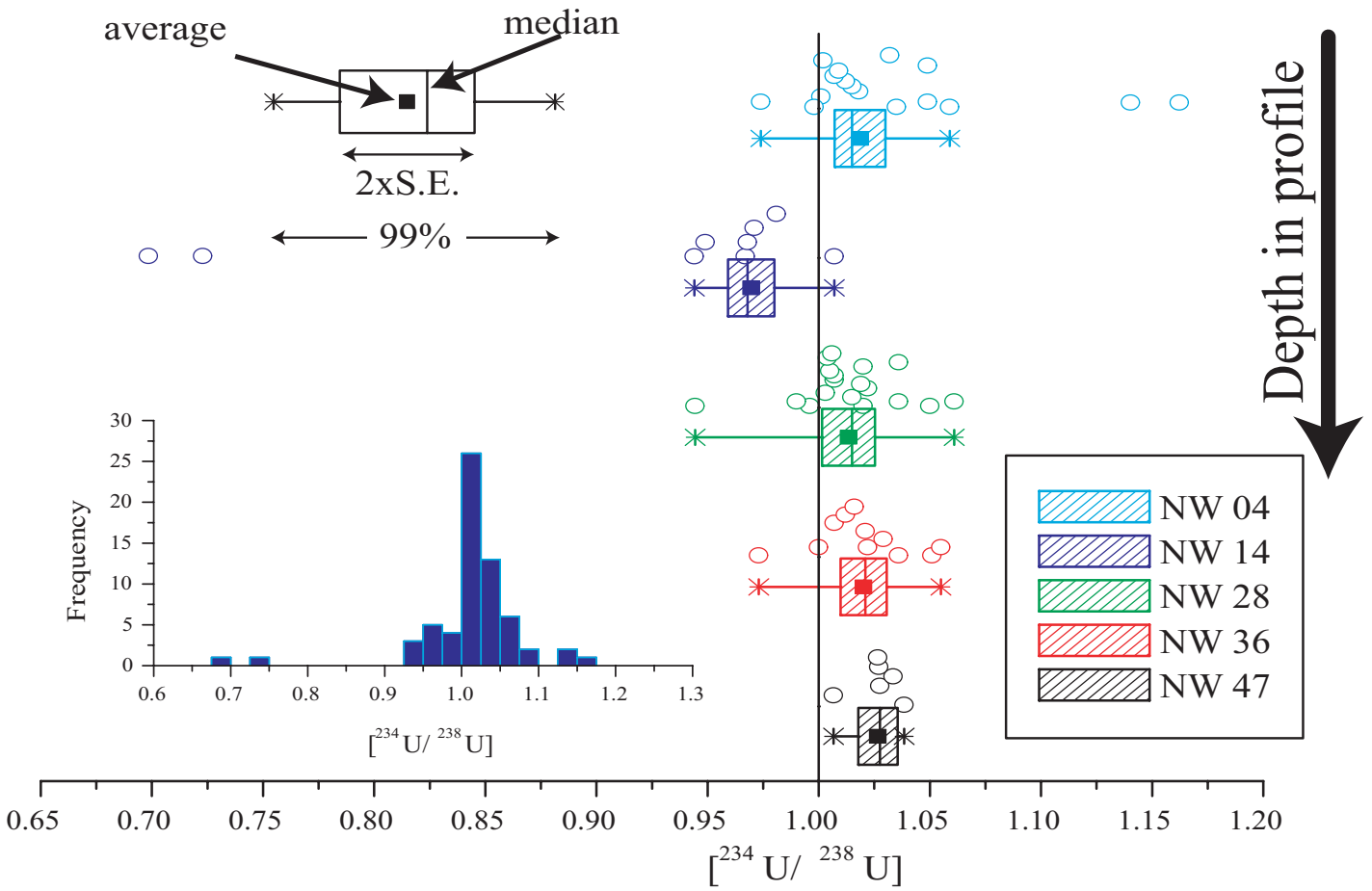

Figure 3. [$^{234}U/^{238}U$] activity ratios for microcrystalline iron oxy/hydroxides from profile NW (~60 m deep – Fig. 1). Each sample is represented in its vertical position in the profile. The uncertainty for each measurement is ± 0.02 (activity), Each box indicates the median and average, the box width represents the 2×standard error uncertainty for each sample. The results for each drill-hole are shown above the box to illustrate the distribution of activity ratios for each sample. Uncertainties for each analyses (not shown) ranged between 2-3%. Inset: histogram comprising all the activity ratios for the profile.

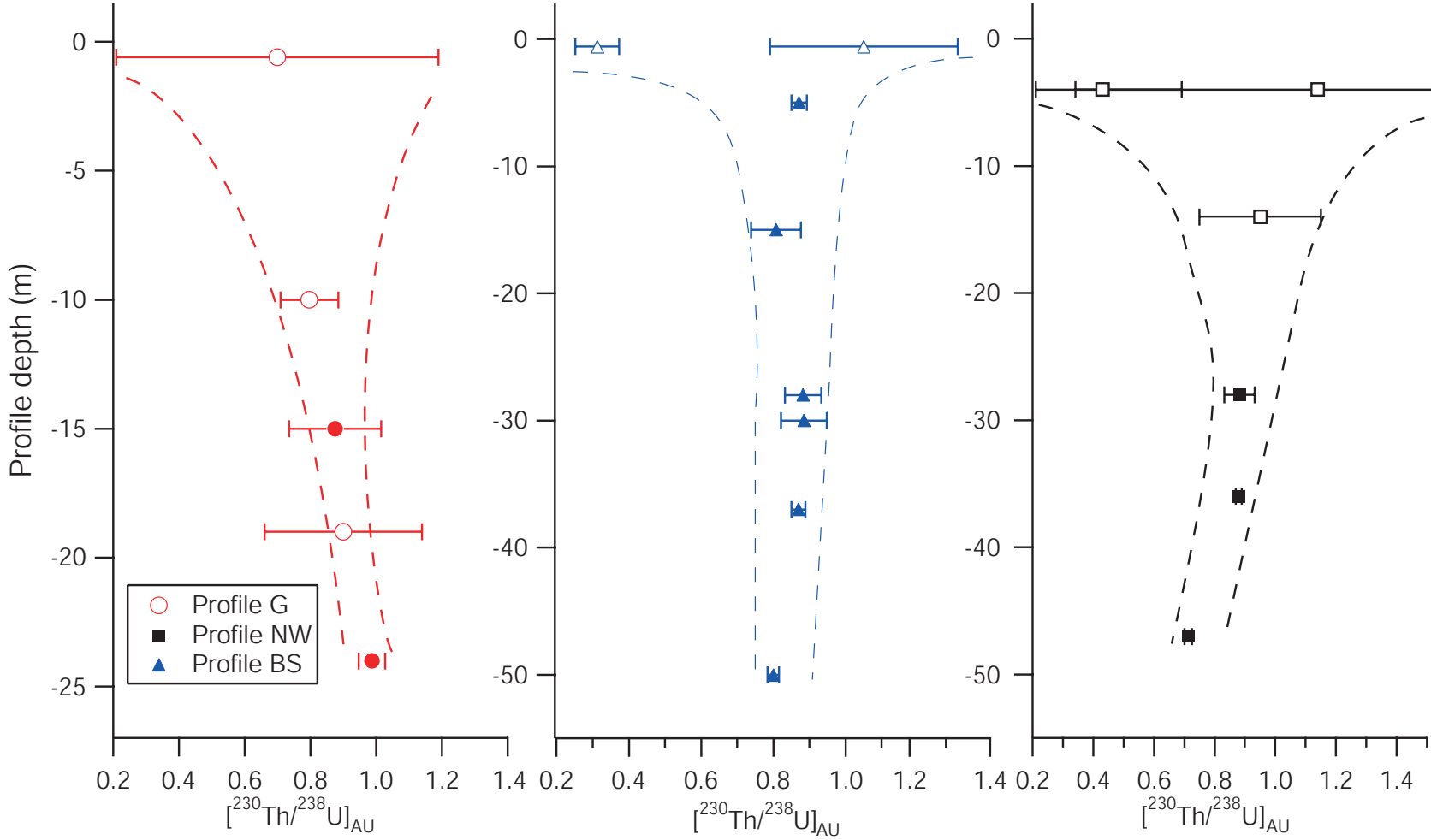

Figure 4. $^{230}Th/^{238}U$ activity ratios for the iron oxy/hydroxides against their corresponding depth in the profile at Ranger (Fig. 1). Open symbols: the activity ratio was corrected for contributions from detrital material significant ($^{238}U/^{232}Th < 50$). Closed symbols: contributions for detrital material were not significant ($^{238}U/^{232}Th > 50$). Error bars are 2σ.

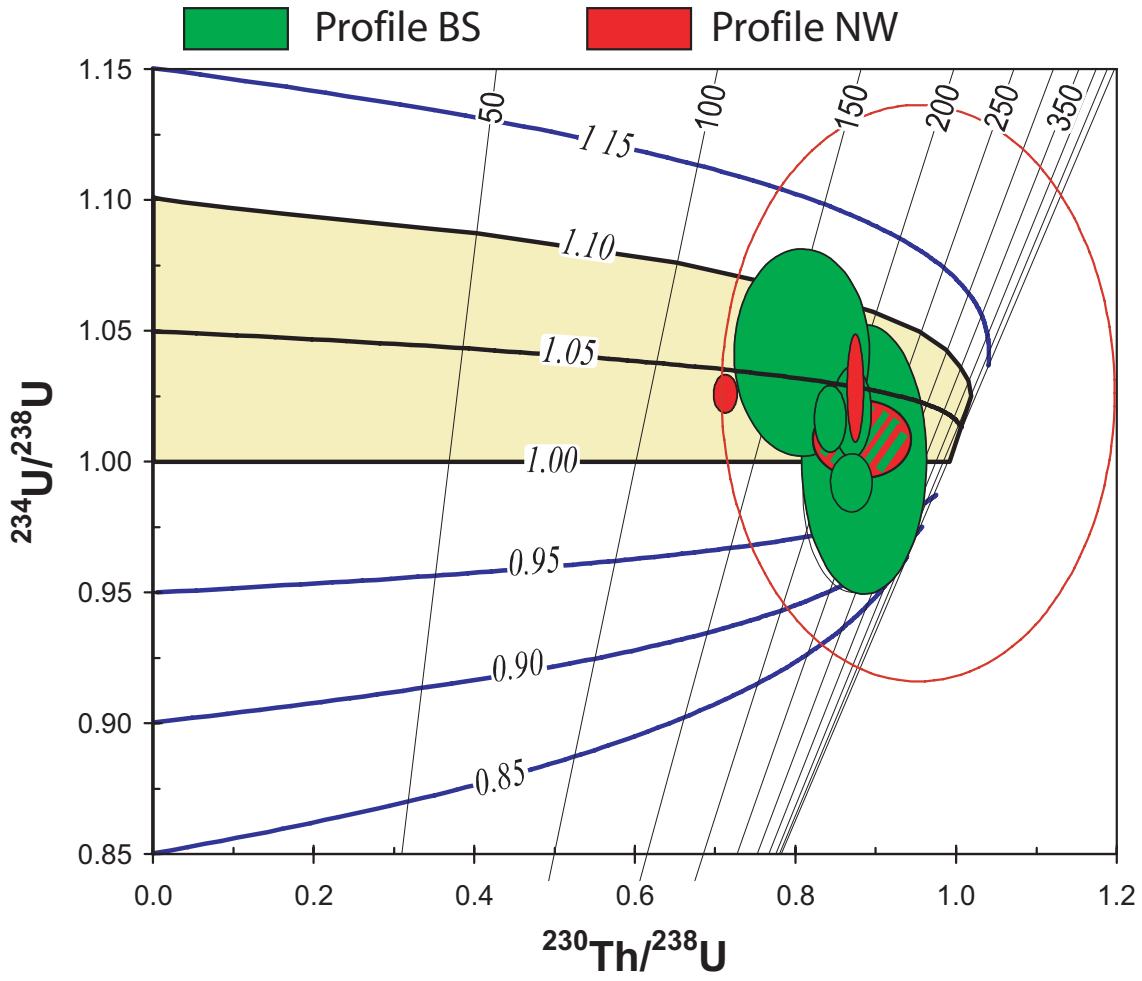

Figure 5. Evolution diagram for samples from profiles BS and NW. Samples from the top of the profiles are not included for clarity. Ovals correspond to 2-σ uncertainties. Hatched oval corresponds to sample NW 28. Red open oval corresponds to sample NW14. Shaded area indicates evolution curve for $[^{234}U/^{238}U]_o$ = 1.05 ± 0.05. Ages are in ka.

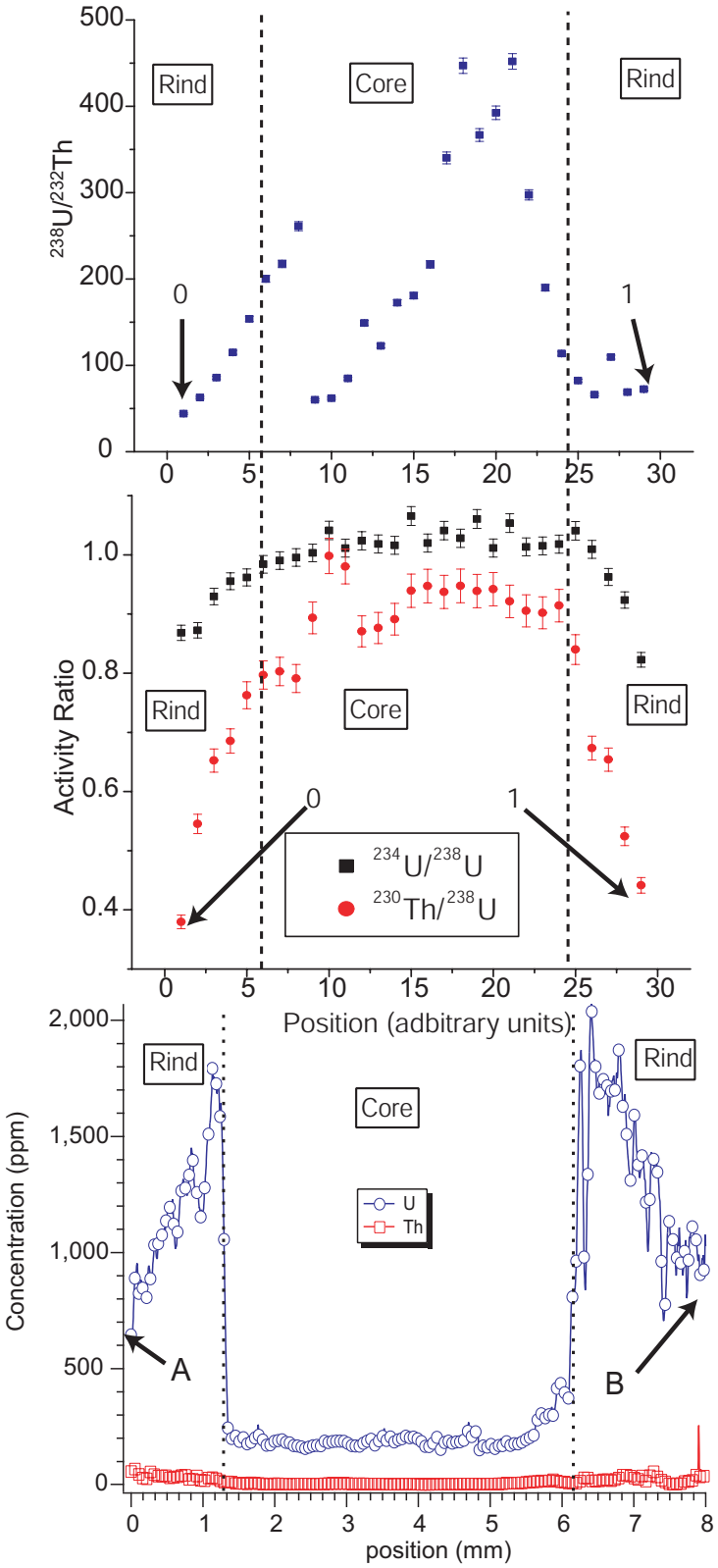

Figure 6. Typical $^{234}U/^{238}U$-$^{230}Th/^{238}U$-$^{238}U/^{232}Th$ profiles along transect from pisolith P03. Error bars are 1.5% for $^{234}U/^{238}U$, 3% for $^{230}Th/^{238}U$ and 2% for $^{238}U/^{232}Th$. Laser beam diameter = 93 µm, sampling rate = 8 Hz. 0 and 1 show start and end of transect respectively. Bottom: Concentration profiles obtained by LA-ICP-QMS. Dashed lines indicate core/rind contact zone.

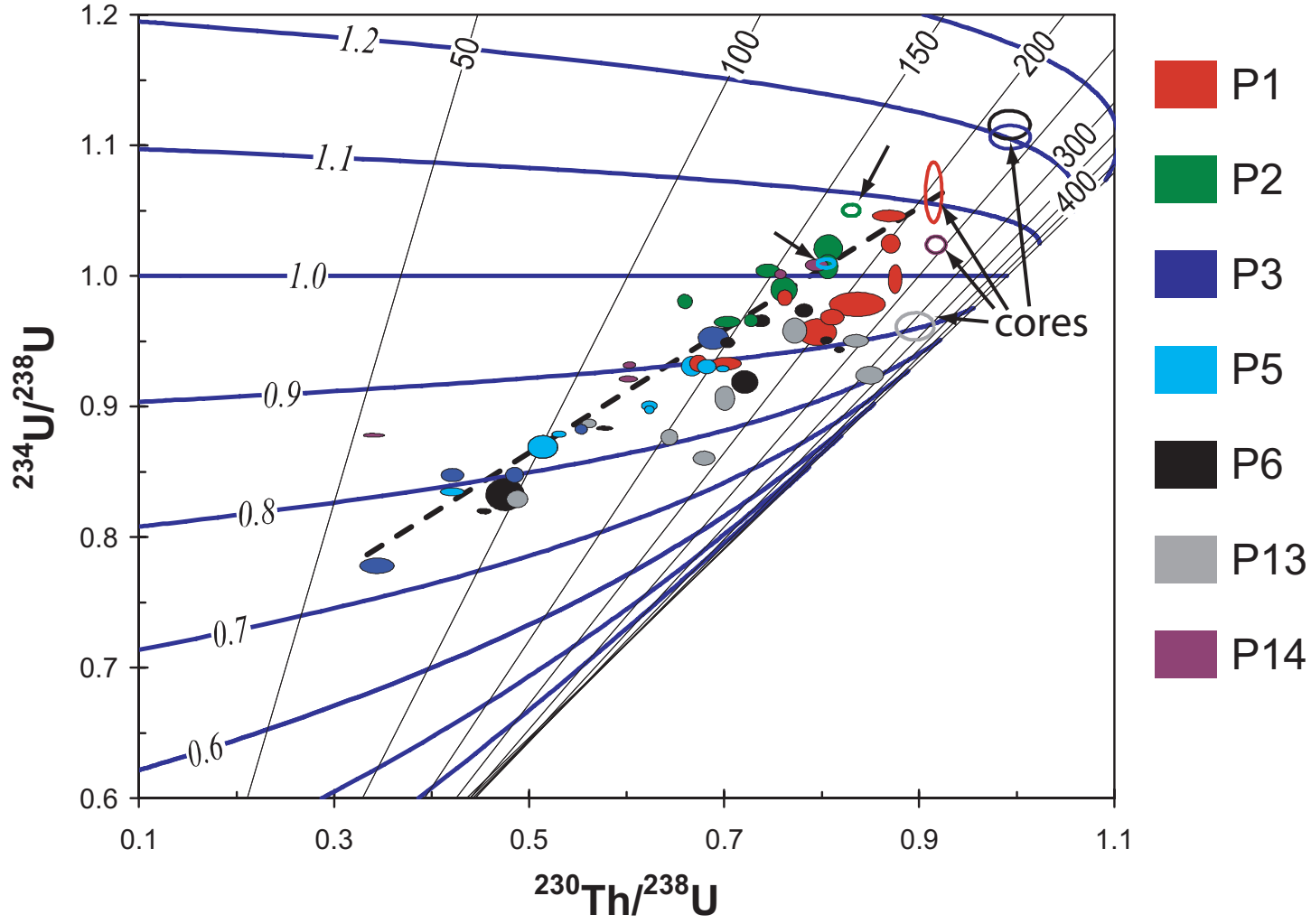

Figure 7. ^{238}U-^{234}U-^{230}Th evolution diagram with the results from all the pisoliths, including hematite- and goethite-rich cutans and their respective cores (open symbols) Error are 2-σ. Dashed line indicates possible mixing line. All activity ratios are presented in the appendix. Ages are in ka.

APPLICATION OF SHRIMP FOR U-PB AND U-SERIES DATING OF OPAL

S.L. Simons and A.A Nemchin

CRC LEME, Curtin University of Technology, Perth

INTRODUCTION

The wide distribution of opal in the weathering profile, combined with its ability to concentrate U, makes it particularly useful for the dating of surface processes. The presence of U opal is explained by co-precipitation of U with silica in groundwater (Ludwig *et al*. 1980, Neymark *et al*. 2002). It is believed that the water carrying both dissolved silica and uranyl ions evaporates depositing U-rich opal, layer after layer. This process helps effective separation of U from Th and Pb, since the latter two elements are less soluble in water. The absence of Th and Pb opal reduces the uncertainties, associated with the correction for initial Th and Pb, which is required for the age calculations. The layer-by-layer deposition of silica also makes opal veins and coatings, observed within the weathering profiles, extremely inhomogeneous with respect to both U concentration and age. This inhomogeneity is evident on a macro and micro scale resulting in the need for minimal sample size and thus, the potential use of microanalytical techniques. This manuscript discusses the application of a new technique, developed at Curtin University of Technology, which utilizes SHRIMP (Sensitive High Resolution Ion Microprobe) for dating of opaline silica. The advantage of this technique, compared to the conventional Thermal Ionisation Mass Spectrometry (TIMS), is a significant increase in the spatial resolution. SHRIMP allows the analysis of a 20-30 μm spot on the surface of a sample as opposed to an average 1 mg fraction required for TIMS. In addition, all isotopes necessary for both U-Pb and U-series dating can be analysed in a single SHRIMP run, whereas TIMS involves chemical extraction and the separate analysis of Pb, U and Th. However, the small amount of material used in the SHRIMP analysis as well as the requirement of a suitable correction standard in order to obtain accurate Pb/U and Th/U ratios in the samples, results in significant reduction of analytical precision, when compared to TIMS. The small size of samples used for SHRIMP analysis also limits applicability of the technique to opal with concentrations of U in excess of ~30 ppm. Smaller concentrations result in an insufficient count rate on the least abundant isotopes such as ^{234}U and ^{230}Th.

Existing methods include analysis of all U, Th and Pb isotopes required for both U-Pb and U-series dating. This results in the relatively long runs. However, such extended cycles appear to be necessary for a number of reasons, despite the fact that some measured isotopes are not used for the final age calculation of each particular spot or sample. First of all, it allows applying a standard analytical procedure to all samples of unknown age, while the set of isotopes that are most suitable, in each case, for the age calculation can be selected during the data reduction. In addition, there are opal samples where ages can vary significantly between individual layers from a few million years to a few thousand years.

Opals with the ages between about 0.5 and 1.5 Ma often display ^{234}U that is not in equilibrium with ^{238}U. The best way to estimate the age of such opals is to use the ^{238}U-^{234}U-^{206}Pb system, which allows simultaneous calculation of ^{206}Pb/ ^{238}U age, corrected for the initial access of ^{234}U and the initial ^{234}U/^{238}U activity ratio. The ^{234}U and ^{230}Th in secular equilibrium with ^{238}U, found in older opals, gives a degree of confidence in closed system behavior of analysed samples, whereas the concordance between the ^{238}U-^{234}U-^{206}Pb and ^{230}Th ages increases reliability of results in the younger opals.

ANALYTICAL TECHNIQUE

A SHRIMP analysis of an individual spot consisted of 5 scans over 12 peaks at masses ^{197}Au (2 sec integration time), ^{204}Pb (30 sec), 204.1-background (30 sec), ^{206}Pb (20 sec), ^{208}Pb (20 sec), 209 (10 sec), ^{238}U (3 sec), ^{246} ThO (30 sec), ^{248} ThO (5 sec), ^{250} UO (30 sec) and ^{254} UO (1 sec). Mass

calibration was done using masses 197 and 254 and the background was measured near mass 204, which is similar to the approach used in U-Pb zircon analyses. The retardation lens was used to reduce the background during all runs. Mass 209 was included to monitor potential Pb hydrides, which were anticipated since opal contains variable quantities of water. However, the intensity of this mass was never significantly above the background and it was not used at the data reduction stage. The primary beam of $^{16}O^{2-}$ was kept above 10 nA in order to contain sufficient counting rates for the isotopes with low abundances.

The Pb/U and Th/U ratios in unknown samples were calibrated against the opal M-21277 from Virgin Valley, Nevada (USA). It is an amorphous porcelanous opal of biogenic origin, which has a U concentration up to 850 ppm (Paces et al. 2003) and an average $^{207}Pb/^{235}U$ age of 2.20 Ma (Amelin & Neymark 1999). U-series TIMS analyses of this opal show that the $^{230}Th/^{238}U$ and $^{234}U/^{238}U$ ratios are within analytical uncertainty of secular equilibrium values (Paces *et al*. 2003), hence this 'standard' is classified as being in secular equilibrium. Macroscopically it is homogeneous; however, backscatter electron imaging reveals evidence of compositional heterogeneities on the scale of tens of micrometers that are associated with its diatomaceous origin (Paces *et al*. 2002).

The analytical procedure developed for commonly analysed U-bearing accessory minerals, such as zircon, have been altered to cater for U-Pb opal analysis. Relatively young ages of opal result in the accumulation of relatively small amounts of radiogenic Pb. In addition Pb isotope composition can be distorted by the incorporation of initial quantities of intermediate products of U-decay. This leads to a need to include measurements of the intermediate daughters in the analytical procedure as well as analyzing several isotopes with very small abundances, which require longer integration times. The large number of mass stations with long integration time, compared to traditional U-Pb analysis of zircon, results in the significantly longer time required for the analysis; usually one run takes about 30-40 min. SHRIMP data reduction traditionally involves calculation of best fit lines for individual isotopes, based on the number of counts versus the time of a particular integration. The best fits for these isotopes are extrapolated to the same point in time. The single value for each isotope is then used to calculate ratios, while error calculations are based on counting statistics. Relatively long SHRIMP runs required for opal analysis result in a large proportion of data not showing linear relationships when the number of counts for individual mass stations are plotted vs. time, especially for the most abundant masses ^{238}U and ^{254}UO. Both of these masses show the maximum number of counts in the middle of the run but this maximum is rarely supported by similar behavior of less abundant isotopes of Th and Pb. This feature cannot be explained by the fluctuations of "gross" secondary beam and more likely reflects variations in the extraction of different species. Therefore, an attempt to fit a line using observed data would result in either accepting a poorly constrained fit or rejecting some of the counts, which are not necessarily the outliers but reflect nonlinear behavior of the data. In order to combat this problem the approach described by Paces *et al*. (2003) was adopted for initial data reduction. It involves the summing of total counts for individual masses. The obtained sums are divided by the cumulative integration times, in order to transfer to counts per second values for all isotopes. Uncertainty calculations are based on counting statistics.

Several sets of standards analysed confirm the conclusion of Paces *et al.* (2003) that the Th/U ratio is constant within error during the SHRIMP session and is independent of variation in $^{238}U/^{254}UO$. However, there is slight variation of $^{230}Th/^{238}U$ between the individual SHRIMP sessions. The average value of this ratio for standards analysed during six sessions is only 0.4% above the secular equilibrium ratio, but varies between the sessions from about 4% below to about 3% higher than the secular equilibrium ratio. True $^{230}Th/^{238}U$ activity ratios were obtained by the division of measured $^{230}Th/^{238}U$ in unknowns by the average of $^{230}Th/^{238}U$ ratios in the standard obtained during the SHRIMP day. A coefficient derived by division of this average by the secular equilibrium $^{230}Th/^{238}U$ ratio was used to correct the $^{232}Th/^{238}U$ ratios in the unknowns. This is based on the assumption that both ^{230}Th and ^{232}Th behave similarly. The corrected $^{232}Th/^{238}U$ ratios were consequently used for the ^{208}Pb based common Pb corrections.

The systematic difference in UO/U ratios that are dependent on the primary beam appear to correlate with the drift in the Pb/U ratios, so that all analyses fall along the single trend in the Pb/U

vs UO/U coordinates. There is also a change in the Pb/U ratio, which is correlated with the spot burning time or overall duration of analysis and which is not correlated with the changes in the observed UO/U ratios. Nevertheless the Pb/U ratios in unknowns were corrected in a manner similar to that used in a zircon analysis with the assumption that if an unknown is analysed at exactly the same conditions as the standards, then the calibration line obtained for the standard during the session could be applied to correct unknowns.

DATING OF UNKNOWN OPAL SAMPLES

U-Pb system (dating of opals older than 1 my)

A sample of hyalite from Guadalajara, Mexico, represents an example of relatively old opal, where intermediate products of U decay are in secular equilibrium. U-Pb systematics is therefore the only way to obtain an age of this sample. The opal occurs within the cavities in volcanic rocks from the basaltic plateau near Guadalajara, which is a part of the Trans-Mexican Volcanic Belt. The rocks are believed to have been formed between 11 and 7.5 Ma (Ferrari *et al*. 2000). A relatively precise U-Pb dating of the hyalite sample is possible since the $^{206}Pb/^{204}Pb$ ratios are high, ranging between ~200 and several thousand, resulting in a relatively small common Pb contribution. Both 204 and 208 corrections give similar $^{206}Pb/^{238}U$ ratios and calculated $^{207}Pb/^{235}U$ ratios have errors ranging between 8 and 17 %. Plotted on a Concordia diagram, the data show expected reverse discordance and spread of $^{206}Pb/^{238}U$ ages, whereas $^{207}Pb/^{235}U$ ratios remain constant within the errors (Figure 1). This behavior appears to be common in opals, which often contain ^{206}Pb unsupported by *in situ* U decay and is explained by the initial excess of ^{234}U. $^{207}Pb/^{235}U$ ages appear to be unaffected by this kind of problem and the average of these ages may be considered as the best estimate of the true age. The average for this sample is 10.4±0.6 Ma (95% confidence) and is similar to the upper limit of age intervals defined for the host rocks accumulation (Ferrari *et al*. 2000). The initial $^{234}U/^{238}U$ activity ratio can be also calculated using measured $^{206}Pb/^{238}U$ ratios and the $^{207}Pb/^{235}U$ age. If the $^{207}Pb/^{235}U$ ages of individual spot analyses are used in such calculations, the initial $^{234}U/^{238}U$ activity ratio varies from 1.1±2.5 to 6±2.6, with the exception of two analyses showing negative values of –1.5±5 and 4±4 and all analyses giving an average of 3±2

U-series systematics (opals younger than ~ 300 kyr)

A sample collected near Yalgoo in Western Australia represents river valley calcrete developed over the Precambrian rocks of the Yilgarn Craton. In this sample, carbonate is crosscut by opal veins varying in width from less than 1 mm to a few mm. One vein, 3 mm in thickness, (Figure 2) was analysed during two SHRIMP sessions. The first one was used to make a series of measurements in the central, intermediate and contact parts of the vein (Figure 3). In addition, analyses of the central and near contact parts of a thinner vein branching from the main vein were made. A single profile, with the distance between the analysed spots equal to 1-2 spot sizes, was made during the second session.

All analyses indicate that ^{234}U and ^{230}Th systems are not in secular equilibrium, making the $^{230}Th/^{238}U$-$^{234}U/^{238}U$ ages the most appropriate method for the vein dating. The relatively young age of the sample makes the $^{207}Pb/^{235}U$ ratios extremely imprecise.

$^{230}Th/^{238}U$-$^{234}U/^{238}U$ ages decrease systematically from the centre of the vein to the contact. The profile, consisting of 20 analytical spots distributed evenly over 3 mm between the two contacts, shows a range of ages from ~150 kyr in the middle to about 80-90 kyr in the outer parts of the vein (Figure 4). The additional 15 analyses in groups of three are placed symmetrically in the middle, near the contacts and at the mid-distance between the center of the vein and its contacts (Figure 3). The vein is slightly thicker in this area, compared to the site of the continuous profile, and is close to 3.6 mm. The ages near the contacts in this area are as low as 60-70 kyr. The observed difference between two profiles is correlated with the thickness of the vein and suggests that the growth rate of opal was constant along the vein, so that the silica in the center was deposited at ~150 kyr. The deposition continued until ~60 kyr in the thickest parts of the vein. The analysed branching vein is approximately 1 mm thick. The ages vary from ~110 kyr to ~70 kyr, suggesting that it was formed later and opal deposition continued synchronously with the deposition in the outer parts of larger vein. Assuming that the deposition rate is constant, it can be estimated as ~22±11 μm/kyr on the

basis of analytical results for the thicker part of the main vein and the branching vein. The analyses for the continuous profile can be interpreted in three possible ways, which cannot be resolved within the large errors of individual spot results. The first way assumes a constant growth rate, which in this case can be estimated as 35±30 μm/kyr (Figure 4). However, analyses suggest a change in the growth rate when plotted on the age vs distance diagram. An extreme interpretation is that the central part of the vein (~30% of thickness) was deposited almost instantaneously at about 139±28 kyr. This was followed by a break in deposition and then the near contact parts of the vein formed very quickly at around 90±11 kyr. The third explanation for the observed data is that the initial fast deposition when the ~0.8 mm thick layer of opal was formed within ~10 kyr starting from ~150 kyr (deposition rate ~80 μm/kyr), was followed by a decrease in deposition rate between ~140 and 100 kyr. This decrease in the rate to about 10 μm/kyr resulted in additional deposition of a ~0.4 mm layer on each side of existing layer. The final increase in the deposition rate resulted in the accumulation of additional 0.8 mm layers of silica near the present contacts of the vein within the following 10-20 kyr.

If the last interpretation is accepted as a working model, some degree of correlation is revealed by comparison of variation in the observed opal growth rate with the global temperature curve (Jouzel, *et al*. 1987) in the time interval for 150 to 50 kyr (Figure 5). A peak on the global temperature curve between ~140 and 110 kyr corresponds to the period of slower opal deposition. The global temperatures corresponding to this peak vary from ~4^{o}C below to 2^{o}C above the average modern temperature. The opal deposition rate apparently increases when the global temperature falls for more than 4^{o}C below today's temperatures. This observation suggests that the opal deposition rate increases under the cooler climate conditions.

Three main factors can influence opal deposition from the ground water. The first one is silica dissolution-precipitation kinetics. However, the kinetic rate constants become smaller with decreasing temperature, which must result in the slower deposition rate. This contradicts apparent faster deposition under the cooler conditions, observed in the sample. The other two factors are groundwater evaporation rate and the supply of silica. The former also contradicts an observed decrease of opal growth rate during the time periods characterised by high global temperature. This high global temperature implies an increase in overall evaporation rate. The silica supply must be proportional to the annual water precipitation rate and may explain observed variations in opal deposition, assuming that the cooler climate is accompanied by an increase in rainfall.

CONCLUSIONS

SHRIMP dating of two opal samples with the ages of ~10 Ma and 60-150 kyr has shown internally consistent results indicating that the method is applicable to the dating of relatively old (>1 Ma) as well as the young (<300 kyr) silica samples. Examples of dating of opal with intermediate ages are given elsewhere (Paces *et al*. 2003, Neymark *et al*. 2000, Nemchin et al in preparation). As discussed by Neymark *et al*. (2000) $^{230}Th/^{238}U$ activity ratios in the opals of this age are usually equal to one, suggesting that the system is in secular equilibrium. However, $^{234}U/^{238}U$ system is often not equilibrated in such samples, due to slower decay of ^{234}U, compared to the decay of ^{230}Th. Therefore, despite the fact that the calculation of $^{207}Pb/^{235}U$ ages is precluded by insignificant accumulation of ^{207}Pb in the system and that the age interval is beyond the limits of $^{230}Th/^{238}U$-$^{234}U/^{238}U$ systematics, it is still possible to calculate age from the $^{206}Pb/^{238}U$ ratios corrected for the initial excess of ^{234}U. This correction is made possible by the "live" ^{234}U present in most of the samples of this age. An advantage of the SHRIMP analysis apart, from the high spatial resolution, is that all required isotopes are measured in a single run. Depending on the time when the analysed sample was formed, either of three approaches can be used for the later age calculations.

The wide distribution of silica in regolith profiles combined with the very limited age data-set makes the area of application of SHRIMP opal dating virtually unlimited. The accumulation of opal age data in the future will increase the understanding of the temporal distribution of silica within the weathering profile.

ACKNOWLEDGEMENTS

The project was supported by an AusIndustry grant to AN and a CRC LEME PhD scholarship to SLS. We thank Bob Fagan and Malcolm McCulloch for their comments on the earlier version of manuscript.

REFERENCES

AMELIN YU.A. & NEYMARK L.A. 1999. Opal as U-Pb geochronometer, *1999 Goldschmidt Conference Abstracts*. Geochemical Society, p. 7335.

FERRARI L., CONTICELLI S., VAGGELLI G., PETRONE C.M. & MANETTI P. 2000. Late Miocene volcanism and intra-arc tectonics during the early development of the Trans-Mexican Volcanic Belt, *Tectonophysics* **318**, 161-185.

JOUZEL J., LORIUS C., PERFIT J.R.., GENTHON C., BARKOV N.I., KOTLYAKOV V.M. & PETROV V.N. 1987. Vostok ice core: a continuous isotope temperature record over the last climatic cycle (160,000 years), *Nature* **329**: 403-403.

LUDWIG, K.R., LINDSEY, D.A., ZIELINSKI, R.A. & SIMMONS, K.R. 1980. U-Pb ages of uraniferous opals and implications for the history of beryllium, fluorine, and uranium mineralization at Spor Mountain, Utah. *Earth & Planetary Science Letters* **46**, 221-232.

NEYMARK L.A., AMELIN YU.A. & PACES J.B. 2000. ^{206}Pb–^{230}Th–^{234}U–^{238}U and ^{207}Pb–^{235}U geochronology of Quaternary opal, Yucca Mountain, Nevada, *Geochimica et Cosmochimica Acta* **64**, 2913-2928.

NEYMARK L.A. & PACES J.B. 2002. Consequences of slow growth for ^{230}Th/U dating of Quaternary opals, Yucca Mountain, NV, USA, *Chemical Geology* **164**, 143-160.

NEYMARK L.A., AMELIN YU.A., PACES J.B., & PETERMAN Z.E. 2002. U-Pb ages of secondary silica at Yucca Mountain, Nevada: implications for the paleohydrology of the unsaturated zone, *Applied Geochemistry* **17**, 709-734.

PACES, J.B., LUDWIG, K.R., PETERMAN, Z.E. & NEYMARK, L.A. 2002. U-234/U-238 evidence for local recharge and patterns of ground-water flow in the vicinity of Yucca Mountain, Nevada, USA. *Applied Geochemistry* **17**, 751-779.

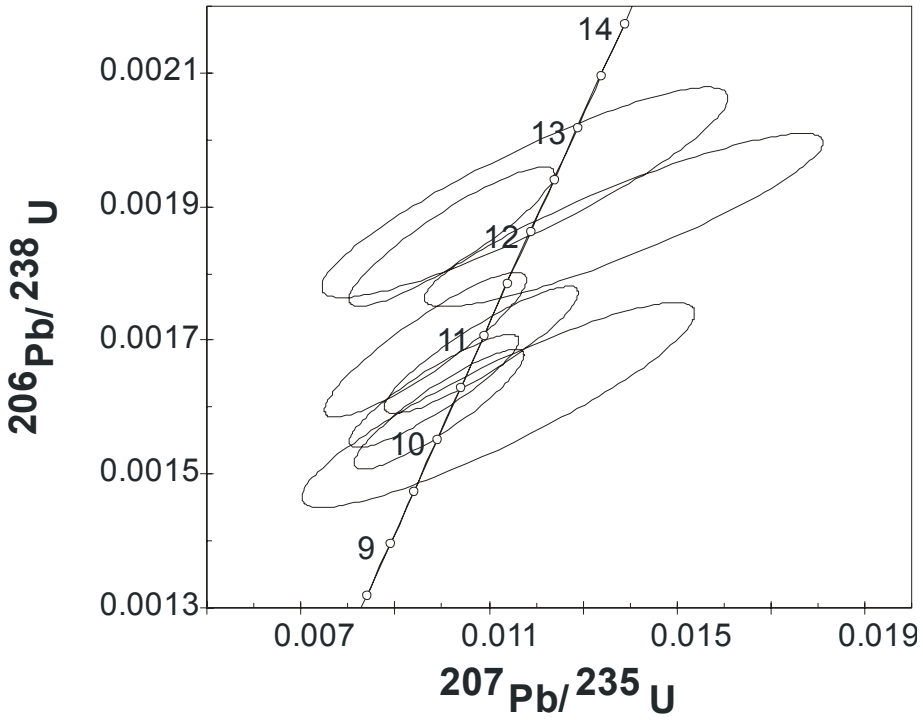

Figure 1. Results of U-Pb analysis of Guadalajara hyalite plotted on a Concordia diagram.

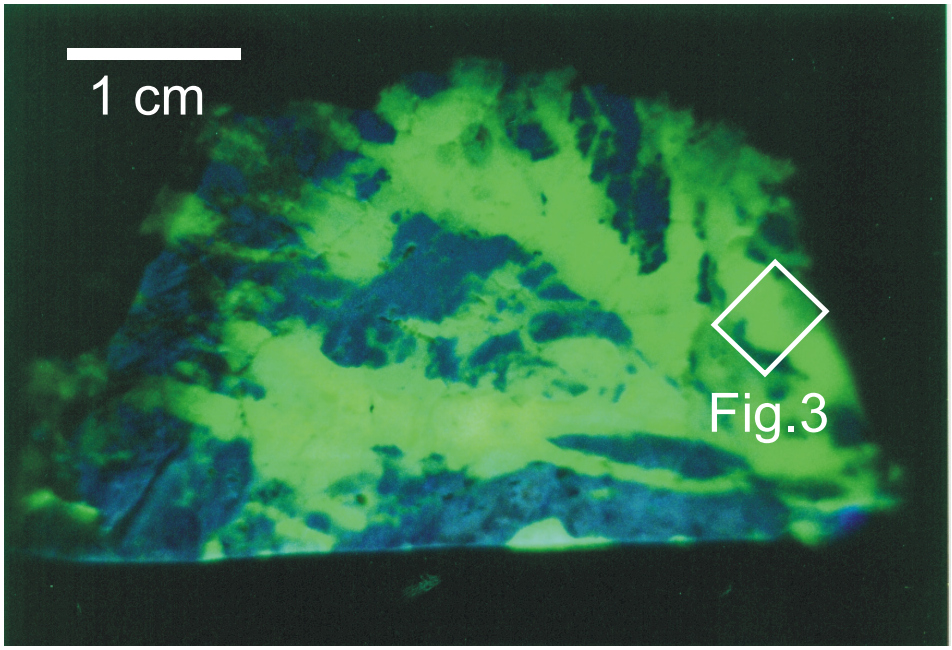

Figure 2. Calcrete sample (from Yalgoo) under short wave ultraviolet light. Calcite is crosscut by the silica veins, which show green fluorescence when placed under a UV lamp. Area analysed by SHRIMP is shown by the white rectangle.

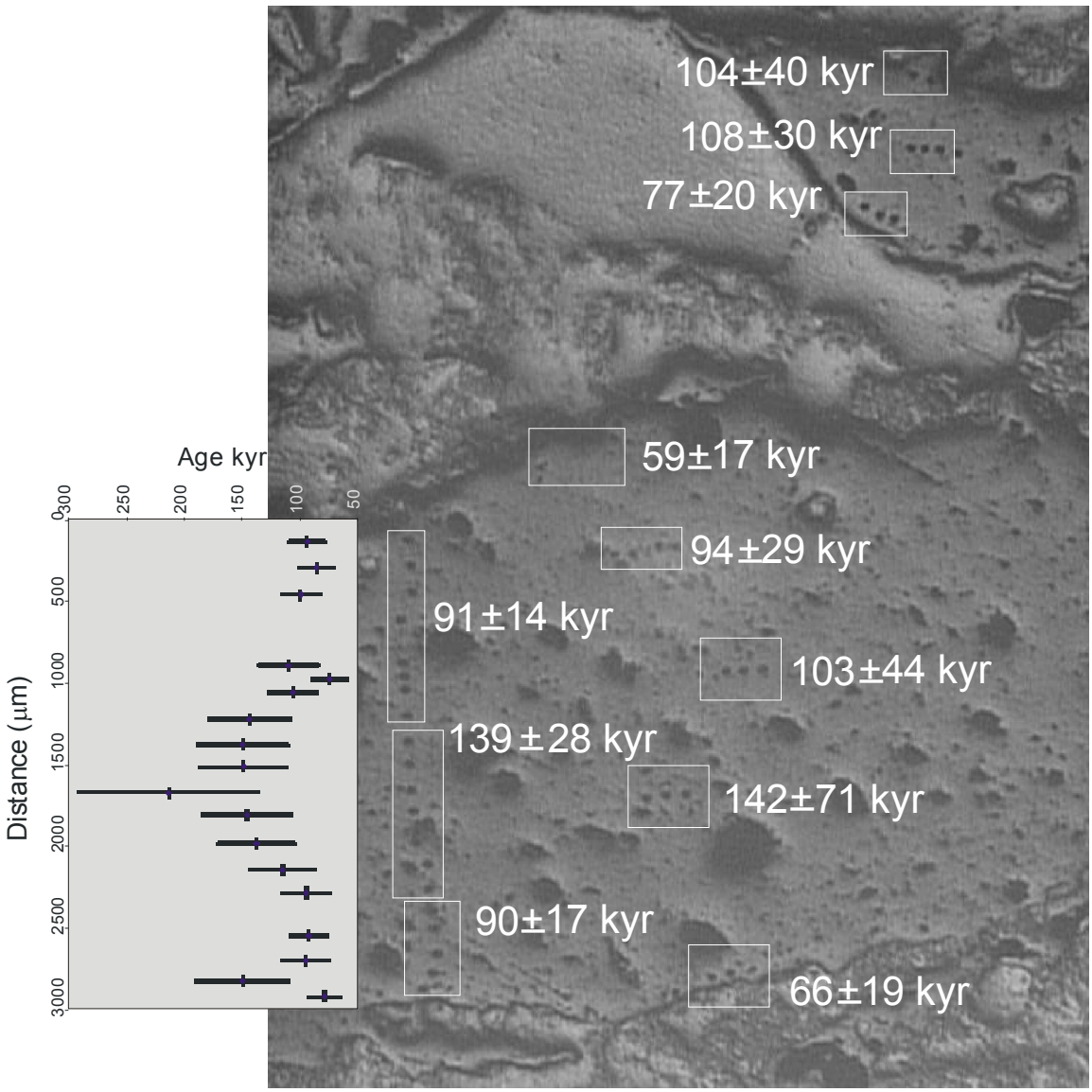

Figure 3. Portion of Yalgoo calcrete sample analysed using SHRIMP, with analytical spots visible on the surface. $^{230}Th/^{238}U$-$^{234}U/^{238}U$ ages correspond to the averages calculated from results for the spots included in the rectangles. The line of analytical spots at the left can be presented as a single traverse across the vein (also shown in Figure 4).

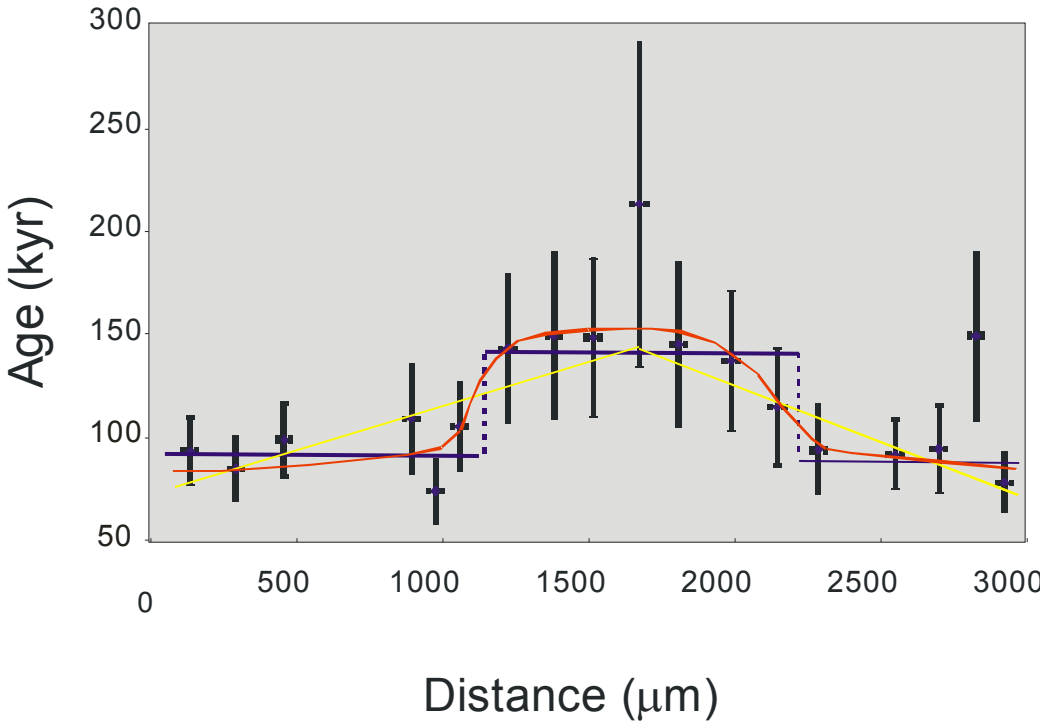

Figure 4. Age distribution along a continuous profile across the main vein in the Yalgoo calcrete sample. Possible interpretations of observed data are shown as: yellow line -constant deposition rate; blue line – two stage instantaneous deposition interrupted by 50 kyr break; red line – fast deposition followed by slower deposition followed by another period of fast deposition.

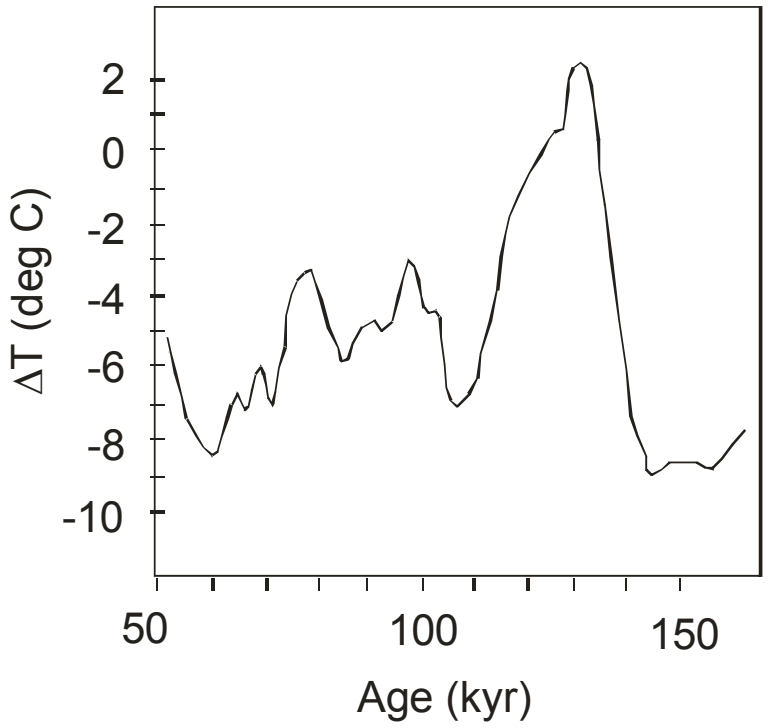

Figure 5. Global temperature variation between 50 and 160 kyr (Jouzel *et al*. 1987).

K-AR AND ^{40}AR/^{39}AR DATING OF K-MN OXIDES

W. J. Dunlap

CRC LEME, Research School of Earth Sciences, ANU, Canberra, ACT, 0200

INTRODUCTION

Potassium-argon and its variant, the $^{40}Ar/^{39}Ar$ method, based on the decay of K to Ar, are commonly used to determine precise ages of K-bearing minerals such as micas, feldspars and amphiboles. Less common minerals that contain K, particularly alteration and ore minerals, can also be dated provided that both the K and daughter product Ar are present in sufficient quantities for analysis, and that the system has remain closed throughout the time of interest.

There is a class of Mn minerals that contain sufficient K that makes them useful for dating purposes. As shown by Dammer *et al*. (1999) and Vasconcelos *et al.* (1995), the psilomelane group minerals, commonly referred to as manganese oxides, do retain daughter product Ar quantitatively, and are unlikely to lose the Ar provided the minerals are kept at near-surface temperatures, and that the mineral structure is not altered after formation.

In this contribution, two examples of dating K-Mn oxides from the Flinders Ranges, South Australia, are presented, one of a Pb-rich psilomelane called coronadite from Beltana and the other a Mn oxide from Trinity Well. In principle the approach adopted here can be used to date a variety of psilomelane group minerals.

BELTANA WILLEMITE DEPOSIT

Beltana is a high-grade willemite (Zn_2Si0_4) deposit hosted in Lower Cambrian carbonate rocks in the Arrowie Basin, Northern Flinders Ranges, South Australia (e.g. Groves *et al*. 2003). Debate concerning the origin of the deposit has centred on whether the willemite is of supergene or hypogene origin, with recent work (e.g. Groves *et al*. 2002; Brugger *et al*. 2003) favouring the latter. The deposit is situated adjacent to a major growth fault on the basin margin. Ooid grainstone units of the Woodendinna Dolomite and units of *Archaeocyathid*-rich Wilkawillina Limestone are the main host lithologies. Sub-economic lead mineralization is hosted in karstic collapse breccias surrounding the willemite ore bodies.

As noted by Groves *et al*. (2003), mineralization is structurally controlled and associated with brecciation and extensive hematite-rich hydrothermal zincian dolomitization. Ore minerals include willemite and coronadite with lesser mimetite, hedyphane and smithsonite. Late-stage gangue minerals include mangano-calcite, dolomite and minor quartz. The texture of willemite is heterogeneous, resulting from various depositional mechanisms, including partial to massive replacement of the carbonate host rock, internal sedimentation, fracture fill, brecciation and vein fill. Smithsonite formed by weathering of willemite occurs on the periphery of the deposit.

The work of Groves *et al*. (2002, 2003) showed that Beltana is centered on a karstic collapse breccia with at least 100 m of vertical extent, formed in part through corrosion by acidic ore solutions. The geochemical signature of the ore body is enhanced levels of Zn-Pb-Cd-As-Mn. Notably, silver is absent from the deposit and sulfur concentrations are low (<20 ppm). Fluid inclusion studies yield a low minimum temperature range of ore deposition between 50 and 170°C, and indicate mixing of brine and meteoric fluids as a depositional mechanism.

Two samples of massive, opaque coronadite from the Pb ore body at Beltana were collected for K-Ar dating (Groves *et al.* 2003). Coronadite selected for dating shows clear cross-cutting relationships with the willemite ore-body and, based on textural studies (Figure 1), is temporally related. The specimens were uncontaminated by host rock at the 1% level; no transparent minerals were observed in crushed aliquots under oil immersion. The siting of K in these samples may be in the large central cation tunnel of the cryptomelane group structure (Vasconcelos *et al*. 1995). Procedures for K-Ar dating are identical to those outlined by McLaren *et al*. (2002) unless otherwise noted.

Dissolution of the coronadite in acid was difficult. The best K yields were obtained by dissolution in hot, weak HCl (~13% by wt.) for 36 hours, evaporation to dryness, with a reflux in concentrated HF and HNO_3. Minor white precipitate was present at the final stage of dissolution and is likely lead chloride assumed to not sequester K. A lithium internal standard was added to the solutions and the K contents were assessed by flame photometry (Table 1). The two maximum K yields from a set of six dissolutions were used to calculate the preferred sample ages. Any underestimate of K content would lead to an overestimate in the age of the samples, a discrepancy possibly revealed through a subsequent programme of $^{40}Ar/^{39}Ar$ analysis.

For Ar determination, gas was extracted from fused coronadite aliquots under vacuum at 1200-1240 °C for 25 minutes and an ^{38}Ar tracer was added to the gas subsequent to fusion. The spiked gas was cleaned over copper oxide and titanium getters before analysis by a mass spectrometer. The combined results for K and Ar analysis are presented in Table 1.

Table 1. K-Ar data for Beltana coronadites.

No.	Material	K wt %	Rad ^{40}Ar, 10^{-9} mol/g	Radiogenic ^{40}Ar %	Age Ma ± 1 σ
Bel-01	Coronadite	0.589	0.5050	88.8	437 ± 5
		0.588			
		(0.583)			
		(0.582)			
		(0.556)			
		(0.532)			
Bel-02	Coronadite	0.166	0.1392	35.6	430 ± 5
		0.164			
		(0.158)			
		(0.156)			
		(0.153)			
		(0.132)			

K is potassium. Decay constants are λ_e=0.581 x $10^{-10}y^{-1}$ and λ_β=4.962 x $10^{-10}y^{-1}$ (Steiger & Jäger 1977). Ages are calculated using the highest two yields from set of 6 dissolutions for K. K analysis by flame photometry using lithium internal standard, calibrated against Australian National University GA1550 biotite. Full data available from W. J. Dunlap upon request.

The preferred ages for the coronadite samples are Ordovician: 437 ± 5 Ma (Bel-01) and 430 ± 5 Ma (Bel-02). The argon retention of cryptomelane group minerals is excellent (Vasconcelos *et al*. 1995). The potential for argon loss due to thermally activated diffusion was minimal with the low temperatures experienced by the samples, as confirmed in studies by co-workers on associated fluid inclusions. In addition, the potential for modification of the K-Ar chronometer by dissolution-precipitation processes subsequent to coronadite formation in these two samples is considered unlikely based on textural evidence. The two ages are similar, indicating reproducibility. K-Ar dating of the coronadite indicates a preferred age of formation at ~435 ± 5 Ma, which demonstrates post-Delamerian (<~450-500 Ma; McLaren *et al*. 2002) Pb-Zn mineralization possibly relating to an exhumation event.

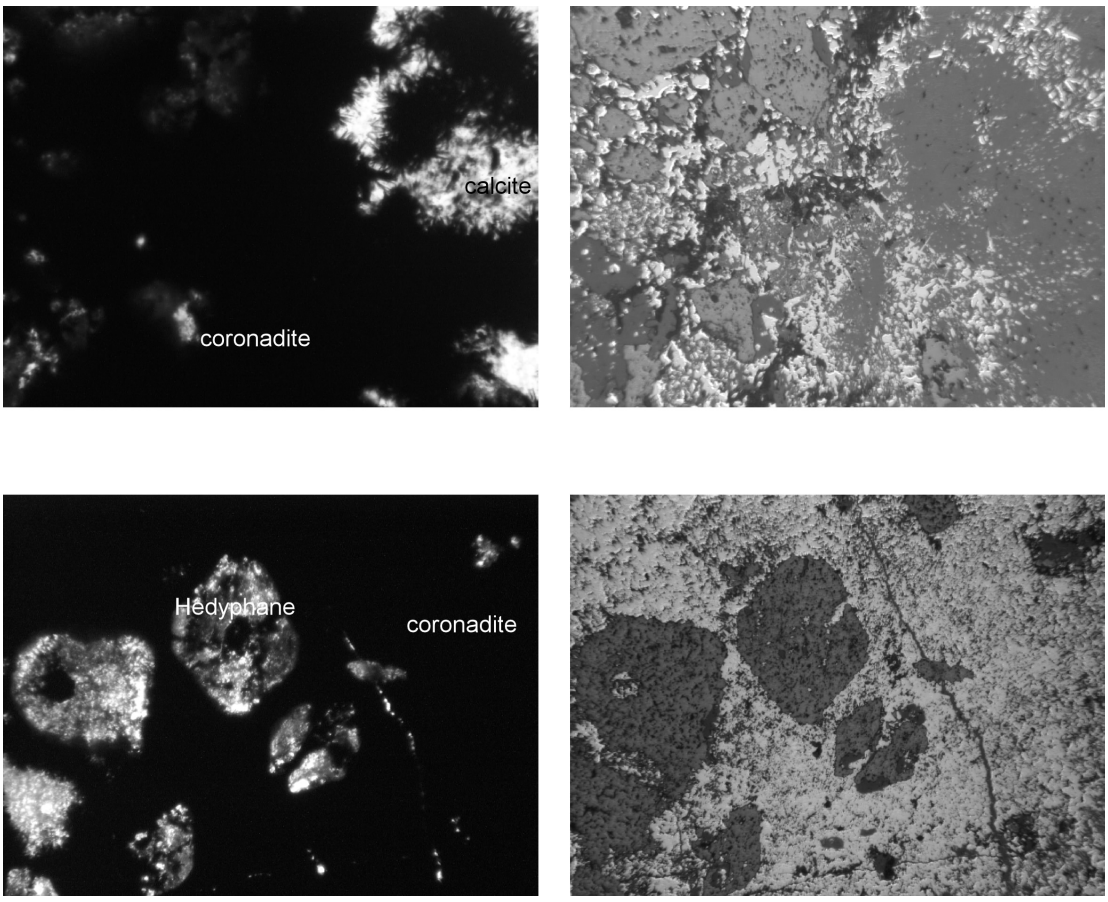

Figure 1. Photo micrographs of two samples containing coronadite; left in transmitted light and right in reflected light. Note the variation in texture of the coronadite, from massive (Bel-01, below) to blocky or brecciated (Bel-01, top); field of view ~3.5 mm, long dimension.

TRINITY WELL

Near Trinity Well, in the northernmost Flinders Ranges, Alley & Frakes (2003) reported the first known tillite (Livingston Tillite) of Cretaceous age. The Cretaceous sediments, containing the tillite, unconformably overlie weathered Late Proterozoic rocks, which include a pod of Mn oxides several metres wide. In outcrop, the Mn oxides appeared likely to have formed during an episode of supergene weathering that predated the tillite. An age for the Mn oxides would therefore provide a maximum age for the tillite, and also potentially date a period of near-surface weathering.

A brief and variably successful argon isotopic dating study of Mn oxide from Trinity Well was undertaken. A small aliquot (~2 grams) was crushed and sieved, with the 125-90 micron fraction retained for dating purposes. This fraction was rinsed and deslimed in deionized water by ultrasonication for 30 seconds, then left to dry. The sample is dark brown in colour and appears homogeneous and free of detrital minerals, as observed under a binocular microscope. No other textural or chemical analysis of the sample was undertaken.

A 50 mg split of the sample (LIV-001) was packed in a 5 mm ID silica tube, in-line with $^{40}Ar/^{39}Ar$ standard GA1550 biotite and irradiated for six days at the HIFAR reactor, Lucas Heights, New South Wales. Subsequently, 31.93 mg of the split was packed in Sn foil, placed under vacuum and baked at 180 °C for 16 hours. Prior to isotopic analysis the sample was dropped into the crucible of a double-vacuum resistance furnace and degassed at ~350 °C for 30 minutes. Temperature at the outside base of the crucible was monitored by a thermocouple inserted into a notch located within a few millimetres of the sample. During analysis, radiogenic ^{40}Ar and reactor induced ^{39}Ar were released from the sample by heating for 12 minutes during each of 12 extraction steps, at progressively higher temperatures, in the range of 650-1450 °C (Table 2).

Following generation of each gas aliquot, analysis of the isotopic composition of the gas was undertaken with a gas-source magnetic-sector mass-spectrometer. Between each extraction step the temperature was lowered to 500 °C, during which time the evolved gas was analysed. This procedure is called "step heating" and the results are collectively known as an age spectrum (McLaren *et al*. 2002).

The results of step heating of the LIV-001 sample show marked discordance (Table 2), with apparent age rising from a minimum of 305 Ma at 650 °C to a maximum at 577 Ma at 760 °C. Subsequent steps decrease in age to a minimum of 279 Ma at 1000 °C. The markedly higher ages of the highest temperature steps (1350, 1450 °C) are typically discarded in this type of analysis due to contamination by small amounts or residual furnace gas. An integration of the evolved gas yields an average age of 444 Ma. Moreover, the age spectrum is "hump-shaped" and is difficult to interpret. The K/Ca, a product of this type of analysis, ranges between 1 and 4, indicating similar concentrations of K and Ca in the sample. Regardless, the age spectrum suggests that subsequent to its formation the sample experienced loss of radiogenic ^{40}Ar, as indicated by the strong age gradients.

Given the results of step heating of the LIV-001 Mn oxide it was decided that laser fusion analysis of individual fragments might shed further light on the age and homogeneity of the sample. Individual fragments (~100 microns in diameter) of the remaining irradiated material were loaded into 1mm conical cells of a copper planchette and placed under vacuum. Baking of the system was done in a manner identical to that outlined above, with the exception that the fragments were not preheated at 350 °C prior to analysis. A 10W argon ion laser was used to fuse each fragment at ~1600 °C for 2 min to extract the argon gas, with subsequent analysis of the entire gas aliquot from each fragment in one step. Twenty-five fragments were analysed and 23 produced enough gas for their bulk age to be determined. The results are presented in Table 3.

Table 2. Step heating $^{40}Ar/^{39}Ar$ Data for LIV-001 Mn oxide.

Temp (°C)	$\%^{40}Ar^*$	Cumulative $\%\ ^{39}Ar$	$^{40}Ar/^{39}Ar_K$	Calculated Age (Ma)	Error in Age (± 1σ)	K/Ca
LIV-001: 31.93 mg, Mn Oxide, J=0.004676 ± 0.35%						
650	91.1	19.1	39.42	305	1	1.7
700	90.6	35.8	63.30	468	2	2.2
730	96.5	48.4	77.92	561	2	2.9
760	98.4	57.5	80.67	577	2	3.9
800	97.8	68.5	70.81	516	2	3.8
830	96.8	76.4	62.19	461	2	3.1
880	96.8	85.2	54.26	408	2	2.7
930	98.0	92.4	49.20	374	1	2.7
1000	96.1	97.4	35.73	279	1	1.9
1120	76.5	99.4	47.52	362	5	1.2
1350	22.0	99.9	89.61	631	41	10.0
1450	1.4	100.0	772.4	2758	27041	1.0
		Totals	59.63	444	4	

Table Correction Factors: $(^{36}Ar/^{37}Ar)_{Ca}=3.50 \times 10^{-4}$, $(^{39}Ar/^{37}Ar)_{Ca}=7.86 \times 10^{-4}$, $(^{40}Ar/^{39}Ar)_K=0.027$, $(^{38}Ar/^{39}Ar)_K=0.13$, $^{38}Ar_{Cl}/^{39}Ar_K=8.0$

Table 3. Laser Fusion $^{40}Ar/^{39}Ar$ Data for LIV-001 Mn oxide. The first nine analyses are the oldest of the set; 1-8 used to calculate relative probability in Fig. 2.

Analysis	$\%^{40}Ar^*$	Cumulative $\%^{39}Ar$	$^{40}Ar/^{39}Ar_K$	Calculated Age (Ma)	Error in Age ($\pm 1\sigma$)	K/Ca
LIV-001: Single Fragment, ~100 micron, Mn Oxide, J=0.004676 ± 0.35%						
1	91.2	13.4	58.64	437	3	2.4
2	88.7	16.2	60.85	452	11	0.4
3	87.9	18.9	56.90	426	13	-
4	95.5	23.6	58.86	439	6	1.8
5	94.7	36.9	59.86	445	5	2.1
6	92.9	40.4	57.64	431	10	-
7	91.6	45.1	61.02	453	8	-
8	85.5	48.3	60.64	450	21	0.6
9	94.7	89.6	63.75	471	9	2.0
10	78.8	57.8	52.87	399	30	0.6
11	58.9	58.9	27.81	221	42	0.2
12	93.7	66.9	53.25	401	4	0.6
13	67.4	67.7	44.28	340	30	0.1
14	80.8	69.4	49.72	377	11	-
15	93.6	79.6	51.62	390	4	-
16	81.7	82.2	39.86	308	18	0.5
17	63.6	82.6	24.03	192	95	0.1
18	72.5	84.6	36.54	285	21	0.4
19	92.7	56.2	54.43	409	5	1.0
20	85.4	93.7	47.23	360	9	0.4
21	91.5	96.7	53.43	402	10	-
22	83.7	98.6	41.23	318	21	0.4
23	51.7	100.0	10.25	84	35	0.1
		Totals	54.33	408	9	

Table Correction Factors: $(^{36}Ar/^{37}Ar)_{Ca}=3.50 \times 10^{-4}$, $(^{39}Ar/^{37}Ar)_{Ca}=7.86 \times 10^{-4}$, $(^{40}Ar/^{39}Ar)_K=0.027$, $(^{38}Ar/^{39}Ar)_K=0.13$, $^{38}Ar_{Cl}/^{39}Ar_K=8.0$. Some measurements of ^{37}Ar were below detection limit (note K/Ca= -), but this is not expected to affect the calculated ages by more than 1%.

From the laser analyses we can conclude that there is inhomogeneity at the grain scale, as indicated by both K/Ca values, and a range of young ages. If all of the gas in the 23 analysed fragments is integrated a bulk age of 408 Ma is calculated, as compared to the 444 Ma bulk age of the much larger step heated fraction. This difference in bulk age is consistent with the notion of inhomogeneity at the scale of the laser analyses, but it suggests a deeper problem: Preheating and degassing of the step heated sample at ~350 °C may have preferentially released ^{39}Ar prior to the formal analysis (preferential loss of ^{39}Ar over ^{40}Ar will increase the apparent age of the sample). This possibility of ^{39}Ar loss prior to analysis of the step heated sample is considered likely, in view of the propensity of ^{39}Ar to be released in large quantities in the early, low temperature, gas evolution (for instance the 650 °C step #1, which comprises 19% of the total ^{39}Ar released). It would appear that recoil and implantation of ^{39}Ar during neutron irradiation may leave the ^{39}Ar in a position in the lattice of the oxide that is relatively easily degassed. Moreover, these issues need to be addressed with a more advanced program of analysis. By contrast, the laser analyses yield systematic ages that suggest that primary age information is retained by the sample, as outlined below.

A relative probability histogram of all 23 laser analyses is shown in Figure 2. Two clear maxima are noted, with the most prominent at 440 Ma. Filtering and averaging to include eight of the nine oldest results yields an age of 440 ± 4 Ma (2σ); the oldest analysis, at 470 Ma, was arbitrarily excluded. The preferred age of 440 ± 4 Ma for the Trinity Well manganese oxide is within error of the two preferred K-Ar ages of the Beltana coronadites from the same region.

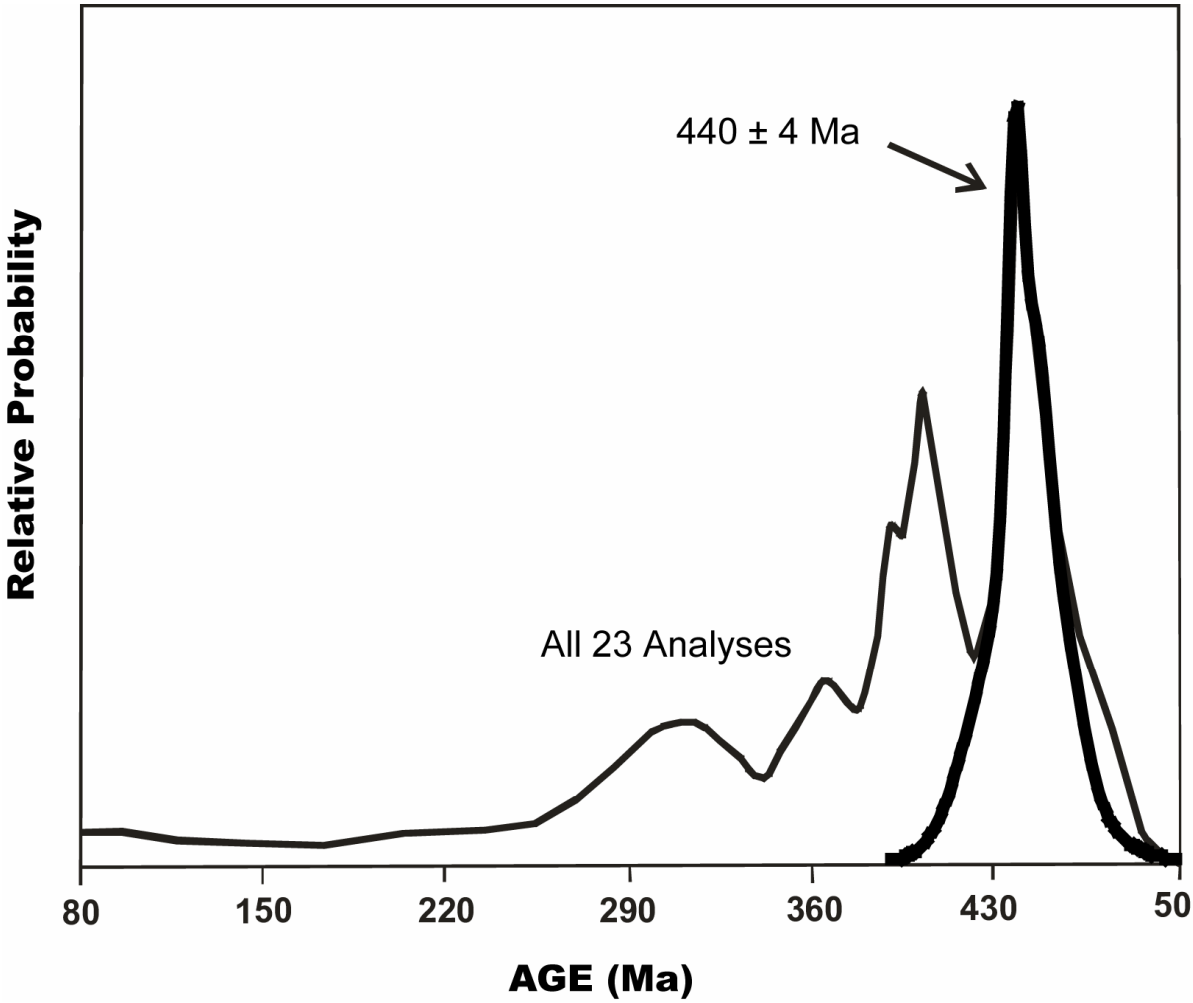

Figure 2. Plot of relative probability versus age for laser fusion analyses. Thin curve is for all 23 analyses combined. Bold curve is for 8 selected analayses, which provide and age of 440 ± 4 Ma (2σ).

To summarize, the step heating analysis of the Trinity Well manganese oxide yields a discordant age spectrum, which is itself of limited value. By contrast, laser fusion analysis of ~100 micron single fragments of the same material suggests that preheating at ~350 °C, prior to step heating analysis,

preferentially released ^{39}Ar from easily-degassed sites. Moreover, laser fusion analyses appear to identify the original formation age of the manganese oxide, as corroborated by regional geochronology (e.g., McLaren *et al*. 2002).

SUMMARY

Exploratory argon isotopic ages of K-bearing Mn oxides have revealed systematic behaviour that may relate to geologic processes in the Australian Paleaozoic of the Flinders Ranges, South Australia. It is suspected that the preferred ages outlined here of the Beltana coronadites and the Trinity Well manganese oxide, which are within error at ~435-440 Ma, are the product of a geologic response to exhumation processes known to be active in the Flinders Ranges at ~440 Ma (McLaren *et al*. 2002, Groves *et al*. 2003). Although the data on these oxides is limited and merits further study, preliminary conclusions are that the Beltana coronadites retain primary formation ages, and the Trinity Well manganese oxides appear to retain, at least in part, their formation age.

REFERENCES

ALLEY N.F. & FRAKES L.A. 2003. First known Cretaceous glaciation: Livingston Tillite Member of the Cadna-owie Formation, South Australia. *Australian Journal of Earth Sciences* **50**: 139-144.

BRUGGER J., McPHAIL D.C., WALLACE M. & WATER J. 2003. Formation of willemite in hydrothermal environments. *Economic Geology* **98**: 819-835

DAMMER D**.,** McDOUGALL I**.** & CHIVAS A**.**R**.** 1999. Timing of weathering-induced alteration of manganese deposits in Western Australia; evidence from K/ Ar and 40Ar/39Ar dating. *Economic Geology* **94**: 87-108.

GROVES I., GREGORY I. & CARMAN C. 2002. Reliance; a new high-grade zinc silicate-oxide discovery in the Flinders Ranges. *MESA Journal* **25**: 6-10.

GROVES I., CARMEN C. & DUNLAP W. 2003. Geology of the Beltana Willemite deposit, Flinders Ranges, South Australia. *Economic Geology* **98**: 797-818.

McLAREN S., DUNLAP W.J., SANDIFORD M. & McDOUGALL I. 2002. Thermochronology of high heat-producing crust at Mount Painter, South Australia: Implications for tectonic reactivation of continental interiors. *Tectonics* **21**: 2-1 to 2-18.

STEIGER R.H. & JAGER E. 1977. Subcommission on geochronology: Convention on the use of decay constants in geo- and cosmochronology. *Earth Planetary Science Letters* **36**: 359-362.

VASCONCELOS P.M., RENNE P.R., BECKER T.A. & WENK H-R. 1995. Mechanisms and kinetics of atmospheric, radiogenic, and nucleogenic argon release from cryptomelane during $^{40}Ar/^{39}Ar$ analysis. *Geochimica et Cosmochimica Acta* **59**: 2057-2070.

TESTING U – PB DATING OF ANATASE IN SILCRETE, WESTERN NSW

M. L. Smith[1], B. J. Pillans[1], S. Eggins[1], G. Mortimer[2], C. Allen[2] and I. Williams[1]

[1]*CRC LEME, Research School of Earth Sciences, ANU, Canberra, ACT, 0200*

[2]*Research School of Earth Sciences, ANU, Canberra, ACT, 0200*

FIELD AREA

Northwestern New South Wales extends from Parkes west through Cobar and Bourke to the South Australian border, and north to Tibooburra and the Queensland border (Figure 1). There are numerous historic and currently active mines in the area, the most significant of which include those at Broken Hill (Pb-Zn-Ag), Cobar (Cu-Au), Northparkes (Cu-Au), Peak Hill (Au), White Cliffs and Lightning Ridge (opal). The potential for further major mineral discoveries is high, but knowledge of landscape and regolith development is increasingly important for successful exploration (e.g. Smith 1996).

Figure 1. Location map of northwestern New South Wales and the Sandstone Tank locality.

Northwestern New South Wales has been sub-aerially exposed since the seas retreated from the Eromanga-Surat Basin in the Albian (~110 Ma) – c.f. Frakes *et al*. (1987). A regional study found evidence for weathering dating back to 100 Ma, with discrete intense weathering events recorded during the Miocene and Palaeocene – Eocene (Smith 2006). Landscape evolution models for the region invoke preservation of processes as far back as the Permo-Carboniferous, and continuous evolution under varying climatic conditions since the latest Cretaceous (e.g., Pillans *et al.* 1999; Gibson 2000; Hill 2000; O'Sullivan *et al.* 2000; Spry 2003).

SILCRETE

Silcrete is a regolith material found throughout Australia, South Africa, parts of Europe and the Americas. The term silcrete was originally proposed by Lamplugh (1902) to describe a conglomerate composed of sand and gravel, cemented by silica into a hard mass. Eggleton (2001) defined silcrete as a strongly silicified, indurated regolith material of low permeability, commonly having a conchoidal fracture and vitreous lustre. Most silcretes are dense and massive, but some may contain boxwork fabrics. The texture, mineralogy and composition of silcretes may reflect the original silicified material. Commonly consisting of 98% silica or more, other phases found in silcretes include iron oxides, anatase, residual zircon and other resistate minerals, in minor and trace amounts (Milnes & Thiry 1992).

Pedogenic and groundwater processes are the main silcrete forming mechanisms in inland Australia (Alley, 1977; Watts, 1978; Wopfner, 1978; Twidale, 1983; Milnes *et al.*, 1991; Ollier, 1991; Thiry & Milnes, 1991; Milnes & Thiry, 1992; Webb & Golding, 1998). Pedogenic silcretes form by downward percolation of solutions through a soil or weathering profile. Extensive leaching results in solubilisation of most phases, and precipitation occurs at porosity or chemical boundaries (Milnes and Thiry, 1992; Watts, 1978). Groundwater silicrete may retain primary structures of host materials and results from absolute silica accumulation (Thiry & Simon-Coincon, 1999). Silicification most probably occurs near a phreatic surface (e.g. Milnes & Thiry, 1992). Throughout the inland portion of Australia, including northwestern NSW, silcretes occur as erosion-resistant caprocks of characteristic mesa and plateau topography.

Whereas silcretes of the Lake Eyre Basin have been thought to define a once extensive paleosurface, the Cordillo Surface (Wopfner, 1974; Wopfner *et al.*, 1974; Wopfner, 1978; Alexandre *et al.*, 2004), in northwestern NSW, silcretes generally represent inverted paleovalley features (e.g. Hill & Roach, 2003). Throughout northwestern NSW, both pedogenic and groundwater silcretes are present.

APPLICATION OF NUMERICAL DATING TECHNIQUES TO SILCRETE

Although the ages of silcretes have been estimated stratigraphically, direct numerical dating of silcretes has not yet been successfully accomplished. If direct numerical dating of silcretes could be accomplished, it would provide an excellent test of landscape evolution models, as silcrete has been used, poorly, as a morphostratigraphic correlation tool, and as a palaeoenvironmental indicator. Palaeontological methods can be used to aid stratigraphic correlation of silcretes, and further constrain their ages. This approach was used at the Stuart Creek silcretes in South Australia, where plant macrofossils revealed that the silcrete formed in sediments sometime shortly after the Miocene (Thiry & Milnes, 1991). The Sandstone Tank silcrete in northwestern NSW also contains abundant macrofloral fossils, which have been dated as Eocene (Figure 2 and Greenwood *et al.* 1997). Other silcretes for which formation ages are based on associated dated materials include those of eastern Australia, where K-Ar and $^{40}Ar/^{39}Ar$ dated basalts of Cenozoic ages overlie the silcretes. Basalts overlying silcretes range in age from Pliocene in Victoria, to Palaeocene in the Monaro region of southeast NSW (Taylor & Smith, 1975; Young & McDougall, 1982). There is debate, however, as to whether the silcretes are sub-basaltic weathering phenomena, occurring post-eruption, or were present prior to when the basalts were erupted (Exon *et al.*, 1970; Wellman & McDougall, 1974). One Electron Spin Resonance (ESR) dating study (Radtke & Brueckner, 1991) has yielded ages for silcretes from Queensland of between 5 and 12 Ma. However, too little is known about the method's applicability to silcrete dating and validation with other numerical methods is required to test the suitability of ESR dating more fully.

U-series and U-Pb dating of opaline silica has been carried out successfully (Neymark *et al.*, 2000; Neymark & Paces, 2000; Ludwig & Paces, 2002; Paces *et al.*, 2004). Studies of Quaternary opal at Yucca Mountain, Nevada, were undertaken to assess past hydrologic conditions at a proposed nuclear waste dump site. Initial investigations focussed on $^{230}Th/U$ dating of sub-millimetre thick samples of opaline silica coating fractures (Neymark & Paces, 2000). The layers themselves showed sub-micron variations in uranium concentration and REE patterns. Results indicated that the opal at Yucca Mountain reflected active hydrology through fracture pathways in the unsaturated zone continuously throughout the Quaternary. The U-Th data were consistent with closed system behaviour, but implied that mineral deposition could not have occurred instantaneously during discrete episodes.

Further work incorporating U-Pb dating with U-series dating supported the previously proposed growth model of slow mineral deposition (Neymark *et al.*, 2000; Neymark *et al.*, 2002). This work provided more accurate average age estimates for the multi-stage, multi-age samples, as ages based on short-lived isotopes are biased by younger mineral additions. The method also significantly extended the age range of the method and showed that the fracture network had been hydrologically active throughout the Quaternary. However, the scale of sampling did not equate with individual growth stages.

Another study, using SHRIMP-RG and microdigestion TIMS techniques, greatly improved spatial resolution (Paces *et al.*, 2004). SHRIMP results yielded average opal growth rates of 0.58 and 0.69 μm/ky. The TIMS study yielded an average growth rate of 0.68 ± 0.22 μm/ky, with faster growth from ~37 to 25 ka, and slower rates from ~25 to 7 ka. The data also indicated that opal had not been deposited in the last several thousand years. The improved spatial resolution obtained in this study provided a more robust test for the model of continuous deposition, and provided a method for fine scale U-series dating of Quaternary opaline silica.

Silcrete can contain abundant titanium oxides, occurring as cryptocrystalline anatase. The most common Ti oxide phase in Australian silcretes is authigenic sub-micron to micro-crystalline grains dispersed through microcrystalline quartz grains as part of the cement. Larger, detrital anatase grains (about 10 – 15 μm in size) are found within the matrix.

Titanium oxides also occur as a grain coating material, composed of very small, sub-micron grains clustered in fuzzy conglomerations. Another easily identified titanium oxide phase is detrital rutile (Milnes & Hutton, 1974; Thiry & Milnes, 1991; Milnes & Thiry, 1992;).

Rutile, of which anatase is a stable, low-temperature polymorph, has been dated using U-Pb methods (Schaerer *et al.*, 1986; Richards *et al.*, 1988; Corfu and Muir, 1989; Mezger *et al.*, 1989; Mezger *et al.*, 1991). These studies focussed on large (>50 μm) grains from metamorphic rocks, and demonstrated that rutile can provide valuable age information using the U-Pb system, as it contains measurable U and incorporates low common Pb during formation. To this end, the anatase present in silcrete was tested for suitability to the U-Pb dating method.

U-Pb dating utilises the differential radioactive decay of ^{238}U to ^{206}Pb and ^{235}U to ^{207}Pb, according to the equations:

$$(^{206}Pb/^{238}U)_t = e^{\lambda 238t-1}$$
$$(^{207}Pb/^{235}U)_t = e^{\lambda 235t-1}$$

where:

$\lambda_{238} = 0.155125 \times 10^{-9}\ yr^{-1}$

$\lambda_{235} = 0.98485 \times 10^{-9}\ yr^{-1}$ (Steiger & Jager, 1977)

Figure 2. Sandstone Tank silcrete with Eocene temperate rainforest flora. Courtesy of S. Hill.

THE SANDSTONE TANK SILCRETE, FOWLERS GAP ARID ZONE RESEARCH STATION

Sandstone Tank Paddock lies at 31^{o} 05' S, 141^{o} 42' E in the northwest of Fowlers Gap Arid Zone Research Station. The Sandstone Tank silcrete is similar in morphology to pedogenic silcretes described by Thiry & Milnes (1991) from Stuart Creek in South Australia. The surface outcrop consists of a pseudobreccia horizon of Adelaidean metasediments, grading up through smaller sized clasts to more massive, tabular silcrete at the top. The more massive portion contains some rounded quartz pebbles, and consists mainly of silicified quartz sand. The pseudobreccia clasts and larger grains are draped by beige-coloured anatase geopetal cappings, also containing iron oxides and silica in varying proportions (Figure 3). The clasts towards the top of the pseudobreccia are draped by thicker caps than those at lower levels. Anatase is also dispersed throughout the more massive portion, either as "flame" structures, or within the cement. Anatase also occurs within some voids and cracks within the clasts. Eocene plant fossils are preserved in the lower horizons of the silcrete, to the east of the site described above. These are described in more detail in Greenwood *et al.* (1997) and Hill (2001).

Thin-sections were cut from the pseudobreccia horizon, specifically around areas rich in anatase. These were analysed by Scanning Electron Microscopy (SEM) and laser ablation ICP-MS (LA-ICP-MS). Other sections were cut from geopetal cappings for micro-sampling using a wafer saw.

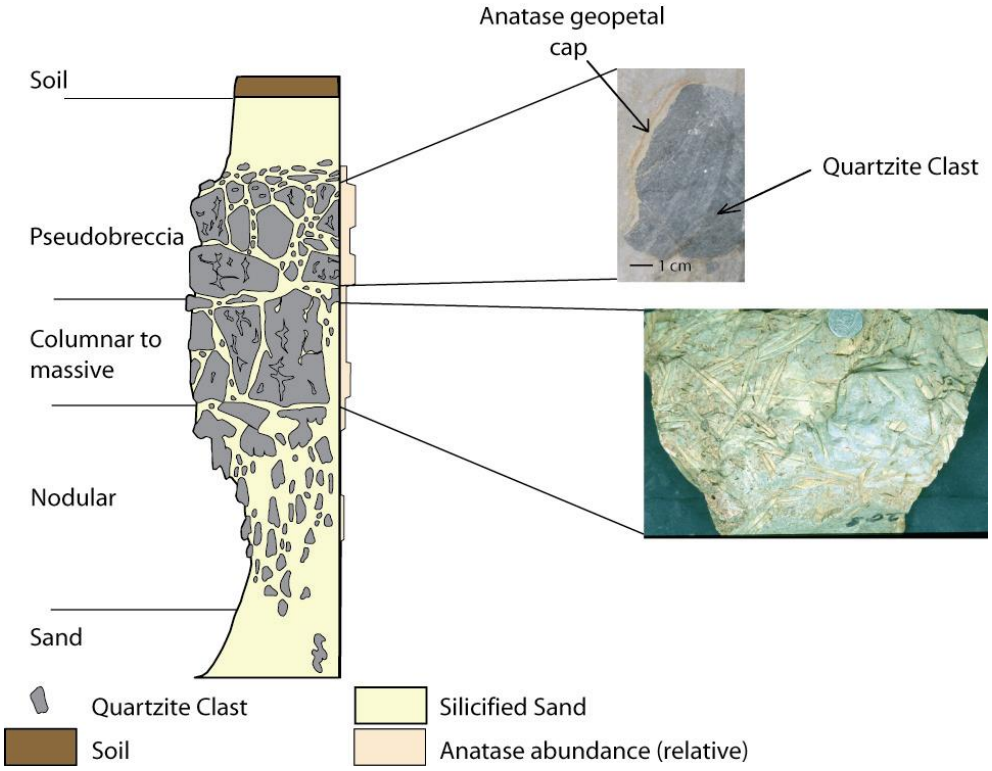

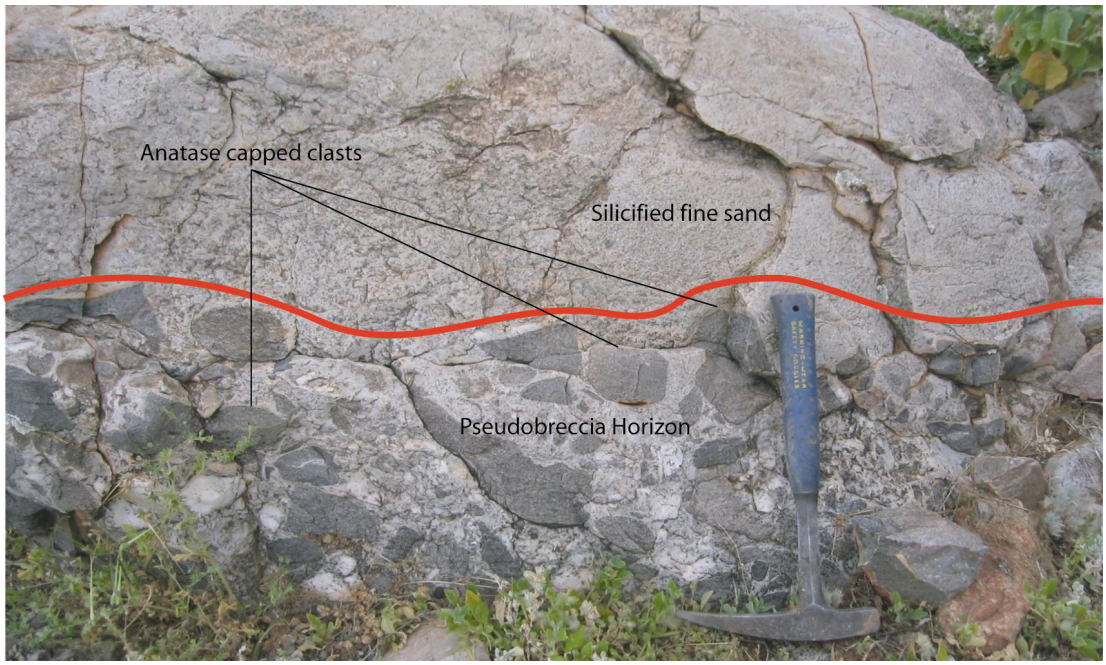

Figure 3A. Schematic section showing horizons and anatase abundance from Stuart Creek silcrete (top), with examples of Sandstone Tank features (top right; after Milnes & Thiry, 1991). Sandstone Tank silcrete outcrop (middle, hammer for scale). Note the demarcation between the pseudobreccia and massive horizons, and the distribution of anatase.

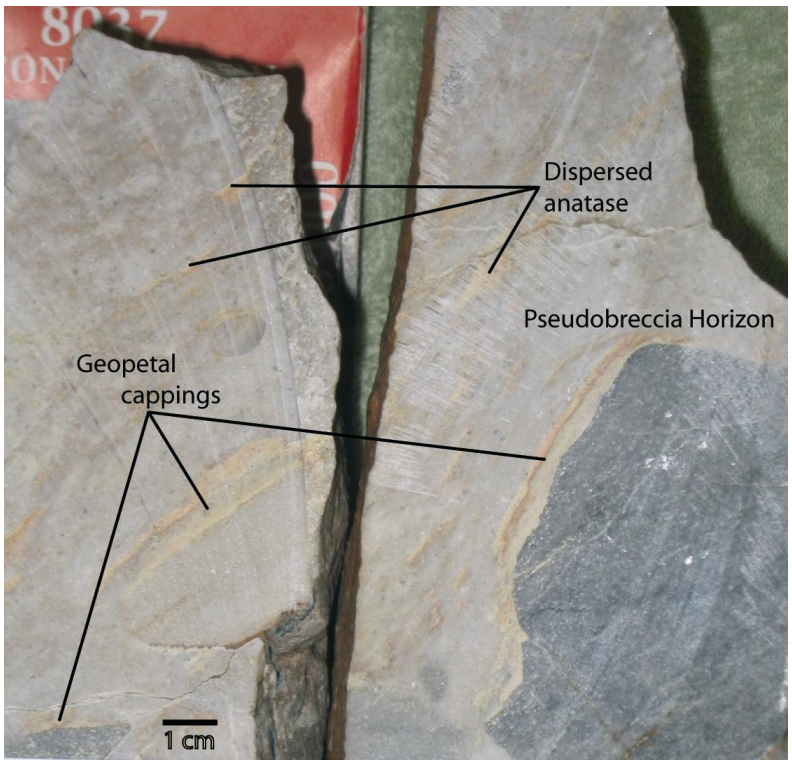

Figure 3B. Sandstone Tank Silcrete sectioned slab, showing the distribution of anatase.

SCANNING ELECTRON MICROSCOPY (SEM)

SEM was carried out on a JEOL JSM6400 scanning electron microscope at the Electron Microscopy Unit, ANU, on sections of silcretes. The primary aim was to assess the morphological relationships between accessory phases, TiO_2 (anatase), and silica in the samples. This was achieved by determining the geochemistry and mineralogy of the main accessory phases and cement utilising energy dispersive x-ray analysis (EDXA) as well as photomicrography. EDXA was carried out to determine concentrations of selected elements (reported as wt.% oxide) in a silcrete section from Sandstone Tank, as an aid to identifying mineral phases (Table 1). Accessory phases are predominantly anatase and zircon (Figure 4), with rare rutile. Zircon and rutile are both detrital, whereas the anatase appears to be predominantly authigenic, with only rare detrital anatase. In most cases, anatase is a late stage phase, occurring as a cementing agent between microcrystalline silica (Figure 5), or replacing other grains (Figure 6). There are three types of cement in the silcretes analysed (Figure 4b). The first is a predominantly silica phase, consisting of microcrystalline silica. The second is a silica-anatase mixture, where very fine anatase grains (~0.5 – 1 μm) are interspersed with similar sized and smaller silica. This cement is found throughout the samples, and in hand specimen appears as beige to light yellow dispersed material. The third type of cement consists of microcrystalline anatase cementing clasts and grains of quartz. This cement occurs predominantly as geopetal cappings on large clasts, and also around larger detrital grains (Figure 5).

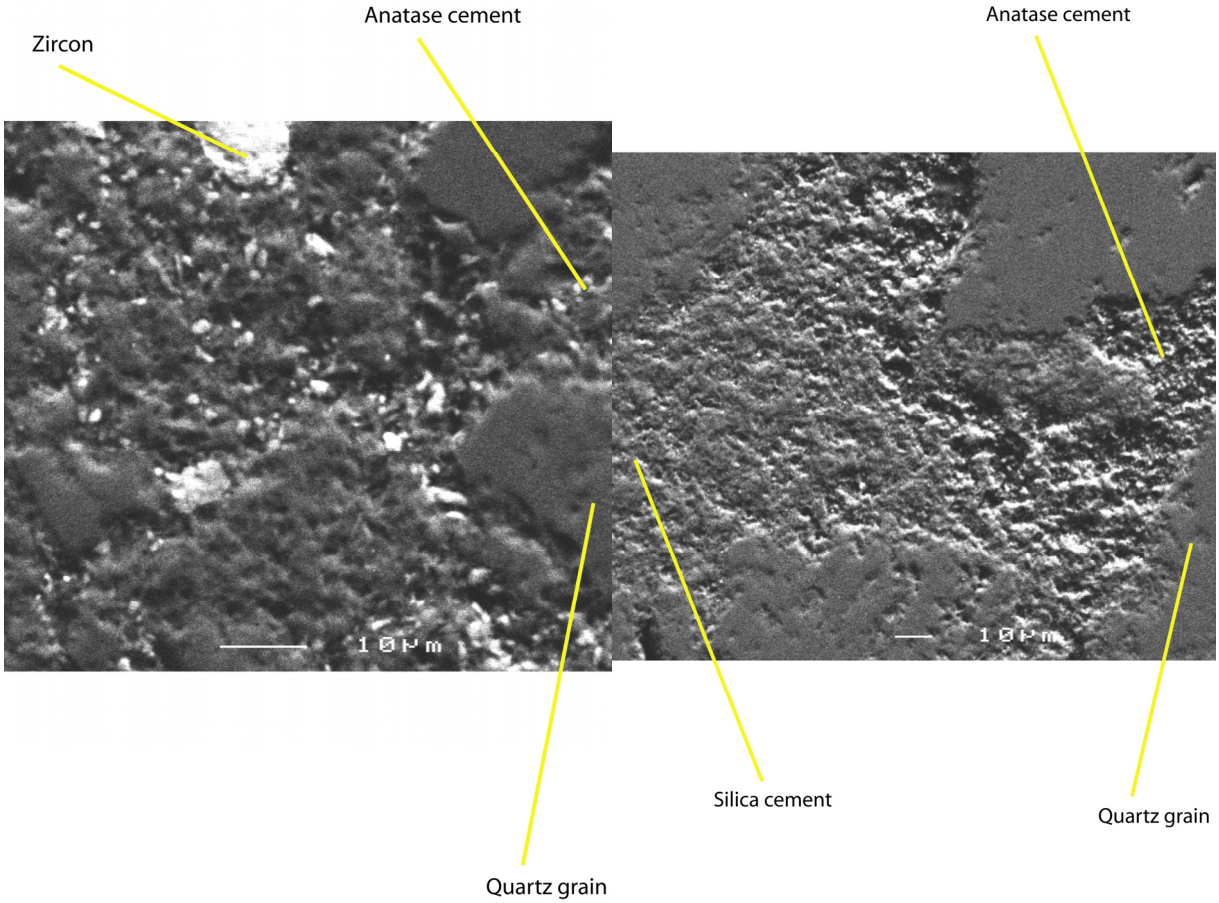

Figure 4. (a) SEM image of silcrete cement. Typical silica-rich cement (dark grey), with detrital zircon (bright white), and anatase (dirty white). (b) Anatase-rich cement (pocked) and silica-rich cement (smooth)

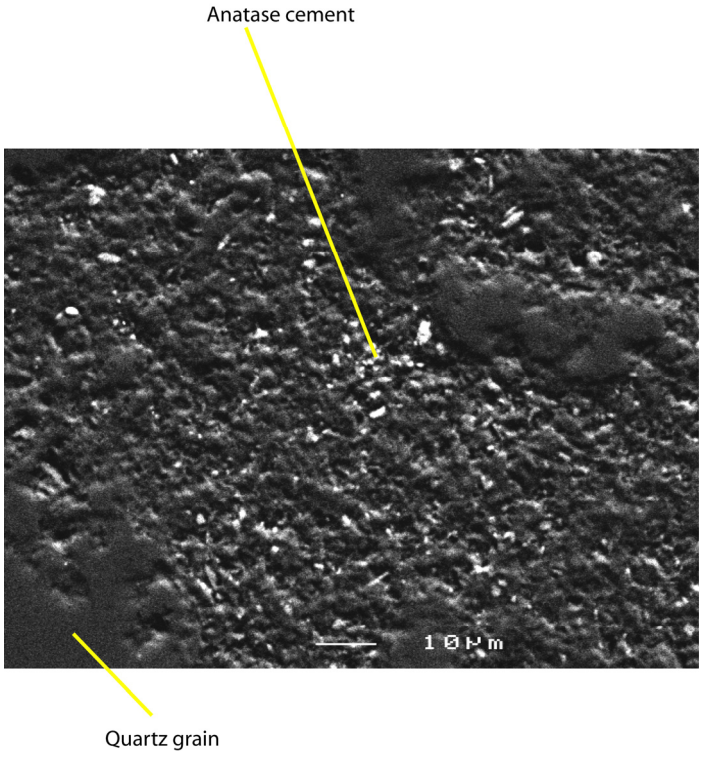

Figure 5. Late stage anatase cementing quartz/silica matrix in Teilta silcrete.

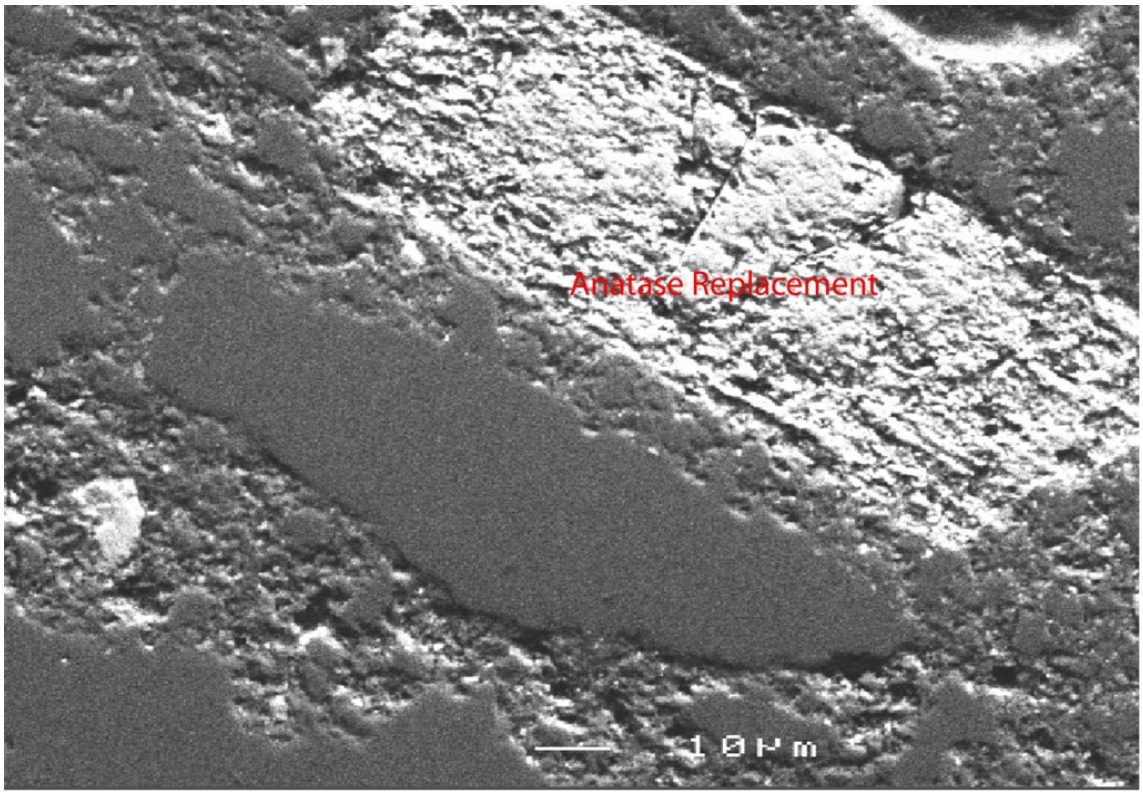

Figure 6. Anatase replacement of a detrital grain in the Sandstone Tank silcrete.

Table 1. Chemistry of various morphologies from SEM of the Sandstone Tank silcrete sample, all results reported as wt% oxide.

Label	CaO	MgO	Al_2O_3	SiO_2	SO	K_2O	CaO
Fine, dispersed Ti oxide in cement	.05	.05	.64	4.96	.26	.00	.09
Ti oxide cement		.03	.84	4.38	.33	.10	.14
Ti oxide		.08		.19	.10		.01
Large Ti oxide grain		.03	.10	.52			.08
Dispersed Ti oxide		.05	.49	4.58		.00	.08
Ti oxide cement	.03	.27	.08	7.19	.44	.15	.32
Dispersed Ti oxide	.03	.03	.12	.65		.01	.03
U rich anatase			.08	.53			.05
Mixed Si/Ti cement	.02		.33	0.40	.26	.00	.02
Silica cement	.14	.00	.08	02.11	.23		.03
Massive silica cement	.17	.03	.28	00.43	.16	.00	
zircon	.11	.30	.96	1.86	.76	.05	.32
Detrital zircon	.07	.11		1.98		.02	
zircon	.28	.12		2.36		.02	
Detrital zircon	.12	.07		1.94			
Quartz matrix	.06	.03	.06	01.17	.13		
Crystalline quartz	.00		.05	02.56	.14		

- = below detection limit

Table 1 (cont).

Label	TiO_2	MnO	FeO	CuO	ZnO	ZrO	total
Fine, dispersed Ti oxide in cement	59.67	0.06	2.66	-	-	0.03	98.39
Ti oxide cement	19.54	0.03	6.78	0.01	0.29	0.84	94.23
Ti oxide	99.13	-	0.16	0.04	-	0.61	99.66
Large Ti oxide grain	93.47	-	1.72	0.29	0.26	-	94.69
Dispersed Ti oxide	62.24	0.17	1.14	0.15	-	-	97.43
Ti oxide cement	13.59	0.02	3.05	0.02	0.01	0.63	88.80
Dispersed Ti oxide	96.95	0.06	0.01	0.18	-	-	97.42
U rich anatase	98.32	0.02	0.16	0.14	0.44	0.52	99.86
Mixed Si/Ti cement	4.89	-	1.93	-	-	-	97.50
Silica cement	0.09	-	0.09	-	0.11	-	102.14
Massive silica cement	0.07	-	-	-	-	-	100.46
Zircon	0.47	-	0.82	-	0.07	59.06	84.89
Detrital zircon	0.20	0.05	-	0.04	-	65.36	97.00
zircon	0.05	0.18	-	-	0.27	65.61	97.15
Detrital zircon	-	-	0.28	-	0.10	65.75	96.88
Quartz matrix	-	-	-	0.38	0.29	-	101.61
Crystalline quartz	0.03	-	-	0.08	-	-	102.28

- = below detection limit

LASER ABLATION INDUCTIVELY COUPLED PLASMA MASS SPECTROMETRY U-PB DATING

A sample from Sandstone Tank was subjected to nine spot U-Pb dates using a laser ablation unit attached to a Hewlett Packard ICP-MS at the Research School of Earth Sciences. The sample remained stationary under the beam, and analysis was carried out over a one minute period. Isotopes ^{49}Ti, ^{57}Fe, ^{202}Hg, $^{204, 206, 207 \& 208}$Pb, ^{232}Th and ^{238}U were measured. Standards were measured before and after each spot. Results are plotted on U-Pb Concordia diagrams in figures 7 to 9. When plotted on a Tera-Wasserburg U-Pb Concordia plot (Figure 7), the ^{207}Pb/^{206}Pb composition of the common lead component from all anatase samples has a value of 0.849 ± 0.058 (2σ errors are reported throughout) that is, the value of ^{207}Pb/^{206}Pb where the chord passes through the samples intersects the Concordia line. Samples cluster towards the common Pb-rich (older) end of the chord, indicating a large proportion of common Pb in the samples. A traditional Concordia plot of all anatase gives a lower intercept age of 266 ± 370 Ma (Figure 8). Anatase without iron oxide contamination gives a lower intercept age of 273 ± 600 Ma (Figure 9).

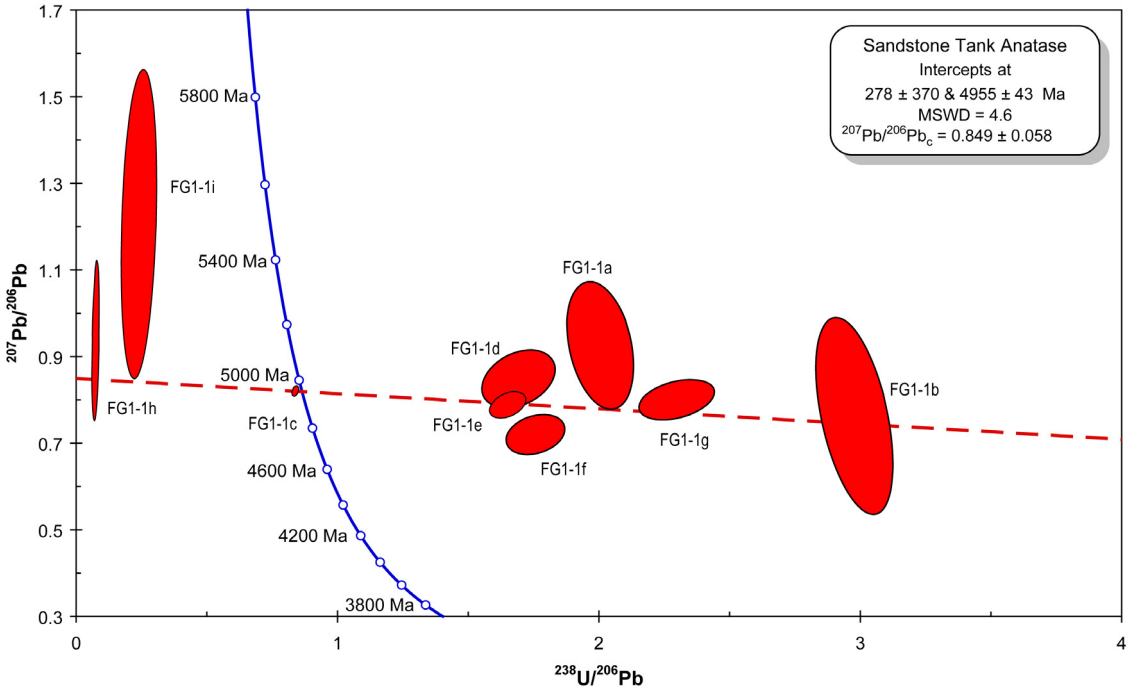

Figure 7. U-Pb Tera-Wasserburg Concordia plot showing data from all Sandstone Tank LA-ICP-MS anatase spots (prepared using Isoplot).

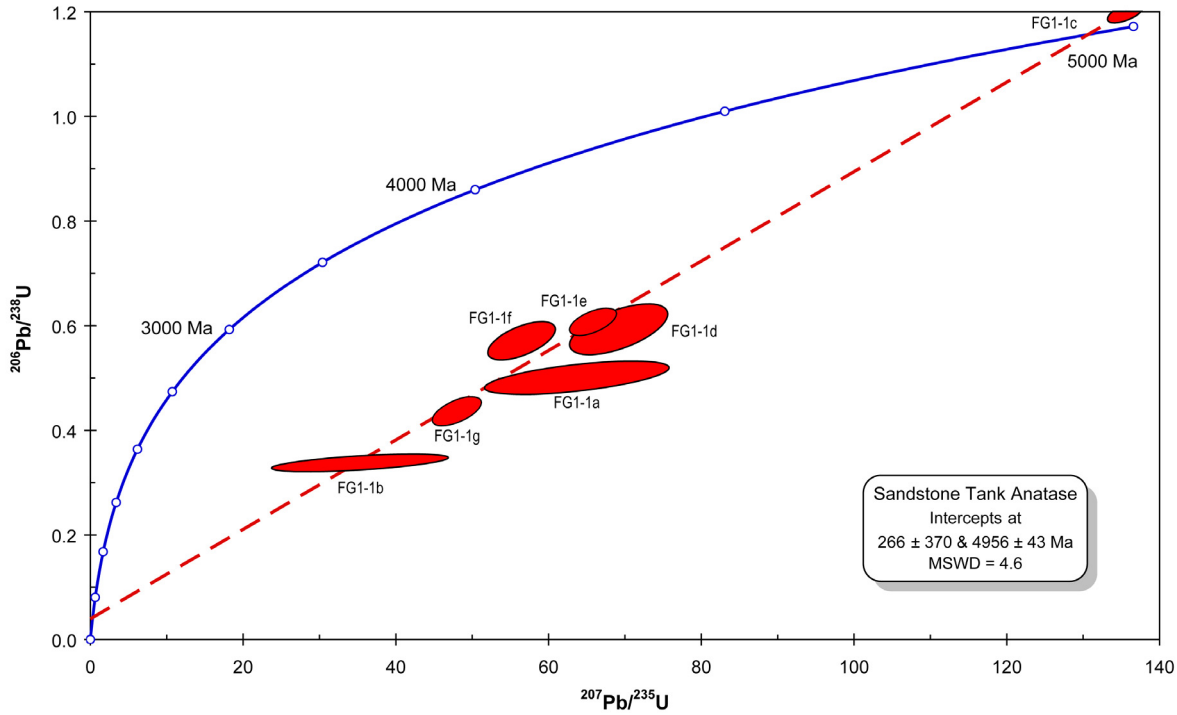

Figure 8. U-Pb Concordia plot showing data from all Sandstone Tank LA-ICP-MS anatase spots (prepared using Isoplot).

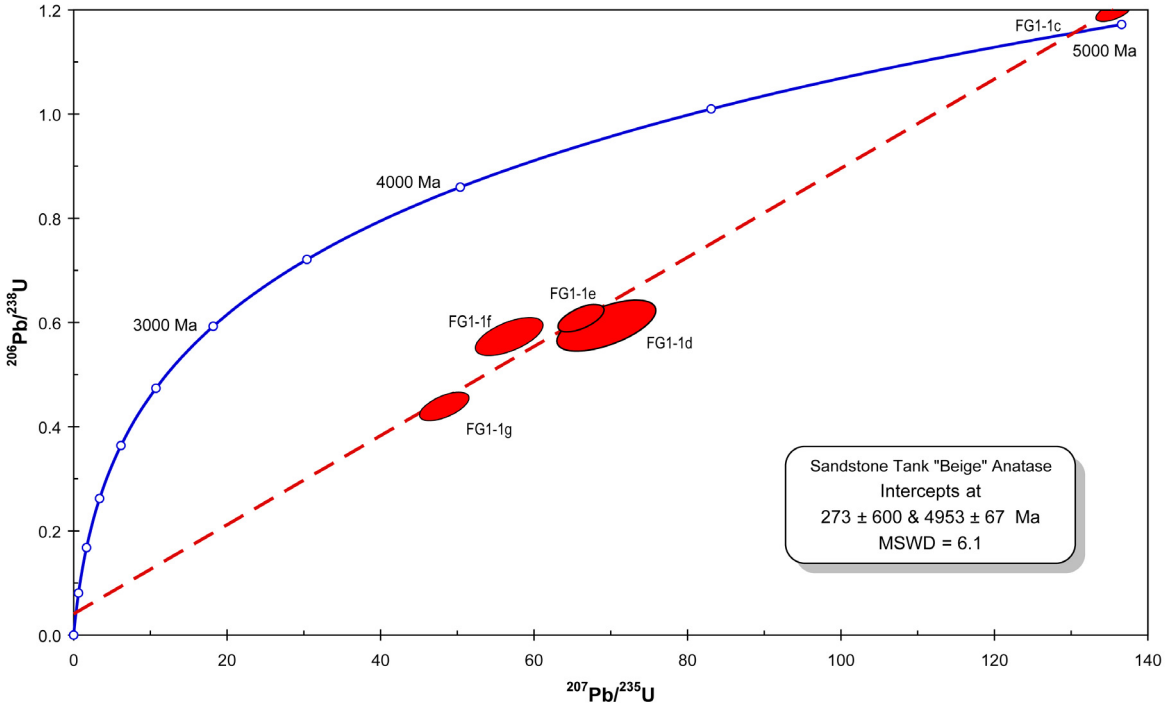

Figure 9. U-Pb Concordia plot showing data from beige (non-iron oxide stained) Sandstone Tank LA-ICP-MS anatase spots (prepared using Isoplot).

DISCUSSION OF LA-ICP-MS RESULTS

The laser ablation results show a systematic correlation between titanium rich morphologies and high U, Th and Pb concentrations. In anatase-rich parts of the sample, especially the geopetal cappings, these three elements are elevated to concentrations of between 10 and 30 ppm.

If a mineral has lost lead, its uranium-lead age will plot below the Concordia curve. Where several such samples plot on a line and this intersects the Concordia curve, the line is called a discordia. The upper intercept is traditionally interpreted as the formation age of the mineral, and the lower intercept the age of the Pb loss event (Williams 1998).

Uranium-lead data from complex geological systems often have an upper intercept of no meaningful age. As uranium and lead are incorporated into a growing crystal, the complex history biases the upper intercept to a spuriously old upper age, which in effect approximates the common lead $^{207}Pb/^{206}Pb$ composition. This has been observed in studies dating titanite by LA-ICP-MS U-Pb methods (Allen *et al.*, 1998; Barnes *et al.*, 2003). The lower intercept is interpreted as containing meaningful age information. In the case of anatase in silcrete, this is thought to represent a crystallisation age, which based on textural information obtained above, should equate to a minimum age cementation, and thus silcrete formation.

Further analysis indicates that there is abundant common lead within anatase. This yields U-Pb ages with high errors, and consequently imprecise isochrons. The 273 ± 600 Ma age for anatase is younger than the youngest bedrock in the area, thought to be Devonian (Beavis & Beavis 1984), and older than the inferred age of the silicified sediments, taken as Eocene based on palaeofloral assemblages. The common lead $^{207}Pb/^{206}Pb$ composition of 0.849 ± 0.058 is older than that for Broken Hill common Pb ($^{207}Pb/^{206}Pb$ = 0.962 – Reynolds (1971)), which is a possible source composition for lead in the system (Figures 7 and 9).

In order to overcome these problems, a more detailed microsampling protocol was established, and analyses were carried out on solutions prepared by total dissolution and spiking techniques on the Neptune multicollector ICP-MS at ANU. This ICP is more precise than the Hewlett Packard, and allows for correction for common Pb by utilising the non-radiogenic ^{204}Pb isotope.

MULTI-COLLECTOR ICP-MS U-PB AND PB-PB SOLUTION ANALYSIS

Micro-sampling was carried out on a geopetal capping from the Sandstone Tank silcrete. A chip (3 cm x 1 cm x 1 cm) was cut from the apex of a geopetal cap draping a quartzite clast. From this chip, seven 3 cm x 1 cm wafers were cut, and from each wafer up to three subsamples, ~0.5 mm x 3 mm were separated using a microsaw. A schematic diagram showing the sampling strategy is shown in Figure 10. The analytical procedure, below, is modified from the procedure of Compston & Oversby (1969).

Each chip was cleaned in 0.2N HCl overnight before being dissolved in a mixture of 1 mL concentrated HF and 0.5 mL concentrated HNO_3 in Teflon bombs at 200^{o}C overnight to dissolve silica and anatase. The solution was then boiled to minimum volume, taken up into solution in 2 mL 6N HNO_3 and another two drops of concentrated HF added to keep the titanium in solution. This mixture was heated to minimum volume again, and placed in a Parr bomb at 200^{o}C overnight in 5 mL 2% HNO_3 and 2 drops of concentrated HF. The final sample solution was brought up to 10 mL with 2% HNO_3 in ICP tubes. From this stock solution, ~5 mL was spiked with ~0.4 g of a thallium spike solution prepared from the SRM 997 standard, which is used to monitor and correct for fractionation of lead isotopes within the ICP-MS. The remaining unspiked solution was kept for unspiked Pb analysis. Spike calibration solutions were prepared by mixing SRM 981 and 997 standard solutions containing 133.6 ppb Pb and 12.48 ppb Tl to produce solutions of differing Pb and Tl concentration, in order to cover the likely range of Pb concentrations encountered in the sample solutions, and account for matrix effects.

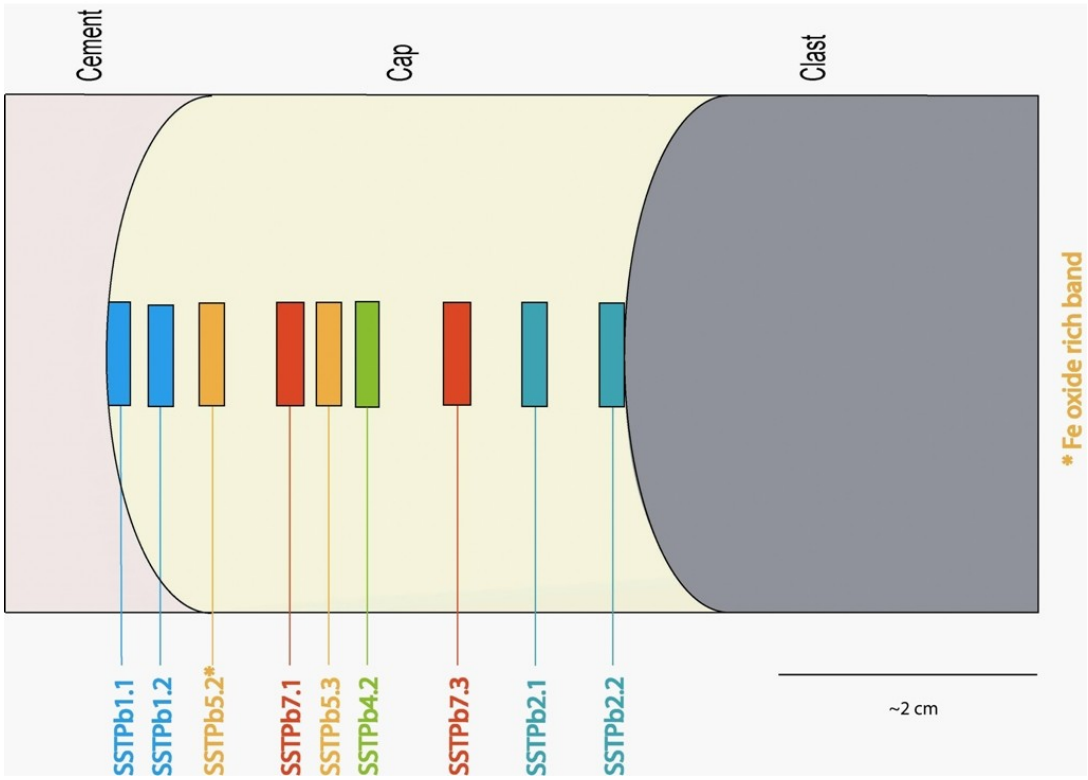

Figure 10. Schematic diagram of a geopetal capping, showing sampling strategy for U- Pb solution MC-ICP-MS (Sandstone Tank sample).

RESULTS

Results of the U-Pb solution work are shown in Tables 2 to 4. These were plotted onto traditional lead isotope diagrams (Figures 11 to 15) in order to evaluate the common lead composition and any age data these might confer.

Lead isotope data (Table 2) shows that lead is present in low concentrations in all samples, ranging from 0.19 – 3.6 ppm, with isotopic ratios suggesting a radiogenic composition, with a high amount of common lead. Uranium concentrations are very low in all samples (Table 3) from 0.1 to 2.3 ppm. Uranium parent-lead daughter ratios are shown in Table 4.

The reduced uranium-lead ratios were used to plot two simple isochron diagrams. The first, the ^{238}U-^{206}Pb isochron diagram plots, the $^{238}U/^{204}Pb$ ratio against the $^{206}Pb/^{204}Pb$ ratio (Figure 11). This diagram yields a ^{238}U-^{206}Pb age of 520 ± 22 Ma, and an initial $^{206}Pb/^{204}Pb$ of 16.58 ± 0.16. A similar diagram can be derived for the ^{235}U-^{207}Pb system (Figure 12). This variant provides age information pertaining to the ^{235}U-^{207}Pb decay scheme, and an initial $^{207}Pb/^{204}Pb$ composition. In this case, the regression yields an isochron age of 846 ± 740 Ma. The large error may be a function of the very low amount of ^{235}U in the samples. In the case of the Sandstone Tank anatase, the initial $^{207}Pb/^{204}Pb$ is 15.46 ± 0.57. A more robust method, by which the initial common Pb $^{207}Pb/^{206}Pb$ ratios can be obtained, uses a Tera-Wasserburg diagram (Tera and Wasserburg, 1972). The Sandstone Tank silcrete data are plotted in this fashion in Figure 13. From this diagram, the $^{207}Pb/^{206}Pb$ of common lead is 0.94 ± 0.1.

Table 2. Uncorrected lead data.

Sample	^{207}Pb (nmol/g)	^{206}Pb (nmol/g)	^{204}Pb (nmol/g)	Pb (ppm)	206/204	± 1σ (%)	207/204	± 1σ (%)
SSTPb1.1	0.751	0.979	0.047	0.758	20.689	0.033	15.872	0.033
SSTPb1.2	1.008	1.299	0.064	1.014	20.413	0.019	15.832	0.019
SSTPb2.1	0.582	0.719	0.037	0.579	19.548	0.040	15.836	0.040
SSTPb2.2	0.542	0.678	0.034	0.540	19.911	0.042	15.903	0.043
SSTPb4.2	0.941	1.202	0.059	0.941	20.337	0.023	15.917	0.022
SSTPb5.2	0.192	0.243	0.012	0.191	20.021	0.129	15.809	0.131
SSTPb5.3	3.621	4.601	0.228	3.605	20.173	0.026	15.876	0.026
SSTPb7.1	0.441	0.660	0.27	0.453	24.271	0.049	16.234	0.049
SSTPb7.3	0.815	1.031	0.051	0.815	20.204	0.028	15.968	0.029

Table 3. Uranium data for solution MC-ICP-MS.

Sample	U ppm	^{238}U ppm	± 1σ (%)	^{235}U ppm	± 1σ (%)
SSTPb1.1	0.556	0.552	0.213	0.004	0.219
SSTPb1.2	0.753	0.748	0.207	0.005	0.210
SSTPb2.1	0.311	0.309	0.203	0.002	0.207
SSTPb2.2	0.323	0.321	0.184	0.002	0.184
SSTPb4.2	0.631	0.626	0.175	0.004	0.168
SSTPb5.2	0.120	0.119	0.225	0.001	0.341
SSTPb5.3	2.339	2.322	0.093	0.017	0.157
SSTPb7.1	0.397	0.394	0.201	0.003	0.218
SSTPb7.3	0.622	0.618	0.229	0.004	0.233

Table 4. Uncorrected uranium-lead data for solution MC-ICP-MS.

Sample	$^{238}U/^{206}Pb$	± 1σ (%)	$^{235}U/^{207}Pb$	± 1σ (%)	$^{238}U/^{204}Pb$	± 1σ (%)	$^{235}U/^{204}Pb$	± 1σ (%)
SSTPb1.1	2.370	0.215	0.022	0.221	49.030	0.215	0.356	0.221
SSTPb1.2	2.418	0.208	0.023	0.211	49.363	0.208	0.358	0.211
SSTPb2.1	1.807	0.207	0.016	0.211	35.329	0.207	0.256	0.211
SSTPb2.2	1.986	0.189	0.018	0.189	39.542	0.189	0.287	0.189
SSTPb4.2	2.187	0.177	0.020	0.169	44.478	0.177	0.323	0.169
SSTPb5.2	2.057	0.259	0.019	0.365	41.182	0.259	0.299	0.365
SSTPb5.3	2.120	0.097	0.020	0.159	42.769	0.097	0.310	0.159
SSTPb7.1	2.510	0.207	0.027	0.224	60.922	0.207	0.442	0.224
SSTPb7.3	2.518	0.231	0.023	0.234	50.880	0.231	0.369	0.234

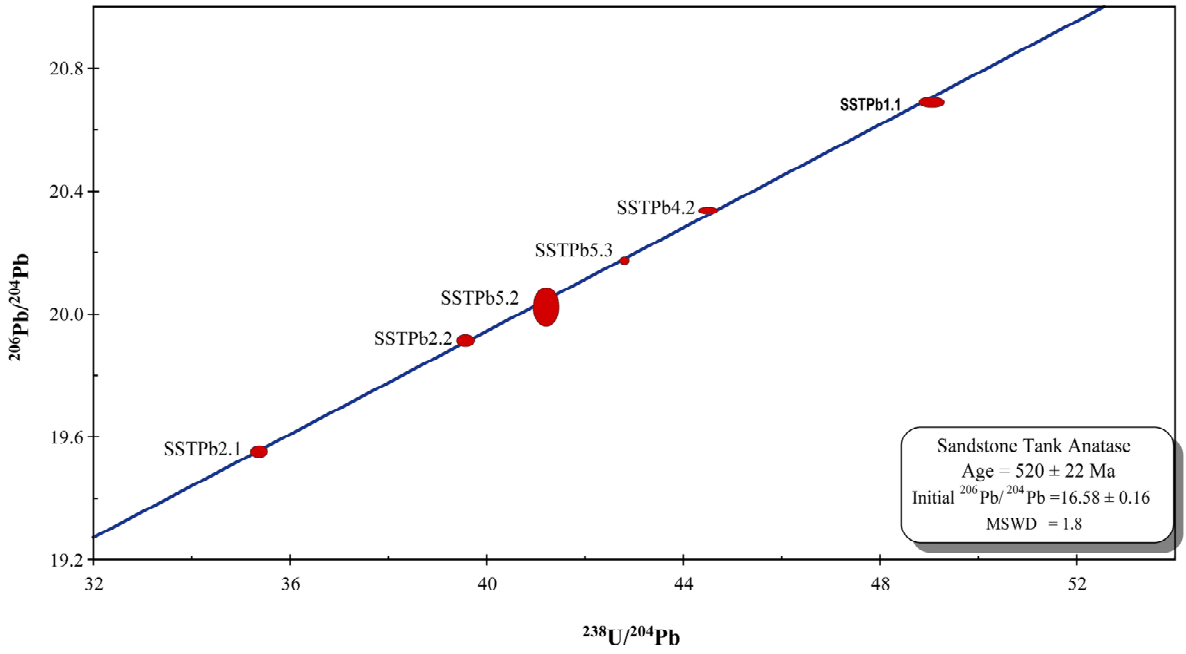

Figure 11. ^{238}U-^{206}Pb isochron diagram.

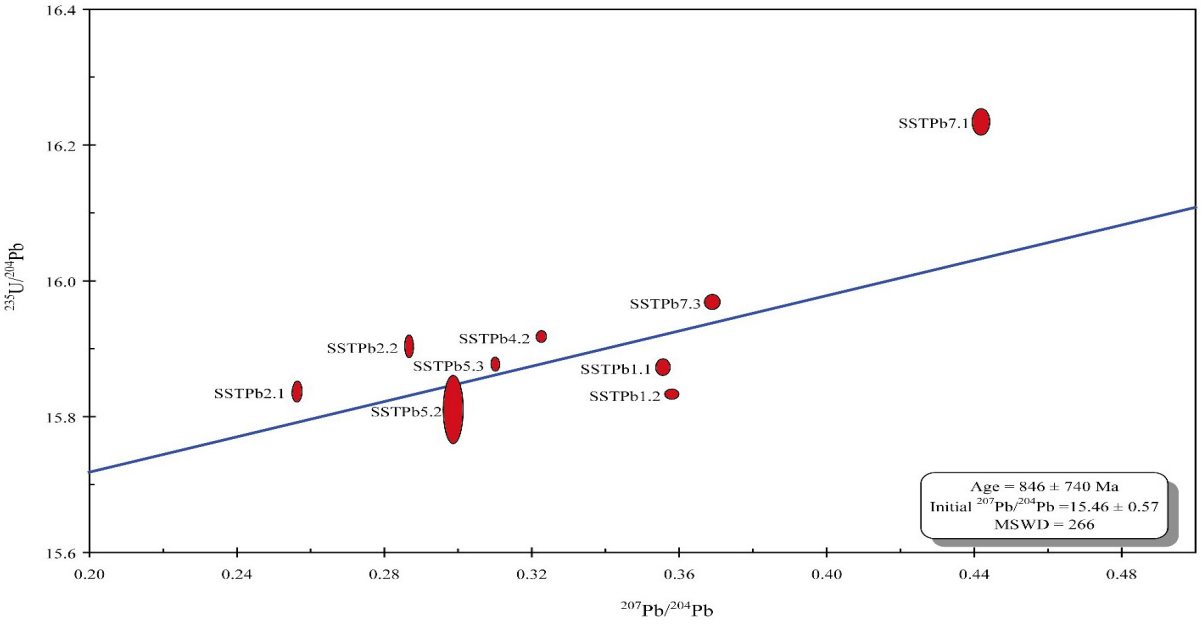

Figure 12. ^{235}U-^{207}Pb isochron diagram.

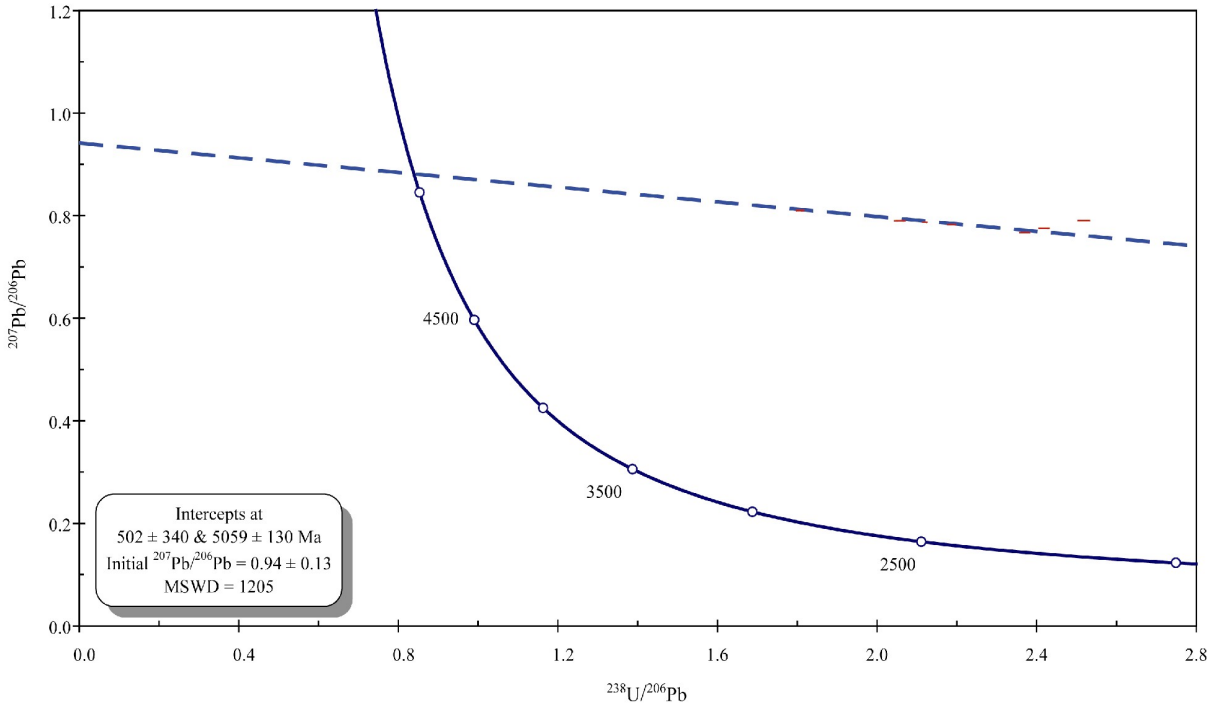

Figure 13. Tera-Wasserburg plot of Sandstone Tank anatase data.

The lead isotope data provide some insight into possible sources and ages of lead within the Sandstone Tank silcrete. The ^{207}Pb-^{206}Pb plot (Figure 14) indicates that the anatase contains some radiogenic component, but is dominated by common Pb. The data clusters around a $^{206}Pb/^{204}Pb$ = 15.9, $^{207}Pb/^{204}Pb$ = 20.2, and is scattered about a line with a slope of 0.074 ± 0.055, which yields an isochron age of 1045 ± 1500 Ma.

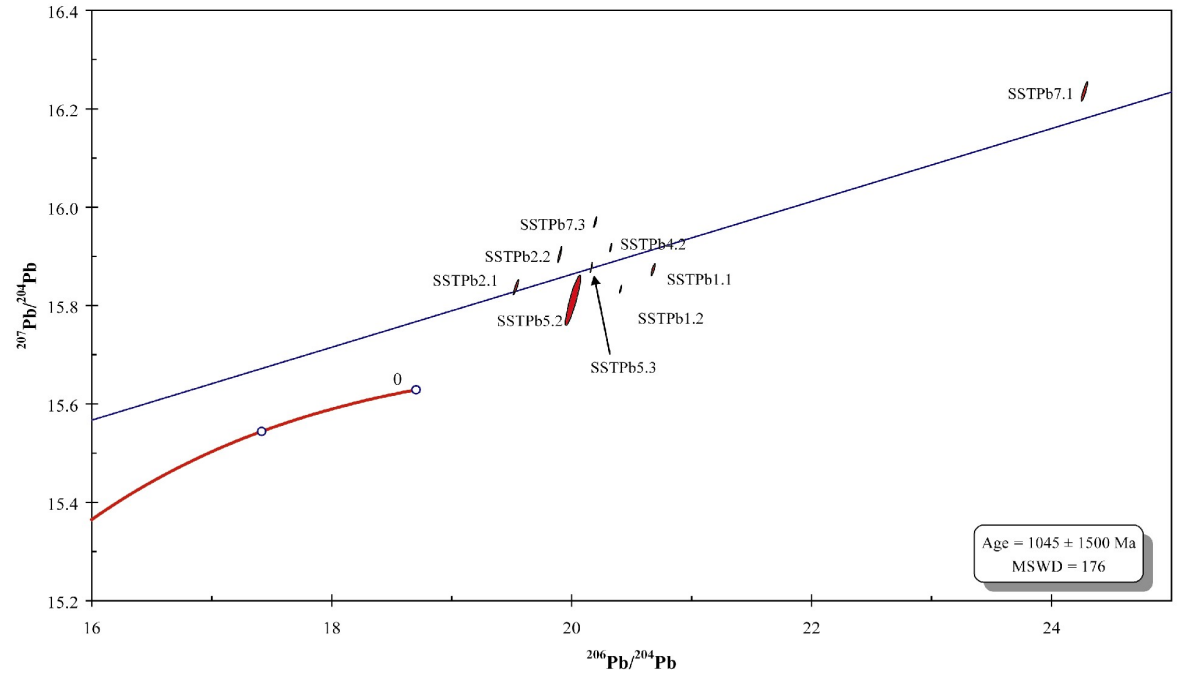

Figure 14. Sandstone Tank silcrete anatase Pb isotope data plotted on a Stacey-Kramers (1975) ^{207}Pb-^{206}Pb plot.

Another way to represent Pb isotope data in order to glean information about the evolution of the Pb system within a sample is via the ^{208}Pb-^{206}Pb plot (Stacey & Kramers, 1975). In the ^{208}Pb-^{206}Pb plot for Sandstone Tank (Figure 15), the results again cluster around a fairly radiogenic composition, given the amount of common Pb in the system. There is no clear trend in the data, and accordingly no isochron has been derived nor any intercept with the calculated Pb growth curve (Stacey & Kramers, 1975).

The common lead component from the Sandstone Tank silcrete anatase can be characterised from the above data. The common lead has a $^{206}Pb/^{204}Pb = 16.59 \pm 0.22$, $^{207}Pb/^{204}Pb = 15.46 \pm 0.57$ and $^{207}Pb/^{206}Pb = 0.94 \pm 0.13$. These values can be used to correct the U-Pb data for the presence of common lead by subtracting the common Pb component from the measured ratios, and deriving radiogenic lead isotope ratios. The radiogenic ratios (Table 5) can be used to obtain ages for the anatase, in a similar fashion to U-Pb dating of zircon (e.g. Williams, 1998).

Common lead corrected radiogenic lead data are listed in Table 5, and a Tera-Wasserburg plot of these data shown in Figure 16. The common lead correction was made by regressing the data on a Tera-Wasserburg diagram (see Figure 12). These data plot above Concordia (see Figure 16), indicating that the correction does not account for all of the common lead. There are three obvious outliers to the data, samples 1.2, 7.1 and 7.3. When these are removed, the data plot on a discordia with a lower intercept age of 513.9 ± 9.8 Ma (Figure 17). The error is reported as the propagated analytical error (1 standard error), and does not include an estimate of error associated with the common lead values.

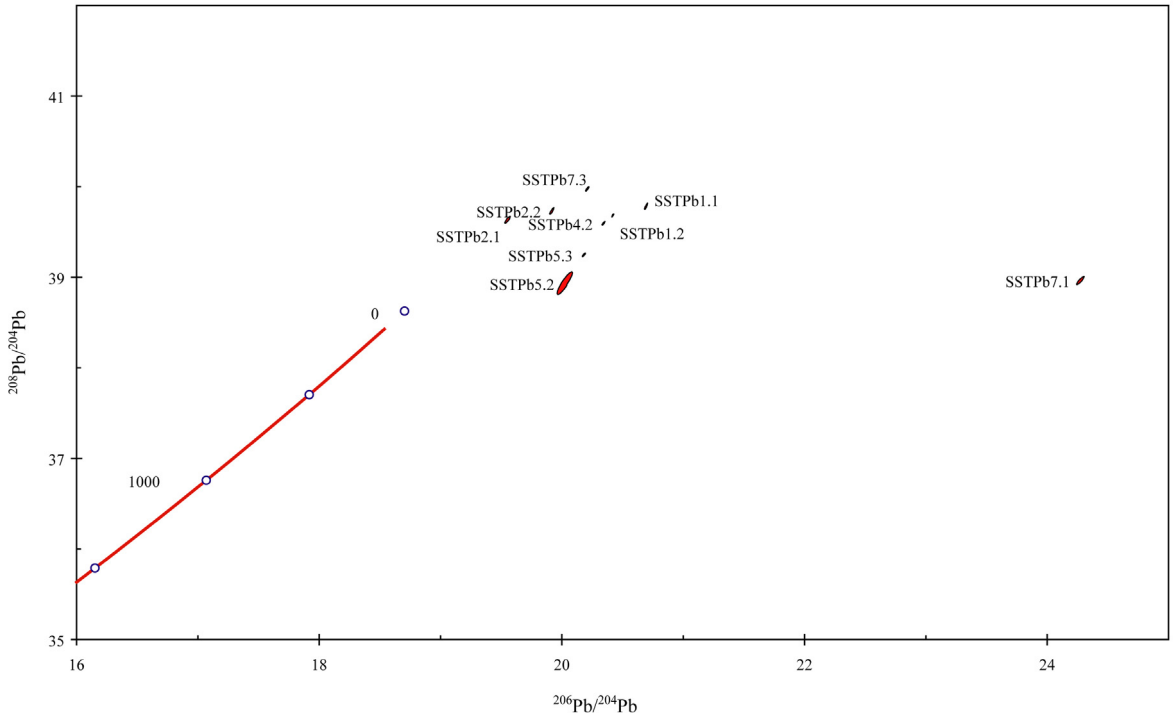

Figure 15. ^{208}Pb-^{206}Pb plot of Sandstone Tank data, with Stacey-Kramers (1975) Pb growth curve.

COMMON LEAD CORRECTION OF U-PB DATA

Table 5. Common lead corrected ratios.

Sample	$^{238}U/^{206}Pb^*$	± 1σ	$^{207}Pb/^{206}Pb^*$	± 1σ	Common Pb composition	
1.1	11.9601	0.0346	0.1004	0.0006	$^{207}Pb/^{206}Pb$	0.94
1.2	12.9111	0.0329	0.0973	0.0004	$^{206}Pb/^{204}Pb$	16.59
2.1	11.9439	0.0459	0.1271	0.0009		
2.2	11.9078	0.0412	0.1333	0.0009		
4.2	11.8702	0.0280	0.1219	0.0004		
5.2	12.0038	0.1019	0.1017	0.0026		
5.3	11.9375	0.0226	0.1162	0.0005		
7.1	7.9316	0.0194	0.1007	0.0006		
7.3	14.0802	0.0431	0.1406	0.0006		

* = radiogenic Pb

As the regression to common lead does not account for all of the observed discordance, data were iteratively corrected until they fell on or near Concordia. This was achieved with common Pb values of $^{207}Pb/^{206}Pb$ = 0.0593 and $^{206}Pb/^{204}Pb$ = 16.86, with errors of ~7.7% on the common lead ratios. The corrected ratios are presented in Table 6, and plotted in Figure 18.

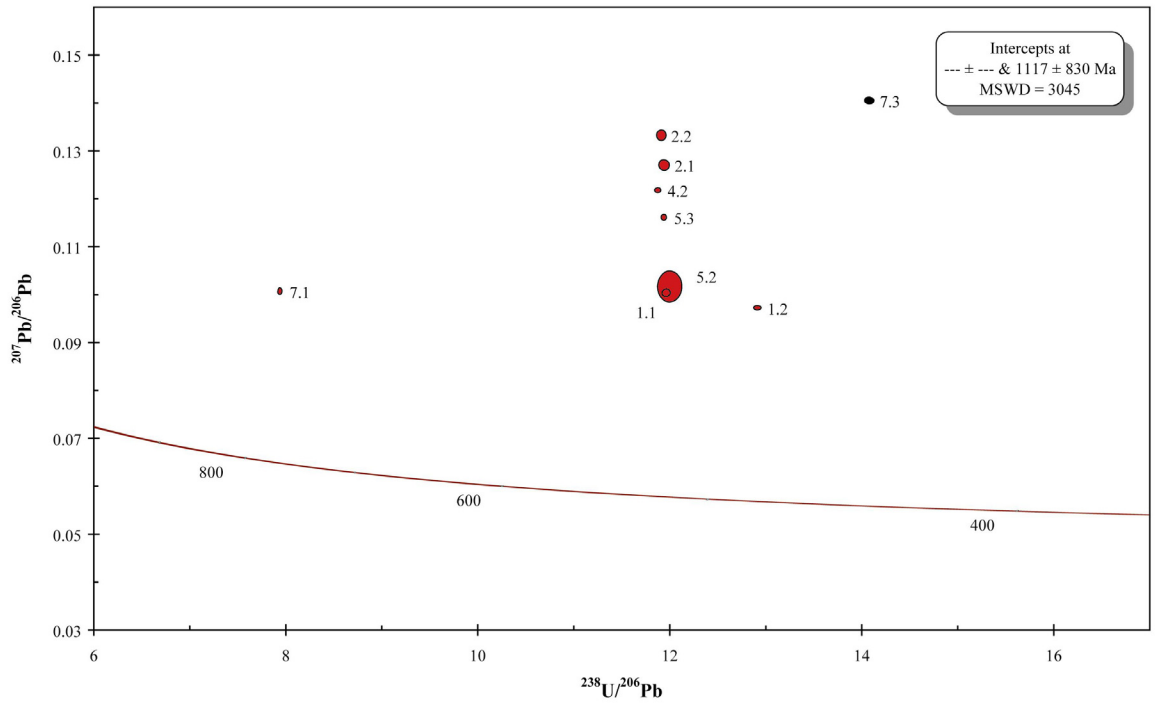

Figure 16. Tera-Wasserburg plot of common lead-corrected data from Sandstone Tank.

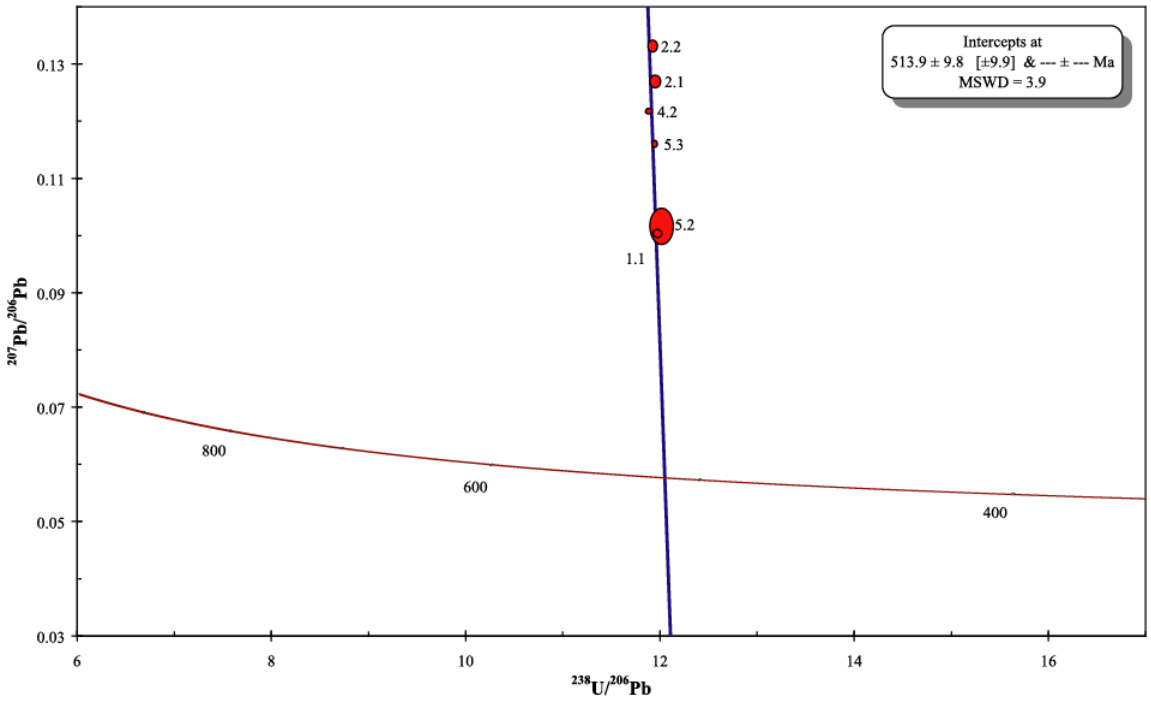

Figure 17. Tera-Wasserburg plot of common lead-corrected data from Sandstone Tank anatase, no outliers.

Table 6. Iterative common lead corrected ratios.

Sample	$^{238}U/^{206}Pb^*$	± 1σ	$^{207}Pb/^{206}Pb^*$	± 1σ	Common Pb Composition	
1.1	12.8147	0.0346	0.0493	0.0006	$^{207}Pb/^{206}Pb$	0.0593
1.2	13.9055	0.0329	0.0419	0.0004	$^{206}Pb/^{204}Pb$	16.86
2.1	13.1603	0.0459	0.0570	0.0009		
2.2	12.9762	0.0412	0.0721	0.0009		
4.2	12.8045	0.0280	0.0673	0.0004		
5.2	13.0433	0.1019	0.0399	0.0026		
5.3	12.9237	0.0226	0.0584	0.0005		
7.1	8.2244	0.0194	0.0744	0.0006		
7.3	15.2328	0.0431	0.0853	0.0006		

* = radiogenic Pb

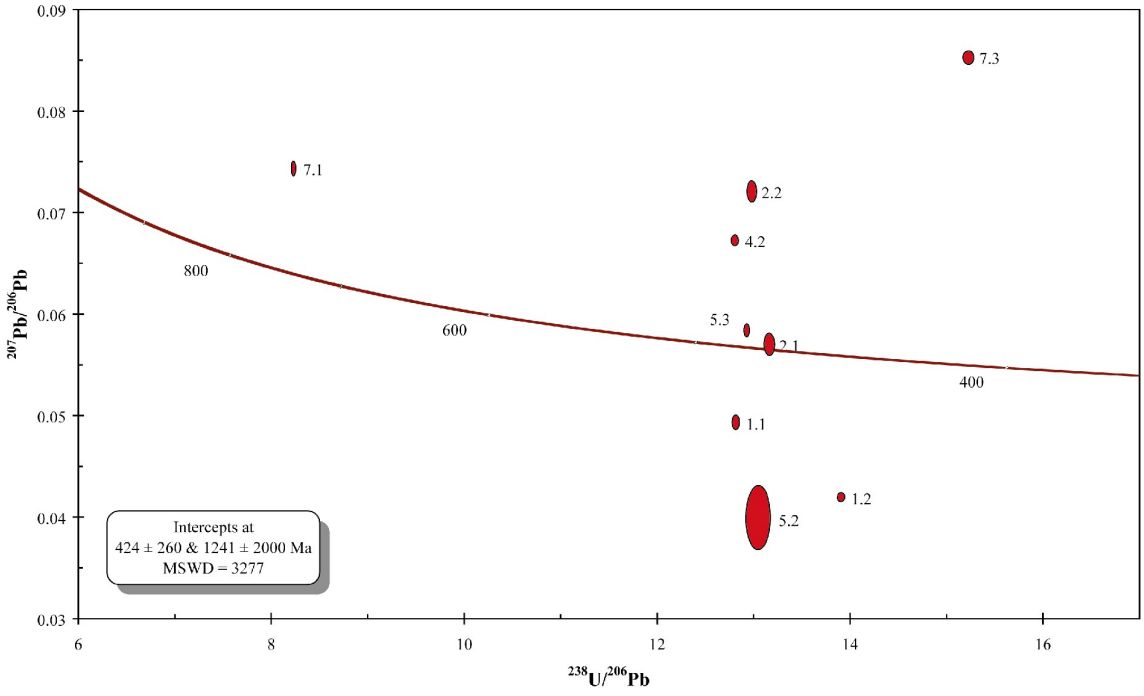

Figure 18. Iterative common lead corrected Sandstone Tank anatase data.

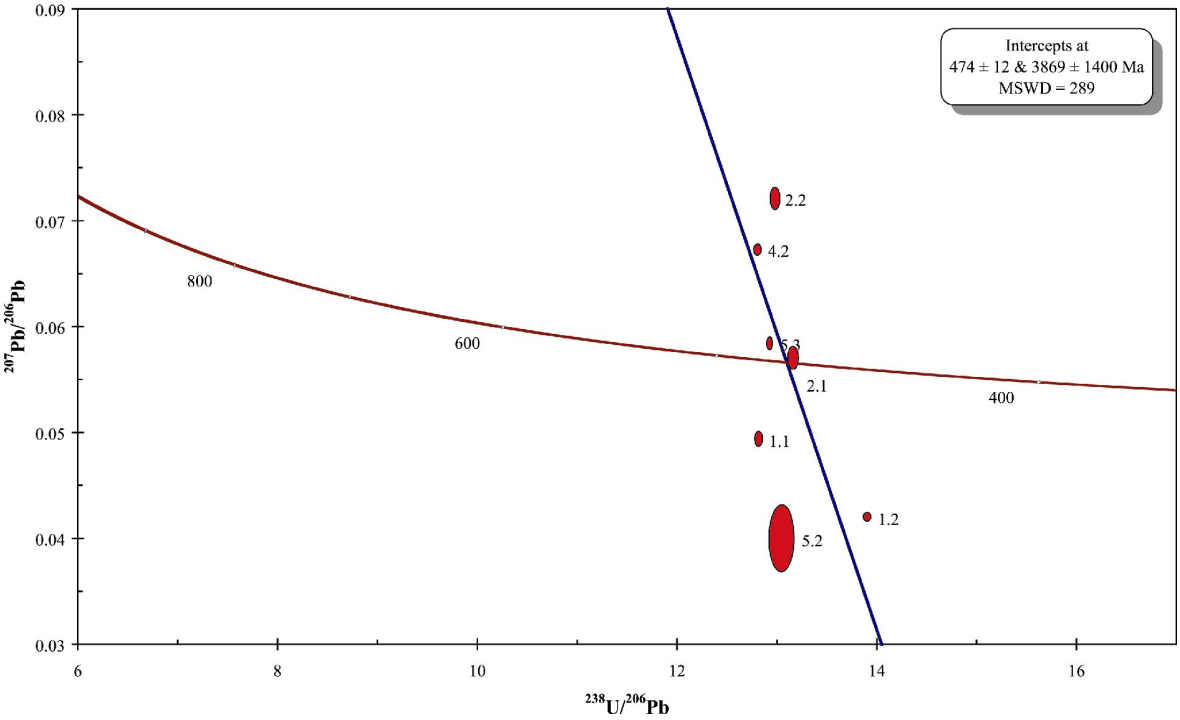

Figure 19. Outlier deleted, iterative common lead corrected Tera-Wasserburg U-Pb plot of Sandstone Tank anatase MC-ICP-MS data**.**

Figure 18 indicates the presence of two outliers after common lead correction, again, Samples 7.1 and 7.3. These two samples contain small amounts of iron oxides, which are susceptible to uptake or loss of both uranium and lead. Once these two outliers are removed, the data (Figure 19) plots on Concordia, with an age of 474 ± 12 Ma. Again, the error reported is only the propagated analytical uncertainty, with no accounting for errors in the estimate of common lead composition, which is roughly 7.7%.

DISCUSSION

The data and refined results presented in the previous sections show that anatase contains uranium and lead in measurable concentrations, high enough for dating. The significance of any age determined is, however, uncertain. In this study, the various U-Pb age estimates obtained vary greatly, and in most cases have large associated errors. The initial measurements using laser ablation gave ages of ~270 Ma, with errors of ± 300 – 600 Ma. These ages were not corrected for common lead, or for possible anatase related fractionation of U or Pb during laser sampling, and the data implied that a large proportion of the lead in anatase was common lead, as shown in Figures 6.11 and 6.14. The common lead composition obtained from the solution data, using ^{238}U-^{206}Pb, ^{235}U-^{207}Pb and Tera-Wasserburg diagrams indicated a single-stage Stacey-Kramers common lead age of ~1.8 Ga, on a Pb evolution curve with an initial ^{238}U/^{204}Pb = 10.26.

Willyama group rocks provide a possible source for lead at Sandstone Tank, as is the Broken Hill orebody itself which lies ~100 km to the south of Sandstone Tank. The Sandstone Tank silcrete represents a silicified palaeochannel that drained from the south to the north (Hill and Roach, 2003). Broken Hill common lead has a Stacey-Kramers single-stage lead age of 1690 Ma, and a composition

of $^{206}Pb/^{204}Pb$ = 16, $^{207}Pb/^{206}Pb$ = 0.9618 (Reynolds, 1971). This is significantly different from the Sandstone Tank calculated common lead composition, which is taken to be $^{206}Pb/^{204}Pb$ = 16.86 and $^{207}Pb/^{206}Pb$ = 0.0593 this indicates that Broken Hill lead is not the source of common lead, assuming a single, unmixed source.

The solution MC-ICP-MS ages do not fit with the existing model for the formation of the Sandstone Tank silcrete. The anatase within the silcrete appears to be a late-stage cementing agent, or matrix material. The cemented sediment that contains Eocene rainforest flora, giving an approximate age for the silcrete formation (Greenwood *et al.*, 1997). The clasts within the pseudobreccia horizon of the silcrete are Adelaidean quartzites (Hill and Roach, 2003), with the anatase sampled forming geopetal drapes over the clasts. If the anatase was precipitated from solution during silcrete formation, the U-Pb ages should represent the closure of the U-Pb system at that time, and fall between 56 and 34 Ma. If the chemical components of the anatase are sourced unchanged from the sediments (i.e. directly from detrital rutile), they could retain any age back to that of the quartzite clasts or older, which are between ~550 and 600 Ma. The best estimate U-Pb age of 474 ± 12 Ma does not equate to either the quartzite age, or the inferred age of silcrete formation. Alternatively, other events in the region that may explain this age must be examined. The Delamarian Orogeny occurred at approximately 520 Ma, and may have provided a pulse of activity that is recorded in rocks in western NSW (Hill and Kohn, 1999). This is the only regional event recorded at this time in western NSW, but it is also too old to account for the U-Pb age of the anatase. Another explanation for the age yielded by MC-ICP-MS is that the anatase inherited the parent U and Pb composition, but only partially. The consequent ingrowth of Pb would yield an age younger than that of the parent material, but much older than the age of the anatase crystallisation.

Rutile, of which anatase is a low temperature polymorph, has been successfully dated using U-Pb methods (e.g. Mezger *et al.*, 1989; Mezger *et al.*, 1991). Although there are no reported studies dating anatase in a similar fashion, the crystal structure is similar, and thus should share U-Pb systematics with rutile. However, the very small crystal size, and the mobility of uranium in the weathering environment, may have rendered the Sandstone Tank anatase unsuitable for dating due to Pb loss associated with recoil during U decay. Adding to this, the resolution of the micro-sampling methods utilised results in incorporation of materials such as silica cement, and possibly detrital rutile and zircon grains, which will contaminate the U-Pb results. In the case of detrital grain contamination, particularly zircon, this may give erroneous mixing ages.

REFERENCES

ALEXANDRE A., MEUNIER J.-D., LLORENS E., HILL S.M. & SAVIN S.M. 2004. Methodological improvements for investigating silcrete formation: petrography, FT-IR and oxygen isotope ratio of silcrete quartz cement, Lake Eyre Basin (Australia). *Chemical Geology* **211**(3-4): 261-274.

ALLEN C.M., WILLIAMS I.S., STEPHENS C.J. & FIELDING, C.R. 1998. Granite genesis and basin formation in an extensional setting: the magmatic history of the northernmost New England Orogen. *Australian Journal of Earth Sciences* **45**(6): 875-888.

ALLEY N.F. 1977. Age and origin of laterite and silcrete duricrusts and their relationship to episodic tectonism in the mid-north of South Australia. *Journal of the Geological Society of Australia* **24**(2): 107-116.

BARNES C.G., PRESTVIK T., BARNES M.A.W., ANTHONY E.Y. & ALLEN C.M. 2003. Geology of a magma transfer zone: the Hortavaer Igneous Complex, north-central Norway. *Norwegian Journal of Geology* **83**: 187-208.

COMPSTON W. & OVERSBY V. 1969. Lead Isotopic analysis using a double spike. *Journal of Geophysical Research* **74**; 4338-4348

CORFU F. & MUIR T.L. 1989. The Hemlo-Heron Bay greenstone belt and Hemlo Au-Mo deposit, Superior Province, Ontario, Canada; 2, Timing of metamorphism, alteration and Au mineralization from titanite, rutile, and monazite U-Pb geochronology. *Chemical Geology; Isotope Geoscience Section* **79**(3): 201-223.

EGGLETON R.A. 2001. *The Regolith Glossary: Surficial Geology, Soils and Landscapes*. Floreat Park, WA, CRC LEME.pp 144.

EXON N.F., LANGFORD-SMITH T. & McDOUGALL I. 1970. The age and geomorphic correlations of deep-weathering profiles, silcrete, and basalt in the Roma-Amby region, Queensland. *Journal of the Geological Society of Australia* **17**(1): 21-30.

FRAKES, L.A., BURGER, D., APTHORPE, M., WISEMAN, J., DETTMANN, M., ALLEY, N., FLINT, R., GRAVESTOCK, D., LUDBROOK, N., BACKHOUSE, J., SKWARKO, S., SCHEIBNEROVA, V., MCMINN, A., MOORE, P.S., BOLTON, B.R., DOUGLAS, J.G., CHRIST, R., WADE, M., MOLNAR, R.E., McGOWRAN, B., BALME, B.E. & DAY, R.A., 1987. Australian Cretaceous shorelines, stage by stage. *Palaeogeography, Palaeoclimatology, Palaeoecology* **59**: 31-48.

GREENWOOD D.R., ROWLETT A.I., ALLEY N.F. & HILL S.M. 1997. Palaeobotanical evidence for the initiation of the drying of the Australian interior. *Quaternary Deserts and Climate Change Program and Abstracts ICGP 139*. Price, D. and Nanson, G. (*eds*). Wollongong, University of Wollongong, School of Geosciences**:** unpaginated.

HILL S.M. 2000. The Regolith and Landscape Evolution of the Broken Hill Block, Western New South Wales, Australia. (PhD), CRC LEME, Department of Geology, The Australian National University.

HILL S.M. & ROACH I.C. 2003. The regolith-landforms of sandstone paddock, Fowlers Gap, western NSW. *Advances in Regolith*. Roach, I. C. (*ed*), CRC LEME**:** 193 - 200.

HILL S.M. & KOHN B.P. 1999. Morphotectonic evolution of the Mundi Mundi range front, Broken Hill, western NSW. Regolith '98. Australian Regolith and Mineral Exploration: new approaches to an old continent, Kalgoorlie, WA, CRC LEME.

LAMPLUGH G.W. 1902. "Calcrete." *Geological Magazine* **9**: 75.

LUDWIG K.R. & PACES J.B. 2002. Uranium-series dating of pedogenic silica and carbonate, Crater Flat, Nevada. *Geochimica et Cosmochimica Acta* **66**(3): 487-506.

MEZGER K., HANSON G.N. & BOHLEN S.R. 1989. High-precision U-Pb ages of metamorphic rutile; application to the cooling history of high-grade terranes. *Earth & Planetary Science Letters* **96**(1-2): 106-118.

MEZGER K., RAWNSLEY C.M., BOHLEN S.R. & HANSON G.N. 1991. U-Pb garnet, sphene, monazite, and rutile ages; implications for the duration of high-grade metamorphism and cooling histories, Adirondack Mts., New York. *Journal of Geology* **99**(3): 415-428.

MILNES A.R. & HUTTON J.T. 1974. The Nature of Microcryptocrystalline Titania in 'Silcrete' Skins from the Beda Hill Area of South Australia. *Search* **5**(4): 153-154.

MILNES A.R. & THIRY M. 1992. Silcretes. *Weathering, soils & Paleosols*. Martini, I. P. and Chesworth, W. (*eds*). Amsterdam-Oxford-New York-Tokyo, Netherlands, Elsevier. **2:** 349-377.

MILNES A.R., THIRY M. & WRIGHT M.J. 1991. Silica accumulations in saprolites and soils in South Australia. Occurrence, characteristics, and genesis of carbonate, gypsum, and silica accumulations in soils. Nettleton, W. D. (*eds*). Madison, WI, United States, *Soil Science Society of America*. **26:** 121-149.

NEYMARK L.A. & PACES J.B. 2000. Consequences of slow growth for ^{230}Th/U dating of Quaternary opals, Yucca Mountain, NV, USA. *Chemical Geology* **164**(1-2): 143-160.

NEYMARK L.A., AMELIN V.Y. & PACES J.B. 2000. "^{206}Pb-^{230}Th-^{234}U-^{238}U and ^{207}Pb-^{235}U geochronology of Quaternary opal, Yucca Mountain, Nevada." *Geochimica et Cosmochimica Acta* **64**(17): 2913-2928.

NEYMARK L.A., AMELIN Y., PACES J.B. & PETERMAN Z.E. 2002. U-Pb ages of secondary silica at Yucca Mountain, Nevada: implications for the paleohydrology of the unsaturated zone. *Applied Geochemistry* **17**(6): 709-734.

O'SULLIVAN P.B., GIBSON D.L., KOHN B.P., PILLANS B. & PAIN C.F. 2000. Long-term landscape evolution of the Northparkes region of the Lachlan Fold Belt, Australia: constraints from fission track and paleomagnetic data. *Journal of Geology* **108**: 1-16.

OLLIER C.D. 1991. "Aspects of silcrete formation in Australia." *Zeitschrift fur Geomorphologie* **35**(2): 151-163.

PACES J.B., NEYMARK L.A., WOODEN J.L. & PERSING H.M. 2004. Improved spatial resolution for U-series dating of opal at Yucca Mountain, Nevada, USA, using ion-microprobe and microdigestion methods. *Geochimica et Cosmochimica Acta* **68**(7): 1591-1606.

PILLANS B., TONUI E. & IDNURM M. 1999. Paleomagnetic dating of weathered regolith at Northparkes Mine, NSW. *Regolith '98: New Approaches to an Old Continent, Proceedings of the 3rd Australian Regolith Conference*. Taylor, G. and Pain, C. (*eds*). Perth, CRC LEME**:** 237-242.

RADTKE U. & BRUECKNER H. 1991. Investigation on age and genesis of silcretes in Queensland (Australia); preliminary results. *Earth Surface Processes and Landforms* **16**(6): 547 - 554.

REYNOLDS P.H. 1971. "A U - Th - Pb lead isotope study of rocks and ores from Broken Hill, Australia." *Earth and Planetary Science Letters* **12**(2): 215-223.

RICHARDS J.P., KROGH T. E. & SPOONER E.T.C. 1988. Fluid inclusion characteristics and U-Pb rutile age of late hydrothermal alteration and veining at the Musoshi stratiform copper deposit, Central African copper belt, Zaire. *Economic Geology* **83**(1): 118-139.

SCHAERER U., KROGH T.E. & GOWER C.F. 1986. Age and evolution of the Grenville Province in eastern Labrador from U-Pb systematics in accessory minerals. *Contributions to Mineralogy and Petrology* **94**(4): 438-451.

SMITH M.L. 2006. Towards a Geochronology for Long-term Landscape Evolution of Northwestern New South Wales. (PhD), CRC LEME, RSES, ANU.

SMITH R.E. 1996. Regolith research in support of mineral exploration in Australia. *Journal of Geochemical Exploration* **57**: 159-173.

SPRY M.J. 2003. The Regolith and Landscape Evolution of a Low Relief Landscape: Cobar, Central New South Wales, Australia. (PhD), CRC LEME Division of Health, Design & Science, University of Canberra.

STACEY J.S. & KRAMERS J.D. 1975. Approximation of terrestrial lead isotope evolution by a two-stage model. *Earth & Planetary Science Letters* **26**(2): 207-221.

STEIGER R.H. & JAGER E. 1977. Subcommission on geochronology: Convention on the use of decay constants in geo- and cosmochronology. *Earth & Planetary Science Letters* **36**(3): 359-362.

TAYLOR G. & SMITH I.E. 1975. The genesis of sub-basaltic silcretes from the Monaro, New South Wales. *Journal of the Geological Society of Australia* **22**: 377-385.

TERA F. & WASSERBURG G.J. 1972. U-Th-Pb systematics in lunar highland samples from the Luna 20 and Apollo 16 missions. *Earth & Planetary Science Letters* **17**(1): 36.

THIRY M. & MILNES A.R. 1991. Pedogenic and groundwater silcretes at Stuart Creek opal field, South Australia. *Journal of Sedimentary Petrology* **61**(1): 111-127.

THIRY M. & SIMON-COINCON R. Eds. (1999). *Palaeoweathering, palaeosurfaces and related continental deposits*. Special Publication of the International Association of Sediementologists. Carlton, Victoria, Blackwell Science.

TWIDALE C.R. 1983. Australian laterites and silcretes; ages and significance. *Revue de Geologie Dynamique et de Geographie Physique* **24**(1): 35 - 45.

WATTS S.H. 1978. A petrographic study of silcrete from inland Australia. Journal of *Sedimentary Petrology* **48**(3): 987-994.

WEBB J.A. & GOLDING S.D. 1998. Geochemical mass-balance and oxygen-isotope constraints on silcrete formation and its paleoclimatic implications in southern Australia. *Journal of Sedimentary Research* **68**(5): 981-993.

WELLMAN P. & McDOUGALL I. 1974. Potassium - argon ages on the Cainozoic volcanic rocks of New South Wales. *Journal of the Geological Society of Australia* **21**(3): 247-272.

WILLIAMS I.S. 1998. U-Th-Pb geochronology by ion microprobe. Applications of Microanalytical Techniques to Understanding Mineralizing Processes. *In*: McKibben, M. A., Shanks III, W. C. and Ridley, W. I. (*eds*). Boulder, Society of Economic Geologists, inc. **7:** 1-35.

WOPFNER H., CALLEN R. & HARRIS W.K. 1974. The Lower Tertiary Eyre formation of the southwestern Great Artesian Basin. *Journal of the Geological Society of Australia* **21**(1): 17 - 51.

WOPFNER H. 1974. Post-Eocene history and stratigraphy of northeastern South Austalia. *Transactions of the Royal Society of South Australia* **98**(1): 1-12.

WOPFNER H. 1978. Silcretes of northern South Australia and adjacent regions. *Silcrete in Australia.* Langford-Smith, T. (*eds*). Armidale, Department of Geography, University of New England**:** 93-142.

YOUNG R.W. & McDOUGALL I. 1982. Basalts and silcretes on the coast near Ulladulla, southern New South Wales. *Journal of the Geological Society of Australia* **29**: 425-430.

APPENDIX. ANAYTICAL DATA FOR RANGER URANIUM MINE

Activity ratios for microcrystalline iron/oxyhydroxides from Ranger uranium mine. Numbers in *italic-bold* were calculated using the maximum likelihood procedure (Ludwig & Titterington 1994) [$^{238}U/^{232}Th$] is the median for the corresponding sample. Apparent ages calculated using Eq 1. [$^{234}U/^{238}U/]_o$ initial activity ratio calculated with $[^{234}U/^{238}U]_0=[^{234}U/^{238}U]\cdot e^{(\lambda\cdot(234)\cdot t)}$, t = Apparent age, ∞ = age upper limit exceeds U-series dating upper limit. MSWD = Mean Square of Weighted Deviates. NA = Not calculated because of ∞ or Not Applicable. (N) = number of sampling sites (drill holes) included in estimation of activity ratios. All errors are 2-σ.

Profile NW	$[^{230}Th/^{238}U]$	$[^{234}U/^{238}U]$	$[^{238}U/^{232}Th]$	Apparent Age (kyr)	$[^{234}U/^{238}U]_0$	MSWD	Prob. fit (N)
NW04a	***1.14± 0.3***	***1.01±0.14***	***16.3± 1.7***	***NA***	***NA***	***8.8***	***0(7)***
NW04b	***0.43±0.2***	***1.29±0.27***	***15.0± 2***	***43+41/-23***	***1.3±0.3***	***1.7***	***0.1(6)***
NW 14	***0.95± 0.2***	***1.03± 0.09***	***19±5***	***272+∞/-130***	***1.058± 0.3***	***4.6***	***0.07(7)***
NW 28	0.881±0.052	1.008± 0.012	134± 21	224+27/-20	1.016± 0.014	--	(14)
NW 36	0.879± 0.01	1.031± 0.01	59± 20	203+14/-12	1.016± 0.024	--	(9)
NW 47	0.712± 0.024	1.026± 0.012	562± 150	127.8+11/-10	1.037± 0.011	--	(6)

Profile G	$[^{230}Th/^{238}U]$	$[^{234}U/^{238}U]$	$[^{238}U/^{232}Th]$	Apparent Age (kyr)	$[^{234}U/^{238}U]_0$	MSWD	Prob. Fit (N)
G 11	***0.7±0.45***	***0.9± 0.2***	***8.0± 0.5***	***134+∞/90***	***0.99±0.3***	***1.4***	***0.22(4)***
G 09	***0.797± 0.088***	***1.19± 0.05***	***48.6± 11***	***114±20***	***1.27± 0.16***	***0.84***	***0.57(6)***
G 08	0.875± 0.14	1.04± 0.12	186± 56	195+∞/-70	1.07± 0.19	--	(5)
G 06	***0.9± 0.2***	***1.07± 0.08***	***10.3± 5***	***190+∞/-81***	***1.13± 0.13***	***0.5***	***0.7(4)***
G 05	0.988± 0.02	1.12± 0.03	460± 350	210±22	1.17± 0.14	--	(5)

Profile BS	$[^{230}Th/^{238}U]$	$[^{234}U/^{238}U]$	$[^{238}U/^{232}Th]$	Apparent Age (kyr)	$[^{234}U/^{238}U]_0$	MSWD	Prob. fit (N)
C+60(b)	1.05± 0.26	1.103± 0.065	40± 90	282+∞/-145	1.23± 0.22	22	0(4)
1AB-5	0.87± 0.02	0.992± 0.010	77± 8	241+31/-23	0.98± 0.04	--	(11)
2B-5	0.807± 0.069	1.042± 0.032	165± 8	159 +40/-27	1.07 ± 0.05	--	(7)
3A-0	0.884± 0.063	1.001± 0.042	630± 50	233 +148/-54	1.00± 0.08	--	(7)
4A-3	0.869± 0.02	1.019± 0.014	238 ± 75	205 +19/-16	1.03± 0.02	--	(6)
5B1	0.842± 0.016	1.016± 0.01	242± 150	190 +12/-11	1.03± 0.02	--	(10)

Summary of U-series results for the analysed pisoliths. Rows in bold are from goethitic cutans, others are core material or hematitic cutans. $^{238}U^*$ are apparent U concentrations and it is not used for calculation of activity ratios Distances from core represent the median distance between the laser-ablation track and the nearest edge of the core. Total rind thickness is presented below the data for the corresponding specimen.

Pisolith (band)	Distance from core (mm)	$^{238}U^*$ (ppm)	$^{230}Th/^{238}U$	$^{234}U/^{238}U$	$^{238}U/^{232}Th$	$^{230}Th/^{232}Th$	Apparent age (ky)
P1(B1)	6.08	38.5	0.796 ± 0.016	0.957 ± 0.008	212 ± 5	169 ± 6	200 +15/13
P1(B2)	5.74	62.0	0.704 ± 0.012	0.933 ± 0.004	283 ± 13	199 ± 10	158 +7.5/-6.4
P1(B3)	**5.44**	**56.9**	**0.675 ± 0.007**	**0.933 ± 0.005**	**367 ± 26**	**248 ± 18**	**143.5 +4.5/4.1**
P1(B4)	**4.4**	**49.1**	**0.763 ± 0.006**	**0.983 ± 0.005**	**111 ± 7**	**85 ± 5**	**164.3 +5/-4.6**
P1(B5)	4.03	49.1	0.876 ± 0.006	0.998 ± 0.009	390 ± 15	341 ± 14	229 +133/-11
P1(B6)	3.63	43.4	0.812 ± 0.010	0.969 ± 0.005	758 ± 15	616 ± 14	203 +10/-8.8
P1(B7)	2.77	33.5	0.837 ± 0.023	0.978 ± 0.008	322 ± 13	270 ± 13	214 +23/-19
P1(B8)	**1.99**	**47.6**	**0.870 ± 0.014**	**1.046 ± 0.004**	**85 ± 2**	**74 ± 2**	**189 +9.2/-8.4**
P1(B9)	**0.86**	**28.5**	**0.871 ± 0.007**	**1.025 ± 0.006**	**253 ± 5**	**221 ± 5**	**203 +8.5/-7.6**
P1(core)		8.5	0.916 ± 0.007	1.064 ± 0.019	283 ± 13	259 ± 12	205 +16/-13

Rind thickness: 6.9 mm

Pisolith (band)	Distance from core (mm)	^{238}U* (ppm)	$^{230}Th/^{238}U$	$^{234}U/^{238}U$	$^{238}U/^{232}Th$	$^{230}Th/^{232}Th$	Apparent age (ky)
P2(B1)	2.57	138.8	0.729 ± 0.006	0.966 ± 0.004	88.0 ± 1.8	64 ± 1	155 +4.2/-3.8
P2(B2)	**2.37**	**107.4**	**0.662 ± 0.006**	**0.980 ± 0.004**	**78.8 ± 9.4**	**52 ± 6**	**122.9 +3/-2.7**
P2(B3)	2.12	110.1	0.746 ± 0.010	1.004 ± 0.004	49.4 ± 2.8	37 ± 2	147 +5/-4.5
P2(B4)	**1.82**	**90.2**	**0.705 ± 0.011**	**0.965 ± 0.004**	**171.6 ± 5.5**	**121 ± 4**	**144 +5.5/-5.2**
P2(B5)	1.37	92.3	0.807 ± 0.008	1.007 ± 0.008	51.6 ± 3.7	42 ± 3	175 +7/-6.3
P2(B6)	**0.97**	**94.5**	**0.807 ± 0.012**	**1.021 ± 0.008**	**71.2 ± 2.0**	**57 ± 2**	**168 +8/-7**
P2(B7)	0.66	73.1	0.762 ± 0.011	0.990 ± 0.008	234.4 ± 16.6	179 ± 13	161 +7.3/-6.8
P2(core)	(3.32)	18.4	0.831 ± 0.007	1.049 ± 0.003	54.6 ± 2.4	45 ± 2	166 5/-4.6

Rind thickness: 3.32 mm

Pisolith (band)	Distance from core (mm)	^{238}U* (ppm)	$^{230}Th/^{238}U$	$^{234}U/^{238}U$	$^{238}U/^{232}Th$	$^{230}Th/^{232}Th$	Apparent age (ky)
P3(B1)	**2.01**	**34.2**	**0.345 ± 0.014**	**0.778 ± 0.005**	**102.5 ± 4.8**	**35 ± 2**	**66 +4/3**
P3(B2)	**1.67**	**67.7**	**0.423 ± 0.009**	**0.848 ± 0.004**	**154.4 ± 3.7**	**65 ± 2**	**77 +3/-2.5**
P3(B3)	**1.45**	**63.4**	**0.487 ± 0.007**	**0.848 ± 0.005**	**137.8 ± 5.1**	67 ± 3	**96 +3/-2.6**
P3(B4)	0.92	84.2	0.555 ± 0.005	0.883 ± 0.003	135.3 ± 5.8	75 ± 3	114 +2.5/2.3
P3(B5)	**0.42**	**90.7**	**0.690 ± 0.012**	**0.953 ± 0.007**	**200.9 ± 6.3**	**139 ± 5**	**143 +6.5/-6.2**
P3(core)		5.5	0.994 0.017	1.106 ±0.007	123.4 ± 13.3	125 ± 1	227 +16/-14

Rind thickness: 2.2 mm

Pisolith (band)	Distance from core (mm)	^{238}U* (ppm)	$^{230}Th/^{238}U$	$^{234}U/^{238}U$	$^{238}U/^{232}Th$	$^{230}Th/^{232}Th$	Apparent age (ky)
P5(B1)	**1.68**	**128.2**	**0.516 ± 0.012**	**0.869 ± 0.007**	**90.3 ± 3.0**	**47 ± 2**	**101 +4.5/-4.3**
P5(B2)	1.1	33.2	0.683 ± 0.008	0.931 ± 0.004	84.5 ± 2.5	58 ± 2	148 +5/-4.5
P5(B3)	**0.8**	**96.4**	**0.668 ± 0.009**	**0.931 ± 0.006**	**134.8 ± 4.2**	**90 ± 3**	**141 +5/-4.6**
P5(core)		12.3	0.806 ± 0.007	1.009 ± 0.003	337.3 ± 101.2	272 ± 82	173 +5.2/-5.1

Rind Thickness: 1.95 mm

Pisolith (band)	Distance from core (mm)	^{238}U* (ppm)	$^{230}Th/^{238}U$	$^{234}U/^{238}U$	$^{238}U/^{232}Th$	$^{230}Th/^{232}Th$	Apparent age (ky)
P5a(B1)	**1.73**	**136.2**	**0.412 ± 0.011**	**0.833 ± 0.003**	**81.4 ± 3.1**	**34 ± 2**	**76 ± 3**
P5a(B2)	**1.43**	**55.3**	**0.532 ± 0.007**	**0.881 ± 0.002**	**101.6 ± 5.1**	**54 ± 3**	**104 ± 2.5**
P5a(B3)	1.03	210.2	0.658 ± 0.004	0.904 ± 0.004	70.8 ± 1.4	47 ± 1	147 ±3
P5a(B4)	**0.75**	**27.6**	**0.635 ± 0.007**	**0.905 ± 0.003**	**115.1 ± 4.6**	**73 ± 3**	**136 ± 3.7**
P5a(B5)	**0.53**	**220.4**	**0.634 ± 0.004**	**0.902 ± 0.002**	**148.0 ± 7.4**	**94 ± 5**	**137 ± 3**
P5a(B6)	**0.23**	**244.7**	**0.702 ± 0.006**	**0.931 ± 0.002**	**132.7 ± 1.7**	**93 ± 1**	**157 ± 4**

Rind thickness 1.95 mm

Pisolith (band)	Distance from core (mm)	^{238}U* (ppm)	$^{230}Th/^{238}U$	$^{234}U/^{238}U$	$^{238}U/^{232}Th$	$^{230}Th/^{232}Th$	Apparent age (ky)
P6a(B1)	**1.57**	**126.0**	**0.477 ± 0.016**	**0.833 ± 0.010**	**47.3 ± 1.7**	**23 ± 1**	**96 +6/-5.5**
P6a(B2)	1.1	207.3	0.723 ± 0.011	0.919 ± 0.007	52.4 ± 1.3	38 ± 1	176 +9.5/-8
P6a(B3)	0.92	181.8	0.739 ± 0.007	0.965 ± 0.004	102. ± 2.3	75 ± 2	160 ± 5
P6a(B4)	**0.59**	**231.8**	**0.705 ± 0.006**	**0.949 ± 0.003**	**117.5 ± 3.8**	**83 ± 3**	**150 ± 4**
P6a(B5)	**0.25**	**231.8**	**0.783 ± 0.007**	**0.974 ± 0.004**	**129.7 ± 2.6**	**102 ± 2**	**180 ± 6**
P6(core)		21.6	0.993 ± 0.017	1.116 ± 0.009	142.3 ± 12.2	141 ± 12	219 +15/-13

Rind thickness: 1.75 mm

Pisolith (band)	Distance from core (mm)	^{238}U* (ppm)	$^{230}Th/^{238}U$	$^{234}U/^{238}U$	$^{238}U/^{232}Th$	$^{230}Th/^{232}Th$	Apparent age (ky)
P6(B1)	**1.42**	**110.4**	**0.456 ± 0.006**	**0.820 ± 0.002**	**65.9 ± 1.4**	**30 ± 1**	**92 ± 2.2**
P6(B2)	**0.92**	**194.2**	**0.579 ± 0.007**	**0.883 ± 0.001**	**112.8 ± 5.1**	**65 ± 3**	**120 ± 3.3**
P6(B3)	**0.62**	**173.2**	**0.806 ± 0.005**	**0.951 ± 0.002**	**137.2 ± 10.0**	**111 ± 8**	**213 +7.6/-6.8**
P6(B4)	0.27	211.2	0.819 ± 0.004	0.944 ± 0.002	190.1 ± 11.2	156 ± 9	232 +9/-8.2

Rind thickness 1.75 mm

Pisolith (band)	Distance from core (mm)	^{238}U* (ppm)	$^{230}Th/^{238}U$	$^{234}U/^{238}U$	$^{238}U/^{232}Th$	$^{230}Th/^{232}Th$	Apparent age (ky)
P13(B1)	**2.33**	**25.2**	**0.489 ± 0.009**	**0.830 ± 0.005**	**26.51 ± 0.81**	**13 ± 0.5**	**128 +6/-5.4**
P13(B3)	**1.82**	**54.3**	**0.563 ± 0.006**	**0.887 ± 0.003**	**52.78 ± 2.30**	**30 ± 1.3**	**113 ±5**
P13(B4)	1.63	54.2	0.646 ± 0.007	0.877 ± 0.005	27.82 ± 1.67	18 ± 1.1	154 ±5
P13(B5)	**1.31**	**48.7**	**0.702 ± 0.008**	**0.906 ± 0.008**	**60.73 ± 1.50**	**43 ± 1.2**	**170 ±7**
P13(B6)	1.08	41.3	0.850 ± 0.011	0.924 ± 0.005	31.66 ± 0.80	27 ± 0.8	314 +46/-30
P13(B7)	**0.65**	**38.5**	**0.773 ± 0.010**	**0.958 ± 0.008**	**32.22 ± 1.28**	**25 ± 1.0**	**183 +9.4/-8.3**
P13(B8)	0.35	46.1	0.836 ± 0.011	0.950 ± 0.004	53.55 ± 0.87	45 ± 0.9	242 +16/-14
P13(core)		5.9	0.896 ± 0.016	0.961 ± 0.008	27.09 ± 1.60	24 ± 1.5	314 +57/-35

Rind thickness 2.52 mm

Pisolith (band)	Distance from core (mm)	^{238}U* (ppm)	$^{230}Th/^{238}U$	$^{234}U/^{238}U$	$^{238}U/^{232}Th$	$^{230}Th/^{232}Th$	Apparent age (ky)
P14(B1)	**1.53**	**30.0**	**0.343 ± 0.008**	**0.878 ± 0.001**	**79.7 ± 5.8**	**27 ± 2**	**54.5 ± 2**
P14(B2)	1.2	52.2	0.603 ± 0.008	0.921 ± 0.002	72.8 ± 1.4	44 ± 1	118 ± 3.1
P14(B3)	**0.88**	**73.4**	**0.604 ± 0.005**	**0.932 ± 0.002**	**149.9 ± 5.6**	**91 ± 3**	**115 ± 3**
P14(B4)	**0.57**	**88.4**	**0.759 ± 0.005**	**1.001 ± 0.003**	**259.7 ± 8.4**	**197 ± 7**	**154 ± 3.5**
P14(B5)	**0.25**	**101.2**	**0.795 ± 0.009**	**1.008 ± 0.004**	**68.8 ± 4.4**	**55 ± 4**	**168 ± 6**
P14(core)		15.4	0.918 ± 0.008	1.024 ± 0.005	213.5 ± 29.6	196 ± 27	241 +12/-11

Rind thickness 1.8 mm